Nanofluidic Species Transport and Nanostructure Based Detection On-Chip

by

Angela De Leebeeck
B.Eng., University of Victoria, 2004
Diploma of Technology, British Columbia Institute of Technology, 2001

A Thesis Submitted in Partial Fulfillment of the Requirements for the Degree of

MASTER OF APPLIED SCIENCE

in the Department of Mechanical Engineering

Nanofluidic Species Transport and Nanostructure Based Detection On-Chip

by

Angela De Leebeeck
B.Eng., University of Victoria, 2004
Diploma of Technology, British Columbia Institute of Technology, 2001

Supervisory Committee:

Dr. David Sinton, (Department of Mechanical Engineering)
Supervisor

Dr. Peter Oshkai, (Department of Mechanical Engineering)
Departmental Member

Dr. Reuven Gordon, (Department of Electrical and Computer Engineering)
Outside Member

Supervisory Committee:

Dr. David Sinton, (Department of Mechanical Engineering)
Supervisor

Dr. Peter Oshkai, (Department of Mechanical Engineering)
Departmental Member

Dr. Reuven Gordon, (Department of Electrical and Computer Engineering)
Outside Member

ABSTRACT

Transport in nanostructures and on-chip detection using nanohole arrays are investigated using a combination of analytical, numerical and experimental techniques. The first half of the thesis describes a fundamental theoretical contribution to the study of nanofluidic species transport. The second half of the thesis describes an applied experimental application of nanostructure-based species detection in a microfluidic framework.

A continuum based analytical solution and numerical model are developed to quantify ionic dispersion of charged and neutral species in nanochannels and identify fundamental dispersion mechanisms unique to nanoscale flows. Ionic dispersion for circular cross-section nanochannels is quantified as a function of a valance parameter, the relative electrical double layer thickness, and the form of the velocity profile. Two unique mechanisms governing ionic dispersion in both pressure- and electrokinetically driven flows are identified. The results of the analytical solution are supported and extended by the results of the numerical model. Collectively, these results indicate that dispersion of ionic species in nanoscale channels is markedly charge dependent, and substantially deviates from that of neutral solutes in the same flow.

A microfluidic device with a set of embedded nanohole array surface plasmon resonance sensors is developed and successfully demonstrated experimentally as a chemical/biological sensor. The device takes advantage of the unique optical properties, the surface-based sensitivity, the transmission mode operation, relatively small footprint, and repeatability characteristic of nanohole arrays. Proof-of-concept measurements are performed on-chip to detect changes in liquid refractive index at the array surface, proportional to change in near wall concentration or indicative of a surface binding event. Employing a cross-stream array of nanohole arrays, the device is applied to detect microfluidic concentration gradients as well as to detect surface binding in the assembly process of a cysteamine monolayer-biotin-streptavidin system.

TABLE OF CONTENTS

Chapter 1 – INTRODUCTION

Chapter 2 – NANOFLUIDIC SPECIES TRANSPORT

Chapter 3 – NANOSTRUCTURE BASED DETECTION ON-CHIP

Chapter 4 – CONCLUSIONS AND FUTURE WORK

LIST OF FIGURES

Figure 1.1 Velocity profiles in circular cross section microchannels for a) pressure driven flow and b) electrokinetically driven flow.

Figure 1.2 Schematic of: (a) the non-uniform ion distribution near the solid surface which forms the electric double layer (EDL); and (b) the potential distribution in the EDL. The Debye length, λ_D, is the characteristic length of the EDL.

Figure 1.3 Dispersion of a neutral solute ($z = 0$) in a microchannel with a thin EDL (λ_D is less than 10 nm) when flow is a) pressure driven with a parabolic velocity profile in a channel of diameter 180 μm and b) electrokinetically driven with a pluglike velocity profile in a channel of diameter 120 μm [Sinton (2003), reproduced with permission].

Figure 1.4 Schematic illustration of the problem of dispersion of positive, neutral, and negative solutes in a nanochannel with finite EDL at late times. The electrokinetically driven velocity profile with a finite EDL is shown at the left, differing from pluglike flow characteristic of microchannels. Solute dispersion is a result of advection, diffusion, and in the case of charged solutes, electromigration.

Figure 1.5 A nanohole array. Surface plasmons help to enhance light transmission through subwavelength structures such as nanohole arrays making them suitable for use as on chip sensors. a) a square 20 x 20 μm nanohole array in a liquid filled microfluidic channel b) a portion of the nanohole array, the scale bar indicates 10 μm c) a single nanohole, approximately 150 nm in diameter.

Figure 2.1 Schematic illustrating Taylor dispersion. A discrete solute sample of length L undergoing Taylor dispersion in a circular cross-section channel of radius a is shown at time t = 0, at early times and at late times. Corresponding average concentration (average c) profiles are shown above. At early times dispersion is convection dominated and at later times, axial convection is balanced by radial diffusion resulting in pluglike flow and a Gaussian concentration profile. The concentration scale is shown at the left. Cmax is the maximum solute concentration.

Figure 2.2 a) Schematic illustrating the geometry of interest and the coupled effect of substantial EDL on cross-stream ionic concentration at late times. Axial cross-section concentration plots of discrete samples of counter-ion ($z = +2$), neutral ($z = 0$), and co-ion ($z = -2$) solutes are plotted for the cases of

b) Moderate EDL, λ_D/a = 0.05 and c) Thick EDL λ_D/a = 0.40. The same concentration scale and initial conditions were applied in both cases to facilitate direct comparison with respect to ion segregation. On the right, electroosmotic velocity profiles that would result from an axially applied electric field are plotted for each case. The concentration field data was calculated here with a commercial computational fluid dynamics modeling package (COMSOL MULTIPHYSICS, COMSOL Inc., Stockholm Sweden), for the case of $\zeta_o = \sigma a/\varepsilon =$ -90mV, details on the numerical model are provided in Section 2.3.

Figure 2.3 Schematic illustrating ionic dispersion of counter-ions, neutral species, and co-ions at late times in pressure driven flow when $\lambda_D/a = 0.1$. The concentration scale is shown at the right.

Figure 2.4 Plot of D_{eff}/D versus Pe^2 showing a linear relationship for the case of pressure driven flow with λ_D/a = 0.1. The slope of the straight line gives the value of the dispersion coefficient, *f*.

Figure 2.5 Analytical solution results for pressure driven flow at late times. Dispersion coefficient *f* resulting from pressure driven flow is plotted versus relative EDL thickness for counter-ions, co-ions and neutral solutes. Unaffected by the EDL, the neutral ($Z = z = 0$) case is co-linear with the Taylor limit ($f = 1/48 \cong 0.21$) [Taylor (1953)]. For ionic solutes, the effect of valence charge is generalized through the non-dimensional valence parameter, *Z*. The plotted cases of Z = 7.0 to -7.0 were selected to correspond to ions of valence charge, z = -2 to +2, with $\zeta_o = \sigma a/\varepsilon =$ -90 mV.

Figure 2.6 Analytical solution results for electrokinetically driven flow at late times. Dispersion coefficient *f* resulting from electrokinetically driven flow is plotted versus relative EDL thickness for counter-ions, co-ions and neutral solutes. Values of *f* for the neutral case ($z = 0$) agree with those calculated from a previous study for neutral solutes [Datta and Kotamarthi (1990)] (also plotted). The neutral species dispersion coefficient approaches the Taylor value ($f = 1/48 \cong 0.21$, plotted as a dashed line) [Taylor (1953)] as EDL thickness increases. For ionic solutes, the effect of valence charge is generalized through the non-dimensional valence parameter, *Z*, and the cases of Z = 7.0 to -7.0 correspond to ions of valence charge, z = -2 to +2, with $\zeta_o = \sigma a/\varepsilon =$ -90 mV as in Figure 2.5.

Figure 2.7 Numerical modeling and analytical solution results for pressure driven flow at late times. Dispersion coefficient *f* resulting from pressure driven flow is plotted versus relative EDL thickness for counter-ions, co-ions and neutral solutes comparing the computational model using the nonlinear

Poisson Boltzmann (NPB) equation with the analytical model using the linear Poisson Boltzmann (LPB) equation. The analytical results stop at $\lambda_D/a = 0.4$ (the limit of the linear Poisson Boltzmann equation) while the computational model results are extended to $\lambda_D/a = 0.6$. The computational results reinforce the trends seen in Figure 2.5 and show that the trend continues for λ_D/a above 0.4. For ionic solutes, the effect of valence charge is generalized through the non-dimensional valence parameter, Z, and the cases of $Z = 7.0$ to -7.0 correspond to ions of valence charge, $z = -2$ to +2, with $\zeta_o = \sigma a/\varepsilon = -90$ mV as in Figure 2.5.

Figure 2.8 Numerical modeling and analytical solution results for electrokinetically driven flow at late times. Dispersion coefficient f resulting from electrokinetically driven flow is plotted versus relative EDL thickness for counter-ions, co-ions and neutral solutes comparing the computational model using the nonlinear Poisson Boltzmann (NPB) equation with the analytical model using the linear Poisson Boltzmann (LPB) equation. The analytical results stop at $\lambda_D/a = 0.4$ (the limit of the linear Poisson Boltzmann equation) while the computational model results are extended to $\lambda_D/a = 0.6$. The computational results reinforce the trends seen in Figure 2.6 and show that the trend continues for λ_D/a above 0.4. For ionic solutes, the effect of valence charge is generalized through the non-dimensional valence parameter, Z, and the cases of $Z = 7.0$ to -7.0 correspond to ions of valence charge, $z = -2$ to +2, with $\zeta_o = \sigma a/\varepsilon = -90$ mV as in Figure 2.5.

Figure 3.1 Schematic and description of the soft-lithography microfabrication method.

Figure 3.2 Nanohole array sensor map with periodicities indicated in nanometers. The identical upper row arrays are for cross-stream concentration gradient measurements. Only portions of each array are shown.

Figure 3.3 Schematic of the microfluidic chip with embedded nanohole arrays. Two microfluidic configurations are shown with the sensing element pattern illustrated below with sample SEM images of the nanoholes. Each array is 20 μm x 20 μm. a) The microchannel configuration shown on the left enables measurements (with fixed periodicity) across a concentration gradient (referred to as configuration a in the text). b) The chip configuration shown on the right enables single solution (multisensor) tests (referred to as configuration b in the text).

Figure 3.4 Prototype chip. To ensure sealing, the reversible bond at the acrylic-PDMS and PDMS-gold interfaces was reinforced with clamping pressure.

Tube connections were made by friction fit into the pre-punched PDMS layer.

Figure 3.5 Experimental setup for transmission spectrum measurements through nanohole arrays. A broadband halogen light source was employed.

Figure 3.6 Electrical potential variation along a microchannel with electroosmotic flow where 1000 V is applied at the inlet and the outlet is grounded, and the corresponding gold patterning. The inset plot shows an expanded 2-D view of iso-potential lines near point B. The points labeled A, B and C correspond to velocity profiles on the right. Location A is the electroosmotic velocity profile 0.5 cm along the channel. Location B is the transition velocity profile 1.005 cm along the channel. Location C is the pressure-driven velocity profile 1.5 cm along the channel over gold.

Figure 3.7 Concentration and circulation in nanoholes. The concentration in and around the nanoholes is shown during the exchange of solutions. The inset shows circulation in the nanoholes, the scale indicates an arrow length of 200 nm/s. The color scale on the right indicates the non-dimensional concentration.

Figure 3.8 Variation in concentration over time at the base of a nanohole during a solution replacement. It takes 0.2 seconds to reach a non-dimensional concentration of 1 (to within 99.9%).

Figure 3.9 Transmission spectra for arrays of varying periodicity with water in the PDMS channel structure over the arrays. The array periodicities are indicated in nanometers in the legend.

Figure 3.10 Transmission spectra for arrays of varying periodicity in water with no PDMS channel structure over the arrays. A droplet of water was placed on the bare gold surface over the arrays. The array periodicities are indicated in nanometers in the legend.

Figure 3.11 Comparison of transmission spectra for pure water (refractive index, n = 1.332) and sugar solution (refractive index, n = 1.352) in channel over the arrays. a) Transmission spectra for arrays of periodicity 350nm and 450 nm. b) Transmission spectra for arrays of periodicity 550nm and 650 nm. c) Transmission spectra for arrays of periodicity 750nm and 850 nm.

Figure 3.12 Transmission spectra in the array with periodicity 450nm for pure water (refractive index, n = 1.332), sugar solutions with refractive index varying from 1.338 to 1.358, and again for water after the sugar solution has been flushed out. The red shift in resonance peak wavelengths can be seen. The refractive index is indicated in brackets in the legend.

LIST OF TABLES

NOMENCLATURE

a	channel radius
c	concentration of a solute
c / c_o	dimensionless concentration of a solute
$\langle c \rangle_{\max} / c_o$	maximum area averaged concentration
$\bar{c}$	cross sectional area averaged or area averaged or average concentration
c_∞	concentration of bulk electrolyte
$c_{\infty,i}$	concentration of ions of species *i* in the bulk solution
c_{CL}	solute centerline concentration
c_i	concentration of ions of species *i*
c_o	solute concentration at $t = 0$
d	channel diameter
e	the charge of an electron, 1.6022×10^{-19} C
f	dispersion coefficient
$\vec{g}$	acceleration of gravity, 9.81 m s^{-2}
$h = h(r, \frac{\partial c}{\partial x'}) = \int_0^r B^{-1}\left(\frac{1}{r'}\int_0^{r'} r''u'(r'')\frac{\partial c}{\partial x'}dr''\right)dr'$	a function
h_C	channel height
k	Boltzmann's constant, 1.3807×10^{-23} J K^{-1}
l	characteristic length of a flow channel
n	refractive index

$\vec{n}$	unit normal vector
n_o	number of moles of solute species
p	pressure
r	radial coordinate
$r^* = r/a$	dimensionless radial coordinate
s	separation distance between two charged surfaces
t	time
u	axial component of velocity
$u^* = u(r)/u_{ref}$	dimensionless velocity
u'	solute velocity with respect to the moving axis
u'^*	dimensionless velocity with respect to the moving axis
$\vec{u}$	velocity vector
u_{avg}	average net solute velocity
u_{CA}	concentration weighted area averaged velocity
$u_{eo} = -\varepsilon\zeta E/\mu$,	Helmholtz-Smoluchowski velocity
$u_{pd} = a^2/8\mu(-dp/dx)$,	average pressure driven flow velocity
u_{ref}	a reference velocity
$v_D = D/l$,	diffusion velocity
x	axial coordinate
x'	moving coordinate
Δx_c	mixing width at the channel center
Δx_w	mixing width at the channel wall

x'	moving axial coordinate
y	distance traveled along a channel
z	valence number of a solute
z_e	valence number of an electrolyte
z_i	valence number of ions of species i
$B = \exp\left(-ez(\psi - \psi_c)/(kT)\right)$, a function	
D	molecular diffusion coefficient
D_{eff}	effective diffusion coefficient
E	axially applied electric field
$\vec{E}$	electric field vector
F	Faraday's constant, 96485 C mol^{-1}
$\vec{F}$	body force vector
I_o	zeroth order modified Bessel function of the first kind
I_1	first order modified Bessel function of the first kind
$Kn = \lambda / a$	Knudsen Number
L	solute axial band length
L_o	solute band length at $t = 0$
$Pe = Ua / D$	Peclet Number
N_A	Avogadro's Number, $6.022\text{x}10^{23}$ mol^{-1}
$\text{Re} = lU / \upsilon$	Reynolds Number
T	temperature
U	bulk-averaged velocity

V_l	molar volume occupied by one mole of liquid at 298 K
$Z = (ez\zeta_o)/(kT) = (ez\sigma a)/(kT\varepsilon)$	valence parameter
δ	lattice spacing in a liquid
ε	electrical permittivity
ε_o	permittivity of a vaccum, $8.8542\text{x}10^{-12}$ C V^{-1} m^{-1}
ε_r	relative permittivity or dielectric constant of a liquid
ϕ	electric potential due to an applied electric field
λ	mean free path of a gas
$\lambda_D = \left(\dfrac{\varepsilon_r \varepsilon_o kTN_A}{2z_e^2 F^2 c_\infty}\right)^{1/2}$	Debye length, the characteristic length of an electric double layer
λ_D / a	relative electric double layer thickness
μ	viscosity
υ	kinematic viscosity
ν_{im}	ionic mobility of a solute
ρ	density
ρ_E	net charge density
σ	surface charge density
$\tau = a^2 / D$	diffusion time parameter
ψ	electrical potential due to the presence of the electric double layer
$\psi^* = \psi / \zeta_o$	dimensionless electrical potential due to the electric double layer
ψ_c	electric potential at the channel centerline
ζ	zeta potential at the shear plane of an electric double layer

$\zeta_o = \sigma a / \varepsilon$ electric potential parameter

$\langle ... \rangle = 2a^{-2} \int_0^a ... r dr$ cross-sectional area averaged or area averaged or average quantity

ACKNOWLEDGEMENTS

I would like to express my deepest gratitude to my supervisor, Dr. David Sinton, for his excellent guidance, support, patience, and providing me with an excellent atmosphere for doing research. His enthusiasm and motivation encouraged me to learn and to grow as an individual. I thank Dr. Sinton for giving me the opportunity to work with him; it has been an exceptional two years.

I would like to acknowledge and thank the collaborating researchers who worked with me on the nanohole arrays project: Dr. Brolo and Dr. Gordon, Kiran, Erin, and Victoria. It has been a pleasure to work within this multidisciplinary group. I also thank Marcos for his assistance in the chemistry lab.

I would like to thank the members of the Microfluidics Lab, past and present, for all of the interesting discussions, insights, feedback, Microfluidics dinners and Cheese Day celebrations that will make this experience so memorable. I would like to thank my friends as well for making the last two years enjoyable and for all the stress reducing activities outside of the lab. A special thanks to my best friend, Germaine. She has been like family while my parents live on the other side of the world.

This research was made possible through financial support provided by the Natural Science and Engineering Research Council of Canada (NSERC) and the University of Victoria.

Finally, it is to my family, Mom, Dad and Lisa, that I dedicate this work. The love, encouragement and support (both emotional and financial) from my family has been incredible. Thank you.

Chapter 1

INTRODUCTION

1.1 Aims and Motivations of the Thesis

The benefits associated with the miniaturization of fluid-based laboratory processes are primary driving forces in microfluidics research. Micro-sized chemical synthesis and analysis systems can offer many advantages over their macro-sized counterparts in terms of speed, cost, sample/reagent consumption, sensitivity, efficiency, safety and automation. Developments in microfluidic engineering towards these applications are documented in review papers spanning several years [Brody et al. (1996); Ho and Tai (1998); Bousse et al. (2000); Whitesides and Stroock (2001); Verpoorte and De Rooij (2003)], and more recently by Stone et al. (2004), Kamholz et al. (2004), Eijkel and van den Berg (2005), and book chapters [Sharp et al. (2002)], and recent books [Nguyen and Wereley (2002); Li (2004)]. Recently, unique transport and optical phenomena facilitated by nanochannels and nanostructures have shown promise [Eijkel and van den Berg (2006), Barnes et al. (2003)] for on chip analytical processing.

The microscopic length scale ranges from 1 μm to 1 mm, below 1 μm is the nanoscale and above 1 mm is macroscopic [Gad-el-Hak (2005)]. The typical range of dimensions for microfluidic devices fabricated in glass and polymers is between 30 and 300 μm [Sharp et al. (2002)]. Miniaturization results in increased surface to volume ratios, which leads to increased rates of heat and mass transfer, useful in compact heat exchangers [Sharp et al. (2002)]. Increased surface to volume ratios are also advantageous in applications with surface based reactions such as microstructured fuel cells [Dyer (2002), Bazylak et al. (2005)]. Benefits associated with the miniaturization of devices for biological, biomedical and chemical analysis have been a major driving force in microfluidics engineering [Reyes et al. (2002)]. So called lab-on-chip processing can result in analysis methods with increased sensitivity, process integration, control and speed, and decreased cost, reagent consumption, and contamination. In addition to direct scaling benefits, many lab-on-a-chip devices exploit functionality unique to microfluidics [Stone et al. (2004)]. Liquid flows in microchannels are typically laminar and characterized by very low Reynolds numbers indicating that viscous forces dominate inertial forces. A consequence of the laminar nature of the flow is that mixing is limited to diffusive effects only and mixing times are generally very slow [Squires and Quake (2005)]. An application that exploits this characteristic is the T-sensor where two parallel liquid streams flow side by side in the same channel with cross-stream diffusion enabling temporal analysis of chemical and biological processes [Squires and Quake (2005)]. An early application of the T-sensor was provided by Weigl and Yager (1999) who determined human serum albumin concentrations using the device. Other common applications that take advantage of this property include particle separations by size or electric charge [Squires and Quake (2005), Ghosal (2004)]. Applications of microscale processing, on some level, are common in the fields of biological and chemical analysis [Reyes et al. (2002)]. Recent advances in microfabrication and microfluidics have also provided a door to harnessing unique properties of nanostructures, particularly unique nanofluidic and subwavelength optical phenomena.

The nanoscale applies to devices with dimensions between 1 nm and 1 μm. Particularly in biology, this is the length scale on which many fundamental processes take place [Tegenfeldt et al. (2004), Eijkel and van den Berg (2005)]. Nanofluidic devices allow for single molecule studies [Eijkel and van den Berg (2005)] and single strand DNA analysis [Tegenfeldt et al. (2004)]. In contrast to many microfluidic applications where the electric double layer (EDL) at the solid-liquid surface is well approximated by an infinitely thin layer [Sharp et al. (2002)], nanofluidics involves finite, and sometimes overlapping, EDL effects. In a recent review, Eijkel and van den Berg (2006) discuss nanofluidics as applied to separation devices. Nanofluidics can be used to reduce band broadening (i.e. increase resolution) in separations [Gzil et al. (2003)], to tailor the characteristics of entropic traps to certain sizes of DNA [Han and Craighead (2000)], and extend the functionality of sieves [Huang et al. (2004), Eijkel and van den Berg (2006)].

In addition to facilitating unique nanofluidic transport phenomena, nanometer-scale structures exhibit unique optical phenomena. Such nanoscale structures are common in natural systems [Vukusic and Sambles (2003)]. Periodic arrays of nanoholes smaller than the wavelength of light in optically thick metallic films have shown enhanced transmission of light much higher than expected [Barnes et al. (2003), Gordon et al. (2004)]. The high transmission is due to the coupling of light with surface plasmons which are electronic excitations on the surface of a metal [Ebbesen et al. (1998)]. The optical properties of nanohole arrays on metal films make them suitable for enhanced Raman spectroscopy used in the detection of single molecules [Brolo et al. (2004b), Barnes et al. (2003)], magneto-optic data storage, solar cells [Barnes et al. (2003)], and for use as sensors in biology and chemistry [Barnes et al. (2003), Brolo et al. (2004a), Liu et al. (2004)]. The small size of nanohole arrays also makes them suitable for integration into microfluidic devices [Brolo et al. (2004a), Liu et al. (2004)], combining microfluidic flow control and sample preparation with unique nano-optic sensing capabilities.

In this thesis, transport in nanostructures and on-chip species detection using nanohole arrays are investigated using a combination of analytical, numerical and experimental techniques. Continuum based transport equations are employed to develop an analytical solution and a numerical model to quantify ionic dispersion in nanofluidic channels. A device integrating nanohole array surface plasmon resonance (SPR) sensors into a microfluidic structure is fabricated and demonstrated experimentally as a chemical sensor. In the broader context of the University of Victoria Microfluidics Lab group, this thesis represents a first foray into nanofluidic transport phenomena and early collaborative work through the BC Research in Nano Optics (BC-RINO) initiative.

The aims of this thesis work are to:

1. Develop a continuum based analytical solution for ionic dispersion of solutes in a nanofluidic channel with finite EDLs.
2. Develop a continuum based numerical model for ionic dispersion in a nanofluidic channel to compare with and extend the analytical solution.
3. Quantify ionic dispersion of charged and neutral solutes in a nanofluidic channel and identify fundamental dispersion mechanisms unique to nanoscale flows.
4. Demonstrate nanohole based SPR based sensors in a microfluidic chip format.

5. Develop an integrated microfluidic device with multiple embedded nanohole arrays of different periodicity for use as an on-chip surface plasmon sensor array.
6. Demonstrate the microfluidic device with embedded nanohole arrays as a chemical sensor experimentally by measuring bulk changes in concentration.
7. Apply the microfluidic device to measure cross-stream concentration gradients.
8. Apply the microfluidic device to monitor surface protein binding events.

1.2 Micro and Nanofluidic Transport Phenomena

This section provides a brief introduction to liquid flow and species transport in micro and nanoscale structures. Highlighted are the transport phenomena central to the nanofluidic ionic dispersion work of chapter 2 and the nanohole array based sensor chip of chapter 3. First a review of classical pressure driven flow is presented and then electrokinetically driven flow commonly seen in microfluidic devices is discussed. Species transport is also covered here and the applicability of the continuum assumption for nanostructures is discussed.

1.2.1 Classical Internal Fluid Flow

Liquid flow in microscale channels is generally incompressible, laminar and fully-developed (within one hydraulic diameter of the entrance). The incompressible assumption is suitable for aqueous solutions where the density does not change significantly with pressure, for example, the density of water at standard temperature and pressure changes only by 1% with an increase in pressure by a factor of 220 [White (1999)]. In fully developed flow, the velocity profile and wall shear are constant in the axial direction. Channel and pipe flows are described by the steady, incompressible continuity and Navier Stokes equations which are written as follows [Bird et al. (1960)],

$$(\bar{\nabla} \cdot \bar{u}) = 0 \qquad (1.1)$$

$$\rho(\bar{u} \cdot \bar{\nabla})\bar{u} = -\bar{\nabla}p + \mu\nabla^2\bar{u} + \rho\bar{g} \qquad (1.2)$$

where $\bar{u}$ is the velocity vector, ρ is the density, p is the pressure, μ is the viscosity and $\bar{g}$ is the acceleration of gravity.

Microscale flows are considered very viscous since viscous forces are considerably larger than the inertial forces. The ratio of inertial forces to viscous forces is defined by the Reynolds number, Re, as follows,

$$\mathrm{Re} = \frac{lU}{\upsilon} \qquad (1.3)$$

where l is the cross-sectional characteristic length of the flow channel, for example, the channel diameter, U is the average velocity, and υ is the kinematic viscosity. Typical values for Reynolds Number range from 10^{-6} to 10 [Squires and Quake (2005)] in microfluidic systems.

In a straight pipe of circular cross section, the Navier-Stokes equation takes on the following simplified form for pressure driven flow in a channel of circular cross section [Schlichting (1968)],

$$\frac{dp}{dx} = \mu\left(\frac{d^2u}{dr^2} + \frac{1}{r}\frac{du}{dr}\right) \qquad (1.4)$$

where x is the axial coordinate, r is the radial coordinate and du/dr is the shear rate which is highest at the wall. Equation 1.4 assumes a Newtonian fluid where viscosity is constant and shear forces are linearly proportional to the shear rate. For internal pipe flows with impermeable walls, pressure varies only in the axial direction as indicated in equation 1.4. Applying the no-slip boundary condition at the pipe wall ($\bar{u} = 0$), Equation 1.4 has the following analytical solution in cylindrical coordinates,

$$u(r) = -\frac{1}{4\mu}\frac{dp}{dx}(a^2 - r^2) \qquad (1.5)$$

where a is the radius of the pipe. This parabolic velocity profile is shown schematically in Figure 1.1 (figures are located at the end of each sub-section). As channel sizes decrease, the pressure required to induce flow becomes large and, in some cases, impractical [Tegenfeldt et al. (2004), Sharp et al. (2002)]. An alternative to pressure driven flow in small channels is electrokinetically driven flow.

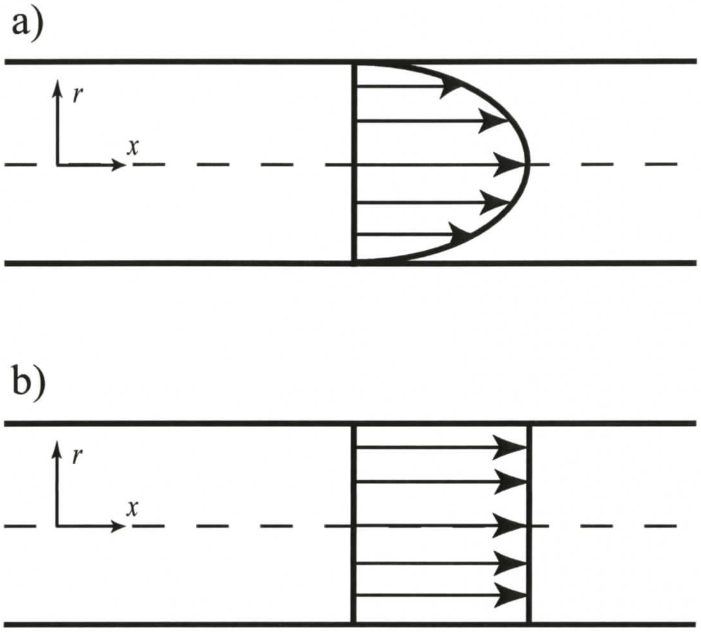

Figure 1.1 Velocity profiles in circular cross section microchannels for a) pressure driven flow and b) electrokinetically driven flow.

1.2.2 Electrokinetically Driven Flow

Solid surfaces acquire a surface electric charge when in contact with a liquid electrolyte [Probstein (1994)]. In response to this surface charge generation, ions in the electrolyte of opposite charge, termed counter-ions, are attracted to the electric charge while ions of like charge, termed co-ions, are repelled. This charge separation near the interface is termed the EDL. The bulk fluid away from the wall has a net neutral charge [Sharp et al. (2002)]. The EDL is composed of two regions: the compact or inner layer and the diffuse layer. The ion distribution and electric potential profile in the EDL are shown schematically in Figure 1.2. The compact layer is a layer of immobile ions very near the channel wall. Charge and electric potential distributions in the compact layer are determined by molecule size as well as specific interactions between ions and the wall [Hunter (1981)]. The diffuse layer is a layer of mobile ions further from the wall. The electric potential distribution in the diffuse layer is described by the Poisson-Boltzmann equation [Hunter (1981)]. The electric potential at the shear plane is called the zeta potential and its value can be determined from electroosmotic response or streaming potential measurements [Sharp et al. (2002)]. The shear plane (shown in figure 1.2b) is generally applied as the boundary in fluid flow analyses.

The concentration profile in the EDL is described by the Boltzmann distribution [Sharp et al. (2002)]. For ions of species *i*, the concentration profile is given by the following equation, assuming a liquid with constant properties,

$$c_i = c_{\infty,i} \exp\left(-\frac{z_i e \psi}{kT}\right) \qquad (1.6)$$

where c_i is the concentration of ions of species *i*, $c_{\infty,i}$ is the concentration of species *i* in the bulk solution, z_i is the valence of species *i*, *e* is the charge of an electron ($1.6022\text{x}10^{-19}$ C), ψ is the electric potential due to the presence of the EDL, *k* is Boltzmann's constant ($1.3807\text{x}10^{-23}$ J K^{-1}), and *T* is temperature. The net charge density in the EDL is given by [Probstein (1994)],

$$\rho_E = F\sum z_i c_i \qquad (1.7)$$

where *F* is Faraday's constant (96485 C mol^{-1}). The net charge density is related to the electric potential in the EDL by the Poisson equation [Probstein (1994)],

$$\nabla^2\psi = -\rho_E / \varepsilon_r\varepsilon_o \qquad (1.8)$$

where ε_r is the relative permittivity or dielectric constant of the liquid medium, and ε_o is the permittivity of a vacuum ($8.8542\text{x}10^{-12}$ $\text{CV}^{-1}\text{m}^{-1}$). Combining equations 1.6, 1.7 and 1.8 gives the Poisson-Boltzmann equation which for the case of a simple 1:1 symmetric electrolyte such as KCl is as follows [Probstein (1994)],

$$\frac{1}{r}\frac{d}{dr}\left(r\frac{d\psi}{dr}\right) = \frac{2Fz_e c_\infty}{\varepsilon_r\varepsilon_o}\sinh(\frac{z_e e\psi}{kT}) \qquad (1.9)$$

where z_e is the valence number of the electrolyte, and c_∞ is the bulk electrolyte concentration, (c_∞ is the same for both species in a 1:1 electrolyte). The Debye-Huckel limit is an approximation of equation 1.9 where the potential energy of ions in the EDL is small compared with their thermal energy [Probstein (1994)] i.e.

$$\sinh(\frac{z_e e\psi}{kT}) \approx \frac{z_e e\psi}{kT} \qquad (1.10)$$

This simplification holds well for values of electric potential up to 50 mV [Rice and Whitehead (1966)], where at room temperature (298 K) the term on the left of equation 1.10 has a value of 3.4 and the term on the right has a value of 2.0. For example, in a 1 mM monovalent electrolyte, the error in electric potential between the linear approximation and the nonlinear Poisson-Boltzmann equation is approximately 10% at the upper limit of 50 mV [Attard et al. (2000)]. Using the approximation in equation 1.10, equation 1.9 becomes a linear differential equation,

$$\frac{1}{r}\frac{d}{dr}\left(r\frac{d\psi}{dr}\right)=\frac{\psi}{{\lambda_D}^2} \qquad (1.11)$$

where the Debye length $\lambda_D=\left(\frac{\varepsilon_r\varepsilon_o kTN_A}{2z_e^2F^2c_\infty}\right)^{1/2}$ represents the characteristic thickness of the EDL, and N_A is Avogadro's number ($6.022\text{x}10^{23}$ mol^{-1}). Equation 1.11 is the linearized form of the Poisson-Boltzmann equation (equation 1.9). For a typical aqueous electrolyte with a concentration of 10 mM, it is on the order of a few nanometers [Sharp et al. (2002)].

Electroosmotic flow is commonly employed in microfluidic devices; it is flow induced by an axially applied electric field, E, which acts on the net charge density in the diffuse layer. For this type of flow, the electrostatic Lorentz force enters the Navier Stokes equation as a body force, active within the EDL where the net charge density is significant [Santiago (2001)]. The Navier Stokes equation with this electrostatic body force is then [Sharp et al. (2002)],

$$\vec{\nabla}p=\mu\nabla^2\vec{u}+\rho_E\vec{E} \qquad (1.12)$$

If the applied electric field in a channel is in the axial direction, the electric potential at the wall is uniform, and the pressure gradients are zero, the velocity profile for electrokinetically driven flow in a channel is [Sharp et al. (2002)],

$$u(r) = \frac{-\varepsilon_r \varepsilon_o E\zeta}{\mu}\left(1 - \frac{\psi}{\zeta}\right) \qquad (1.13)$$

where ζ is the zeta potential which is the electric potential at the shear plane of the EDL as shown in Figure 1.2b. For microchannels with EDLs ($\lambda_D \sim 10$ nm) that are thin relative to cross sectional (D ~ 10 μm), the velocity gradients within the EDL may be neglected and the bulk liquid velocity profile simplifies to the one-dimensional case [Sharp et al. (2002)],

$$u(r) = u = \frac{\varepsilon_r \varepsilon_o \zeta E}{\mu} \qquad (1.14)$$

Equation 1.14 is the Helmholtz-Smoluchowski equation for electroosmotic flow and holds for distances away from the channel wall that are greater than four times the Debye length (λ_D) [Santiago (2001)]. A schematic velocity profile comparing with that of pressure driven flow is shown in 1.1b.

Electrokinetically driven flow is easily controlled via fluid reservoir potential and enables fluid pumping with no moving parts. In channels greater than 10 μm, electroosmotic flow results in a pluglike velocity profile as shown in Figure 1.1b [Sharp et al. (2002)]. In this idealized case there are no cross-stream velocity gradients or 'shear'. The lack of shear provides an inherent advantage for transporting and separating discrete samples of reagents and analytes [Ghosal (2004)].

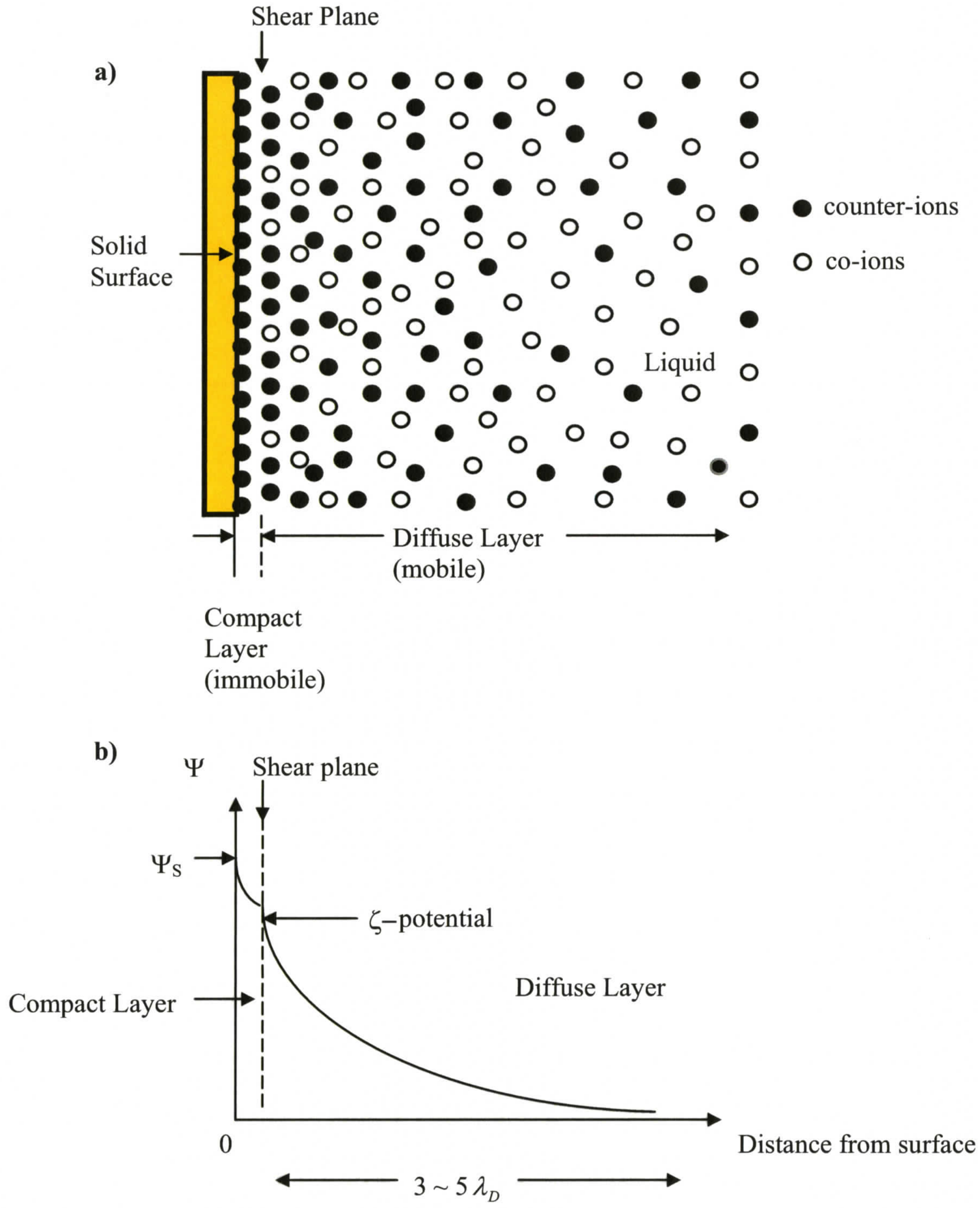

Figure 1.2 Schematic of: (a) the non-uniform ion distribution near the solid surface which forms the electric double layer (EDL); and (b) the potential distribution in the EDL. The Debye length, λ_D, is the characteristic length of the EDL.

1.2.3 Nanoscale Mass Transport

Unlike microchannels, EDLs in nanochannels are of significant thickness relative to the cross-channel dimension and thus the velocity profile for electrokinetically driven flow in nanochannels is not pluglike. Velocity gradients, or shear, in the EDL significantly influence species transport [Ghosal (2004)]. The species transport equation for a nonreacting solute is as follows [Bird et al. (1960)],

$$\frac{\partial c}{\partial t} + \vec{u} \cdot \bar{\nabla} c = D \nabla^2 c + \nu_{im} z F \bar{\nabla} \cdot (c(-\bar{E} + \bar{\nabla} \psi)) \qquad (1.15)$$

where c is the concentration of the solute species, t is time, ν_{im} is the ionic mobility, z is the valence charge of the solute species, and D is the molecular diffusion coefficient of the solute species. Equation 1.15 is applied to study ionic dispersion in nanochannels with finite EDL in chapter 2. The second term on the left side of equation 1.15 quantifies advection, the first term on the right quantifies ordinary diffusion, and the second term on the right quantifies electromigration of a charged species.

For a neutral species, where $z = 0$, equation 1.15 simplifies to:

$$\frac{\partial c}{\partial t} + \vec{u} \cdot \bar{\nabla} c = D \nabla^2 c \qquad (1.16)$$

Equation 1.16 is applied in Chapter 3 to model unsteady species transport within nano-sized holes during the replacement of one fluid with another over the nanohole arrays. This primarily diffusive transport limits the rate at which these sensors may sample an adjacent microfluidic stream.

1.2.4 Continuum Assumption

With the continuum approximation, all properties such as density, viscosity, and velocity are assumed to be well-defined and continuous everywhere. The analytical solutions and numerical models developed in this thesis are based on the continuum assumption which is consistent with previous nanoscale fluid dynamics modeling and experimental results [Pennathur and Santiago (2005a) and (2005b), Garcia et al. (2005)]. However, it is prudent to consider at what length scale the continuum approximation breaks down. The Knudson number gives an indication of the applicability of continuum models [Sharp et al. (2002)]. The Knudson number is defined as,

$$Kn = \lambda / a \qquad (1.17)$$

where for a gas, λ is the mean free path in a gas (the average distance a particle travels between collisions). For a liquid, lattice spacing δ is a similar measure to mean free path in a gas [Sharp et al. (2002)]. The lattice spacing is approximated as,

$$\delta \approx (V_t / N_A)^{1/3} \qquad (1.18)$$

where V_t is the molar volume occupied by one mole of liquid at 298 K. For water, δ is around 0.3 nm [Sharp et al. (2002)].

If the Knudson number is greater than 10^{-3} individual molecular interactions become significant and the continuum assumption is no longer applicable. For flow in the near-continuum range there are a variety of hybrid models to account for molecular interaction effects [Struchtrup (2005)]. For instance, modified slip boundary conditions can be used for continuum models for Knudson number between 10^{-1} and 10^{-3} [Gad-el-Hak (2005)]. As Kn increases beyond 10^{-1} continuum assumptions and classical fluid flow theory are no longer applicable [Sharp et al. (2002)]. For a liquid, related effects such as slip at the wall are predicted only if channels are less than 3 nm in cross section [Sharp et al. (2002)]. In general, continuum mechanics can safely be used to model liquid flows in channels with cross section dimensions over 10 nm. Gad-el-Hak (2005) notes that a microscopic volume containing more than $1\text{x}10^6$ molecules may be considered a continuum. A 1 μm cube contains $34\text{x}10^9$ water molecules, therefore the continuum approximation would apply to a volume as small as 30 nm^3 which contains $1\text{x}10^6$ water molecules. This volume represents a channel approximately 3 nm in diameter by 5 nm long. Qiao and Aluru (2003) compared ion distributions and velocity profiles of electrolytes in nanochannels calculated via molecular dynamics and continuum theory. Their results indicate that continuum theory can be used to predict bulk fluid flow in channels with widths down to 2.2 nm provided viscosity variations are accounted for, and that the continuum approximation breaks down completely for channel widths narrower than about 1 nm [Qiao and Aluru (2003)]. Deviations from predictions made by classical continuum theory have been observed for liquids confined to 10 molecular diameters [Eijkel and van den Berg (2005)], which corresponds to about 5 nm.

In this thesis, nanochannels with a diameter on the order of 50 nm and nanohole arrays with a diameter on the order of 100 nm are studied. These dimensions are at least an order of magnitude larger than established limits of the continuum approximation for liquid flows [Qiao and Aluru (2003), Gad-el-Hak (2005), Sharp et al. (2002)] and therefore, the use of the continuum assumption in this work is considered appropriate.

1.3 Solute Dispersion in Channels

Dispersion is the process whereby a locally concentrated solute is distributed in a solution, toward the equilibrium condition of uniform concentration [Probstein (1994)]. Axial dispersion, in combination with translation at a bulk-averaged velocity, characterizes the transport of solute bands in channels and is fundamental to the majority of separation techniques involving electrophoresis and chromatography. Distinct and detectable solute bands are the hallmark of a quality separation. Dispersion effectively broadens solute bands thus mitigating detection and ultimately limiting the separation efficiency and resolution attainable with these analytical techniques.

Solute dispersion in a laminar pressure driven flow through a circular cross-section channel was first characterized by Sir Geoffrey Taylor [Taylor (1953)]. Citations numbering in the thousands indicate the impact of this seminal work. Taylor (1953) divided the dispersion process into two regimes: an early period and a late period. At early times, dispersion is convection dominated leading to a rapid increase in axial length of the solute band and significant cross-stream diffusion. Fluorescent dye transport in this regime is shown in the image sequence in Figure 1.3a, obtained via molecular tagging velocimetry [Sinton (2003)]. At later times, a quasi-equilibrium is reached where the axial convection is balanced by radial diffusion. The resulting cross-stream-averaged axial concentration profile is Gaussian, resembling that of diffusive transport alone with an increased diffusion coefficient, and travels in a plug-like fashion at the average flow velocity (equivalent to one-half the centerline fluid velocity). Taylor (1953) found that the ratio of the effective diffusion coefficient, D_{eff}, to the molecular diffusion coefficient, D, was proportional to the square of the Peclet number, Pe, where $Pe = Ua/D$ is a relative measure of convective to diffusive species transport in a channel of radius, $a = d/2$, with bulk-averaged velocity, U. More generally, so-called Taylor-Aris dispersion is the sum of axial molecular dispersion and Taylor dispersion $D_{eff}/D = 1 + Pe^2/48$ [Probstein (1994), Aris (1956)].

Instead of pressure driven flow, capillary electrophoresis based separation techniques exploit electrokinetically driven (electroosmotic) flow and differential electrophoretic velocities. Electroosmotic flow is bulk fluid motion induced by the interaction of the EDL at the solution-channel interface and an axially applied electric field [Probstein (1994)]. In the limiting case of ideal electroosmotic flow in a straight channel, the EDL is negligibly thin relative to the cross-stream channel dimension and a plug-like velocity profile results as shown schematically in Figure 1.1b. In the absence of cross-stream velocity gradients, Taylor-style dispersion is absent and dispersion is limited to axial molecular dispersion alone ($D_{eff}/D = 1$) – a significant benefit in the context of separation science. Dispersion of a fluorescent dye sample in an electrokinetically driven flow is shown in figure 1.3b [Sinton (2003)] compared to the pressure driven dispersion case, the electrokinetically driven flow in the microchannel is effectively limited to axial dispersion. With EDL thicknesses on the order of 10nm, many microchannel/capillary-based systems approximate this ideal case. When finite EDL thicknesses are considered, the near-wall velocity gradients result in additional dispersion. Dispersion of a neutral species due to such velocity gradients has been studied for electroosmotic flow [Griffiths and Nilson (1999), Griffiths and Nilson (2000b), Zholkovskij et al. (2003)] and combined pressure driven and electroosmotic flow [Datta and Kotamarthi (1990), Dutta and Beskok (2001), Zholkovskij and Masliyah (2004)] in microchannels, and thoroughly reviewed by

Ghosal (2004). These studies focused on neutral solute transport, and the effect of valence charge on solute dispersion was not considered. Recent experimental studies [Pennathur and Santiago (2005a) and (2005b), Garcia et al. (2005)] demonstrated promising electrophoretic separation mechanisms, unique to flow in nanostructures, however both studies involved relatively low Peclet numbers ($Pe < 0.7$), and thus axial molecular diffusion dominated dispersion and ionic specific dispersion effects were not observed.

In Chapter 2, a continuum-based analytical solution is derived to quantify ionic dispersion of both charged and uncharged species in circular cross-section nanochannels with finite EDL for both cases of pressure- and electrokinetically driven flow at larger Peclet Numbers. Figure 1.4 shows ionic dispersion for a positive, neutral and negative solute showing the difference between these three cases. A numerical model is also developed for comparison with the analytical solution.

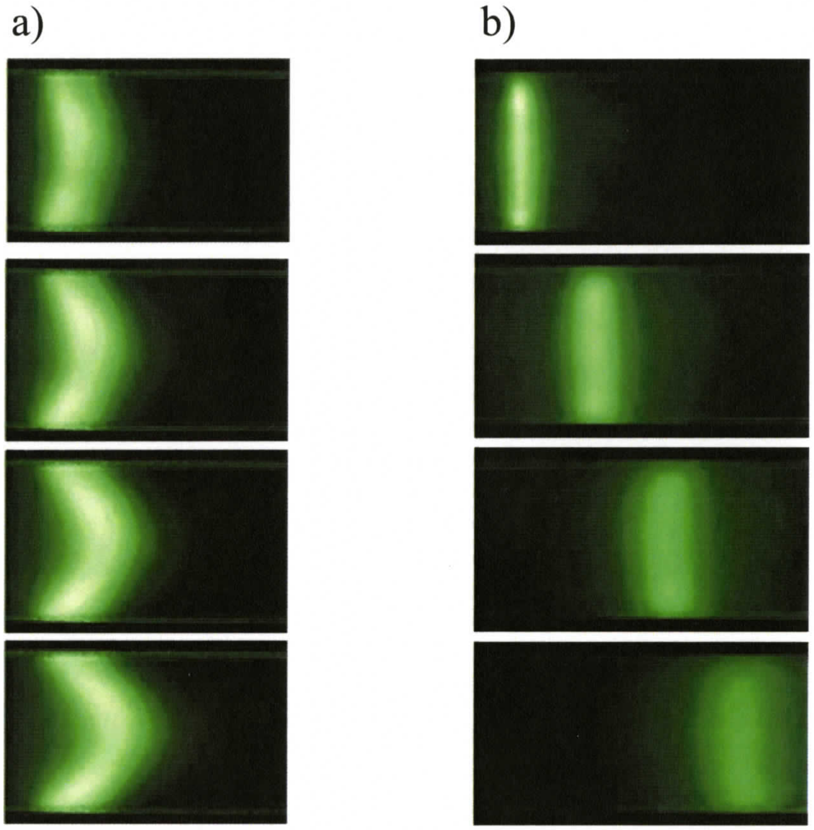

Figure 1.3 Dispersion of a neutral solute ($z = 0$) in a microchannel with a thin EDL (λ_D is less than 10 nm) when flow is a) pressure driven with a parabolic velocity profile in a channel of diameter 180 μm and b) electrokinetically driven with a pluglike velocity profile in a channel of diameter 120 μm [Sinton (2003), reproduced with permission].

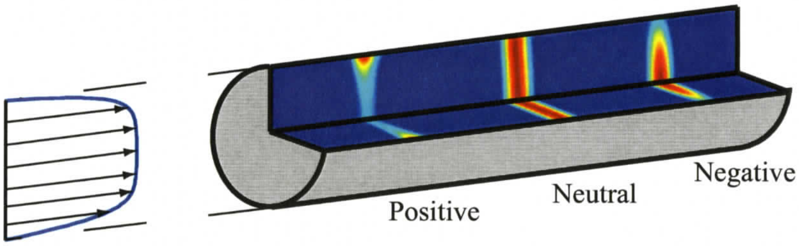

Figure 1.4 Schematic illustration of the problem of dispersion of positive, neutral, and negative solutes in a nanochannel with finite EDL at late times. The electrokinetically driven velocity profile with a finite EDL is shown at the left, differing from pluglike flow characteristic of microchannels. Solute dispersion is a result of advection, diffusion, and in the case of charged solutes, electromigration.

1.4 Microfluidic Device with Nanohole Array SPR Sensors

Surface plasmons are surface bound electromagnetic waves that can be excited in metallic nanostructures [Barnes et al. (2003)]. The ability to pattern nanoscale metal structures presents an opportunity to tailor surface plasmon response to specific applications, for example, chemical detection on the surface of metallic arrays of subwavelength holes. Such surfaces can support surface plasmons resulting in an enhanced transmission that is a strong function of the relative permittivities of the metal and the surrounding medium [Barnes et al. (2003)]. Nanohole array based SPR sensors are well suited to device level miniaturization/integration due to both the relatively small footprint of the nanohole arrays and the collinear optical arrangement afforded by transmission mode operation. A nanohole array is shown in Figure 1.5; the size of the array is about 20 x 20 μm. SPR in nanohole arrays has been applied previously (off-chip) to detect surface binding events of organic and biological molecules [Brolo et al. (2004 Langmuir)], and achieve enhanced fluorescence [Brolo et al. (2005)].

Combining microfluidic processing and control with nanoscale photonic structures, the nanohole array SPR sensors are integrated into a microfluidic device and their application for detecting concentration gradients and protein binding events is demonstrated in Chapter 3. This multidisciplinary work is done in collaboration with researchers in the electrical engineering department and the chemistry department at the University of Victoria formally through the British Columbia Research in Nano Optics initiative. The focus of this thesis work was to integrate the nanohole arrays into a microfluidic device and demonstrate proof-of-concept operation of the on-chip SPR sensor array. The microfluidic device was made by standard photolithographic techniques in the Microfluidics Lab which are discussed in detail in Chapter 3. Kiran Kumar from the electrical engineering group fabricated the nanohole arrays in a thin gold layer on a glass substrate using focused ion beam milling. Experimental measurements of concentration gradients in a channel with two parallel streams and protein binding were conducted in the Microfluidics lab using a spectrometer provided by the chemistry group. The protein binding tests were done with the assistance of members of both the collaborating electrical and chemistry groups.

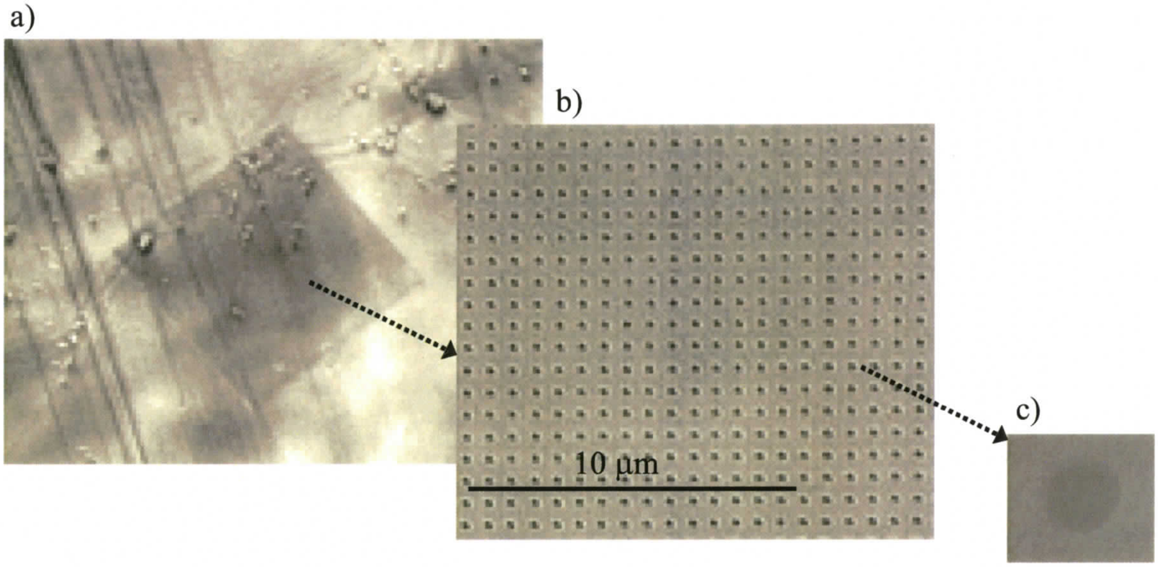

Figure 1.5 A nanohole array. Surface plasmons help to enhance light transmission through subwavelength structures such as nanohole arrays making them suitable for use as on chip sensors. a) a square 20 x 20 µm nanohole array in a liquid filled microfluidic channel b) a portion of the nanohole array, the scale bar indicates 10 µm c) a single nanohole, approximately 150 nm in diameter.

1.5 Overview of This Thesis

The contributions and structure of this thesis are summarized in the following paragraphs. The work in this thesis has also resulted in several conference proceedings [De Leebeeck et al. (2004), De Leebeeck and Sinton (2005), De Leebeeck et al. (2006a)], a submitted journal article [De Leebeeck and Sinton (2006)], and another article to be submitted in July/August 2006 [De Leebeeck et al. (2006b)].

In Chapter 1, the aims and motivation of the thesis work were presented followed by an overview of the pertinent microfluidic transport. A short introduction to ionic dispersion and nanochannels was given followed by an introduction to the concept of a nanohole array SPR sensor and its application in a microfluidic device.

In Chapter 2, a continuum based analytical solution and numerical model are developed for the study and quantification of ionic dispersion of a solute in circular nanochannels with finite EDLs. Dispersion of positively charged, neutral and negatively charged solutes at larger Peclet numbers are considered.

In Chapter 3, a microfluidic device with embedded nanohole arrays is developed and demonstrated as a SPR sensor for on-chip chemical detection. The device is applied experimentally to the detection of concentration gradients and protein binding as proof-of-concept.

In Chapter 4, an overview of the key contributions and conclusions of the thesis is given, and future work stemming from these findings are suggested.

Chapter 2

NANOFLUIDIC SPECIES TRANSPORT

In this chapter, a continuum-based analytical solution is derived to quantify dispersion of charged and neutral species in circular cross-section nanochannels for both cases of pressure- and electrokinetically driven flow. A numerical model is then developed for comparison to and extension of the analytical solution. The influence of relatively thick electric double layers in nanoscale liquid flows on ionic dispersion through the coupled effects of both cross-stream electromigration and advection in the presence of cross-stream velocity gradients are investigated.

2.1 Background

The study and application of fluid flow in and around nanostructures, or nanofluidics, presents unique opportunities for biological and chemical analysis [Eijkel and van den Berg (2005)]. In contrast to many microfluidic applications where the electrical double layer (EDL) at the solid-liquid surface can be approximated as an infinitely thin layer, nanofluidics involves finite, and sometimes overlapping, EDL effects. Ionic transport is particularly affected and much recent work has focused on ion enrichment/depletion [Pu et al. (2004), Plecis et al. (2005)], and applications to nanofluidic transistors [Karnik et al. (2005)] and energy conversion [Daiguji et al. (2004b)]. As noted in a recent review [Eijkel and van den Berg (2005)], much relevant work in this area predates the term nanofluidics and has roots in classical physical chemistry. Nanofluidic analytical separation mechanisms, for instance, are native to established membrane science. However, by combining the ability to precisely fabricate nanostructures in conjunction with lab-on-chip microfluidic integration, several novel separation technologies have emerged such as macromolecular separation in ordered post arrays [Huang et al. (2002)], and entropic traps [Han and Craighead (2000)]. More recently, nanoscale electrophoretic separation methods have been developed [Pennathur and Santiago (2005a), Pennathur and Santiago (2005b), Garcia et al. (2005)]. The extension of electrophoretic separation methods from microchannels to nanochannels has potential for increased field strengths and associated increased speed of analysis and sensitivity. Perhaps more importantly, charge-specific interactions of ions with the substantial EDL in nanoscale channels, or 'nanoconfinement' [Garcia et al. (2005)], leads to solute velocities that differ significantly from that in otherwise similar microscale channels [Pennathur and Santiago (2005a), Pennathur and Santiago (2005b), Garcia et al. (2005)]. This distinction between nano- and microfluidic regimes opens an opportunity for integrated multi-scale electrophoretic analysis capable, for instance, of determining both ion valence and mobility independently [Pennathur and Santiago (2005a), Pennathur and Santiago (2005b)]. In contrast to microscale electrophoresis, however, nanoconfinement can also lead to charge-specific dispersion of analyte bands, as will be described in this chapter.

2.1.1 Dispersion of Solutes

Dispersion is the process whereby a locally concentrated solute is distributed in a solution, toward the equilibrium condition of uniform concentration [Probstein (1994)]. Axial dispersion, in combination with translation at a bulk-averaged velocity, characterizes the transport of solute bands in channels and is fundamental to the majority of separation techniques involving electrophoresis and chromatography. Distinct and detectable solute bands are the hallmark of a quality separation. Dispersion effectively broadens solute bands thus mitigating detection and ultimately limiting the separation efficiency and resolution attainable with these analytical techniques. Sir Geoffrey Taylor [Taylor (1953) developed the seminal work on dispersion theory for a non-reacting solute in laminar pressure driven flow in a circular cross-section channel. Taylor (1953) divided the dispersion process into two regimes: an early period and a late period, as can be seen schematically in Figure 2.1. At early times, dispersion is convection dominated leading to a rapid increase in axial length of the solute band and significant cross-stream diffusion. At later times, a quasi-equilibrium is reached where the axial convection is balanced by radial diffusion. The resulting cross-stream-averaged axial concentration profile is Gaussian, resembling that of diffusive transport alone with an increased diffusion coefficient, and travels in a plug-like fashion at the average flow velocity (equivalent to one-half the centerline fluid velocity). Taylor (1953) found that the ratio of the effective diffusion coefficient, D_{eff}, to the molecular diffusion coefficient, D, was proportional to the square of the Peclet number, Pe by a dispersion coefficient, f. More generally, so-called Taylor-Aris dispersion is the sum of axial molecular dispersion and Taylor dispersion $D_{eff}/D = 1 + fPe^2$, where f has a value of 1/48 for pressure driven flow [Probstein (1994), Aris (1956)].

Instead of pressure driven flow, capillary electrophoresis based separation techniques exploit electrokinetically driven (electroosmotic) flow and differential electrophoretic velocities. Electroosmotic flow is bulk fluid motion induced by the interaction of the EDL at the solution-channel interface and an axially applied electric field [Probstein (1994)]. In the limiting case of ideal electroosmotic flow in a straight channel, the EDL is negligibly thin relative to the cross-stream channel dimension and a plug-like velocity profile results as introduced in Chapter 1. Pluglike electroosmotic flow was compared to the parabolic nature of pressure driven flow in Figure 1.1. In the absence of cross-stream velocity gradients, Taylor-style dispersion is absent and dispersion is limited to axial molecular dispersion alone ($D_{eff}/D=1$) – a significant benefit in the context of separation science. With EDL thicknesses on the order of 10 nm, many microchannel/capillary-based systems approximate this ideal case. Channel turns can, however, induce dispersion in such systems as has been studied extensively [Griffiths and Nilson (2000a), Dutta and Leighton (2002), Molho et al. (2001)]. Also, in practice, pressure driven flow components commonly arise due to non-uniformities in fluid and surface properties [Attencia and Beebe (2005)], and externalities such as capillarity effects in fluid reservoirs [Crabtree et al. (2001)]. Other sources of dispersion result from analyte-wall adsorption/desorption dynamics [Ghosal (2004)].

When finite EDL thicknesses are considered, the near-wall velocity gradients result in additional dispersion. Dispersion of a neutral species due to these velocity gradients has been studied for electroosmotic flow [Griffiths and Nilson (1999), Griffiths and Nilson (2000b), Zholkovskij et al. (2003)] and combined pressure driven and electroosmotic flow in microchannels [Datta and Kotamarthi (1990), Dutta and Beskok (2001), Zholkovskij and Masliyah (2004)], and thoroughly reviewed by Ghosal (2004). These studies focused on neutral solute transport, and the effect of valence charge on solute dispersion was not considered. Recent nanoscale electrophoretic separation studies [Pennathur and Santiago (2005a), Pennathur and Santiago (2005b), Garcia et al. (2005)] involved relatively low Peclet numbers ($Pe < 0.7$), and thus axial molecular diffusion dominated dispersion and ionic dispersion effects were not observed.

In the following sections, an analytical solution and numerical model for ionic dispersion of charged and neutral species in nanochannels with finite EDL at larger Peclet numbers are developed, results are compared, effective diffusion coefficients and dispersion coefficients are quantified, and unique diffusive mechanisms are established.

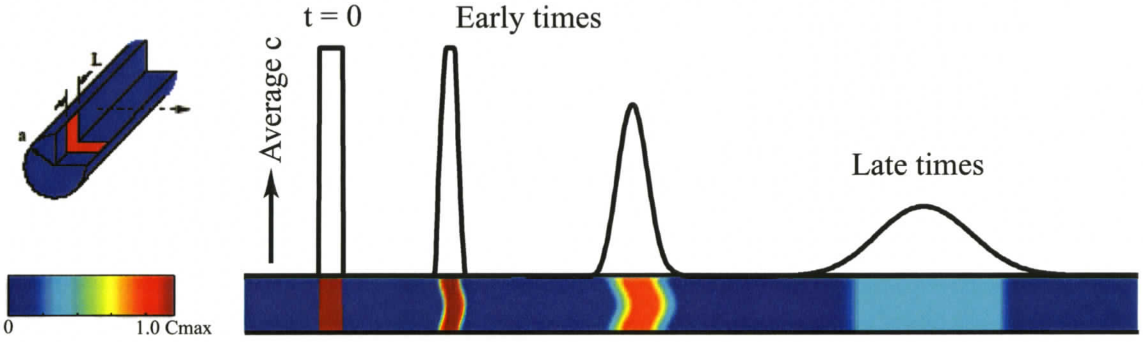

Figure 2.1 Schematic illustrating Taylor dispersion. A discrete solute sample of length *L* undergoing Taylor dispersion in a circular cross-section channel of radius *a* is shown at time t = 0, at early times and at late times. Corresponding average concentration (average c) profiles are shown above. At early times dispersion is convection dominated and at later times, axial convection is balanced by radial diffusion resulting in pluglike flow and a Gaussian concentration profile. The concentration scale is shown at the left. Cmax is the maximum solute concentration.

2.2 Analytical Solution

The Debye length that characterizes the thickness of the EDL is [Probstein (1994)]

$$\lambda_D = \left(\frac{\varepsilon k T N_A}{2 z_e^{\,2} F^2 c_\infty} \right)^{1/2} \quad (2.1)$$

where λ_D is the Debye length, ε is the electrical permittivity (product of the relative permittivity, ε_r, and the permittivity of a vacuum ε_o = 8.8542x10^{-12} CV^{-1}m^{-1}), k is the Boltzmann constant (1.3807x10^{-23} J K^{-1}), T is temperature, N_A is Avogadro's Number (6.022x10^{23} mol^{-1}), z_e is the valence of the ions comprising the bulk electrolyte, F is Faraday's constant (96485 C mol^{-1}), and c_∞ is the concentration of the bulk electrolyte. Debye lengths are typically on the order of 10 nm, and thus the thin EDL assumption $(\lambda_D / a << 1)$ common in microfluidics, is not generally applicable to nanoscale flows.

Electrokinetic theory governing the EDL and specific interactions with bulk fluid motion is well established [Burgreen and Nakache (1964), Rice and Whitehead (1965), Attard et al. (2000)]. For zeta potentials with an absolute value less than 50 mV, the Poisson-Boltzmann equation may be made linear according to the Debye-Hückel approximation as in [Rice and Whitehead (1965)]

$$\frac{1}{r}\frac{d}{dr}\left(r \frac{d\psi}{dr} \right) = \frac{\psi(r)}{\lambda_D^2} \quad (2.2)$$

where r is the radial coordinate, and ψ is the electric potential due to the EDL. Finite ion size and interaction effects as elucidated by other theories [Attard et al. (2000), Van Theemsche et al. (2002)] contribute negligibly at these low potentials. The electrical potential due to the EDL may be expressed as [Rice and Whitehead (1965)]

$$\psi(r) = \zeta \frac{I_o(r/\lambda_D)}{I_o(a/\lambda_D)} \qquad (2.3)$$

where ζ is the zeta potential at radial coordinate $r = a$, and I_o is the zeroth-order modified Bessel function of the first kind. The zeta potential may be related to the surface charge density, σ, by integration of the Poisson-Boltzmann equation with the result,

$$\zeta = \left(\frac{\sigma a}{\varepsilon}\right)\left(\frac{\lambda_D}{a}\right)\frac{I_o(a/\lambda_D)}{I_1(a/\lambda_D)} \qquad (2.4)$$

where I_1 is the first-order modified Bessel function of the first kind, and the first bracketed term provides a potential parameter, $\zeta_o = \sigma a/\varepsilon$. The magnitude of the electric field in the EDL is orders of magnitude higher than the axially applied electric fields considered here, and thus the EDL potential and the applied electric field may be considered separately [Ghosal (2004)]. Van Theemsche et al. (2002) demonstrate the continued validity of this assumption in cases where the EDL thickness is on the order of the channel hydraulic diameter, and this treatment is also supported by nanofluidic experimental studies [Pennathur and Santiago (2005b), Garcia et al. (2005)].

The velocity profile resulting from steady, combined pressure driven and electroosmotic flow of an incompressible, Newtonian fluid is given by [Rice and Whitehead (1965)]

$$u(r) = u_{eo}\left(1 - \frac{\psi(r)}{\zeta}\right) + 2u_{pd}\left(1 - \frac{r^2}{a^2}\right) \qquad (2.5)$$

where $u_{eo} = -\varepsilon\zeta E/\mu$ is the Helmholtz-Smoluchowski velocity, E is the axially applied electric field, μ is the viscosity of the liquid, $u_{pd} = a^2/8\mu(-dp/dx)$ is the average pressure driven flow velocity, and dp/dx is the axial pressure gradient.

The species conservation equation governing ionic transport in a straight channel of circular cross-section is [Probstein (1994)]

$$\frac{\partial c}{\partial t} + (u(r) + \nu_{im} zFE)\frac{\partial c}{\partial x} = \nu_{im} zF \frac{1}{r}\frac{\partial}{\partial r}(rc\frac{\partial \psi}{\partial r}) + D\frac{1}{r}\frac{\partial}{\partial r}(r\frac{\partial c}{\partial r}) + D\frac{\partial^2 c}{\partial x^2} \quad (2.6)$$

where c is the concentration of solute species, ν_{im} is the ionic mobility, z is the valence charge of the solute, x is the axial coordinate, and D is the molecular diffusion coefficient. It is assumed that the solute species is non-reacting and dilute relative to the bulk electrolyte. In the absence of an axially applied electric field or pressure gradient, no bulk fluid velocity is generated ($u(r) = 0$), and charged species will be radially distributed in response to the EDL as shown in the schematic in Figure 2.2a. Axial cross-section concentration plots of discrete samples of counter-ion (z = +2), neutral, and co-ion (z = -2) solutes in a channel with negative surface charge ($\zeta_o = \sigma a/\varepsilon$ = - 90 mV) are shown for the cases of moderate EDL thickness, λ_D/a = 0.05 (Figure 2.2b), and thick EDL, λ_D/a = 0.40 (Figure 2.2c). In both cases attraction of the counter-ions to the oppositely charged surface results in their increased concentration near the wall, whereas neutral species are unaffected and co-ions are concentrated more into the interior of the channel. The degree of ionic concentration, however, increases with the thickness, or ‘reach’, of the EDL. In the absence of a bulk velocity, these samples diffuse axially while maintaining a Boltzmann-type radial concentration distribution that results from a balance between radial electromigration (in response to the wall charge) and radial diffusion.

Electroosmotic velocity profiles resulting from an axially applied electric field are shown on the right side of Figure 2.2b and 2.2c. The moderate EDL case results in large velocity gradients near the wall and an effectively uniform velocity in the channel centre. In contrast, the velocity profile in the thick EDL case resembles more the parabolic form characteristic of pressure driven flow [Rice and Whitehead (1965)]. The coupled effect of the substantial EDL on both the cross-stream ionic concentration and velocity profile, results in solute velocities that differ significantly from that in an otherwise similar microscale channel [Pennathur and Santiago (2005a), Pennathur and Santiago (2005b), Garcia et al. (2005)]. This effect is shown schematically in Figure 2.2a. Specifically, the counter-ion is preferentially concentrated in the near-wall region where the fluid velocity is less than in the centre portion of the channel where the co-ion is concentrated. Thus a counter-ion solute tends to have a lower convective velocity than a neutral or co-ion solute. The average net solute velocity may be expressed as

$$u_{avg} = \frac{\langle Bu(r) \rangle}{\langle B \rangle} + v_{im} zFE = u_{CA} + v_{im} zFE \qquad (2.7)$$

where $\langle ... \rangle = 2a^{-2} \int_0^a ...rdr$ indicates an average over the cross-sectional area, $B = \exp\left(-ez(\psi - \psi_c)/(kT)\right)$, e is the charge on an electron (1.6022x10^{-19} C), and ψ_c is the electric potential at the channel centerline. As indicated, the average net solute velocity is a combination of the concentration weighted area-averaged velocity (u_{CA}) and the electrophoretic velocity ($v_{im} zFE$). In the case of electrokinetically driven flow with zero pressure gradients, equation 2.7 agrees with solute velocities defined previously [Pennathur and Santiago (2005a), Pennathur and Santiago (2005b), Garcia et al. (2005)]. For neutral species equation 2.7 simplifies to the bulk-averaged velocity.

The early period in the dispersion process occurs on a time scale, $t < \tau = a^2 / D$ [Taylor (1953)]. In nanofluidics this early period is particularly brief; for the case of small ions in channels with diameters on the order of 10 nm, τ is on the order of microseconds. Following Taylor (1953), the flow at much later times ($t >> \tau = a^2 / D$) is assumed to be quasi-steady with respect to axes moving with velocity u_{avg} and concentration variation with respect to these axes is purely radial. Furthermore, for axial band length, L, much larger than the channel radius ($L >> a$), radial molecular diffusion and electromigration dominate over axial diffusion. Implementing these assumptions and replacing x with a moving coordinate, $x' = x - u_{avg}t$, equation 2.6 becomes

$$(u(r) + v_{im}zFE - u_{avg})\frac{\partial c}{\partial x'} = v_{im}zF\frac{1}{r}\frac{\partial}{\partial r}(rc\frac{\partial \psi}{\partial r}) + D\frac{1}{r}\frac{\partial}{\partial r}(r\frac{\partial c}{\partial r}) \qquad (2.8)$$

At the channel centerline, r = 0, the boundary conditions $\partial c / \partial r = 0$, $\partial \psi / \partial r = 0$, and $\psi = \psi_c$ are applied and a centerline solute concentration, $c = c_{CL}(x)$, is defined. Solving the differential equation 2.8, using these boundary conditions gives the following solution:

$$c(r,x) = B[c_{CL}(x) + h/D] \qquad (2.9)$$

where $$h = h(r,\frac{\partial c}{\partial x'}) = \int_0^r B^{-1}\left(\frac{1}{r'}\int_0^{r'} r''u'(r'')\frac{\partial c}{\partial x'}dr''\right)dr',$$ and

$u'(r) = u(r) + vzFE - u_{avg} = u(r) - u_{CA}$ is the solute velocity with respect to the moving axis. The term $\partial c / \partial x'$ appearing in the function *h* is a function of *r* and $\partial \bar{c} / \partial x'$ where $\bar{c}$ is the cross-section-area-averaged concentration given by

$$\bar{c} = c_{CL}(x)\langle B \rangle + \langle B \cdot h/D \rangle \qquad (2.10)$$

Using equation 2.10 to solve for c_{CL} in equation 2.9 gives

$$c(r,x) = B\left[\frac{\bar{c}}{\langle B \rangle} - \frac{\langle Bh\ D \rangle}{\langle B \rangle} + h/D\right] \qquad (2.11)$$

Differentiating equation 2.11 with respect to *x'* gives

$$\frac{\partial c}{\partial x'} \approx \frac{\partial \bar{c}}{\partial x'}\frac{B}{\langle B \rangle} \qquad (2.12)$$

where the last two terms in equation 2.11 are assumed small, when differentiated with respect to *x'*, compared to the remaining terms in equation 2.12. This follows from the earlier assumption that axial diffusion ($\partial^2 c / \partial x'^2$) is small compared to radial diffusion and electromigration. From the cross-section-averaged mass flux in the channel relative to the moving axis, an effective diffusion coefficient, D_{eff} may be calculated as [Probstein (1994)]

$$D_{eff} = -\langle cu'(r) \rangle \left(\frac{\partial \bar{c}}{\partial x'}\right)^{-1} \qquad (2.13)$$

Combining equations 2.11-2.13, the effective diffusion coefficient can be expressed relative to the molecular diffusion coefficient as

$$\frac{D_{eff}}{D} = \frac{-1}{D}\left\langle \frac{B}{D}\left[\int_0^r B^{-1}\left(\frac{1}{r'}\int_0^{r'} r''u'(r'')\frac{B}{\langle B \rangle}dr''\right)dr'\right] \cdot u'(r) \right\rangle \qquad (2.14)$$

The effective diffusion coefficient defined above varies linearly with Peclet number squared, where Peclet number is based on the bulk-averaged fluid velocity,

$Pe = \langle u(r) \rangle a / D$; in keeping with dispersion studies of neutral solutes [Taylor (1953), Griffiths and Nilson (1999), Datta and Kotamarthi (1990)]. Dispersive effects of axial molecular diffusion may be accommodated as well, by expressing the effective diffusion coefficient as

$$\frac{D_{eff}}{D} = 1 + fPe^2 \qquad (2.15)$$

where f is the dispersion coefficient given by

$$f = \frac{-\left\langle B\left[\int_0^r B^{-1}\left(\frac{1}{r'}\int_0^{r'} r''u'(r'')\frac{B}{\langle B\rangle}dr''\right)dr'\right]\cdot u'(r)\right\rangle}{\left[\langle u(r)\rangle \cdot a\right]^2} \qquad (2.16)$$

A dimensional analysis in parallel with the above derivation results in

$$f = \frac{-\left\langle B\left[\int B^{-1}\frac{1}{r^*}\left(\int r^* u'^* \frac{B}{\langle B\rangle}dr^*\right)dr^*\right]u'^*\right\rangle}{\left(\langle u^*\rangle\right)^2} \qquad (2.17)$$

where $\langle \ldots \rangle = 2a^{-2}\int_0^a \ldots r dr = 2\int_0^1 \ldots r^* dr^*$, $r^* = r/a$, $B = \exp\left(-ez\zeta_o(\psi^* - \psi_c^*)/(kT)\right)$, $\zeta_o = \sigma a/\varepsilon$, $\psi^* = \psi/\zeta_o$, $u^* = u(r)/u_{ref}$, and $u'^* = u'(r)/u_{ref}$. A convenient reference velocity may be chosen depending on the application, for example, $u_{ref} = u_{eo} = -\varepsilon\zeta E/\mu$ for electrokinetically-driven flow or $u_{ref} = u_{pd} = a^2/8\mu\left(-dp/dx\right)$ for pressure driven flow, or a combination thereof for mixed flow applications. The dimensional analysis reveals that the dispersion coefficient, f, is a function of only a valence parameter, $Z = (ez\zeta_o)/(kT) = (ez\sigma a)/(kT\varepsilon)$, and the relative EDL thickness, λ_D/a, in addition to the specific form of the velocity profile.

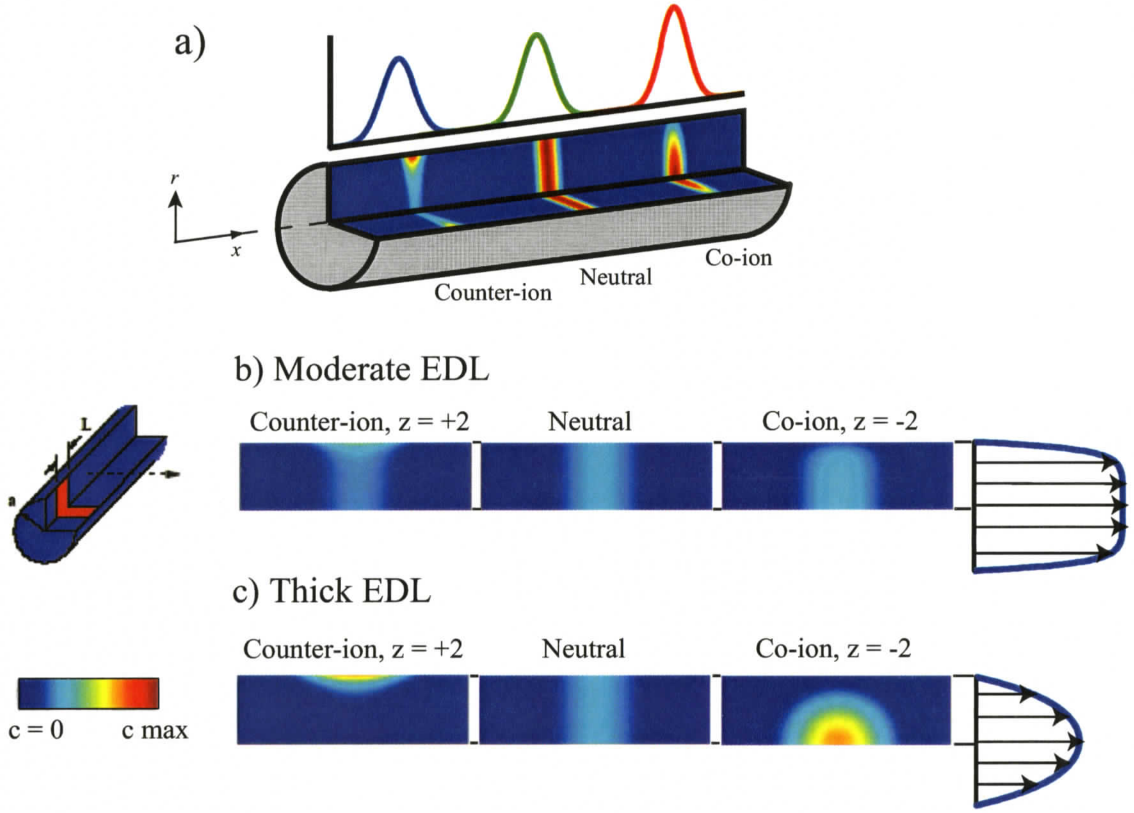

Figure 2.2 a) Schematic illustrating the geometry of interest and the coupled effect of substantial EDL on cross-stream ionic concentration at late times. Axial cross-section concentration plots of discrete samples of counter-ion (z = +2), neutral (z = 0), and co-ion (z = -2) solutes are plotted for the cases of b) Moderate EDL, λ_D/a = 0.05 and c) Thick EDL λ_D/a = 0.40. The same concentration scale and initial conditions were applied in both cases to facilitate direct comparison with respect to ion segregation. On the right, electroosmotic velocity profiles that would result from an axially applied electric field are plotted for each case. The concentration field data was calculated here with a commercial computational fluid dynamics modeling package (COMSOL MULTIPHYSICS, COMSOL Inc., Stockholm Sweden), for the case of $\zeta_o = \sigma a / \varepsilon =$ -90mV, details on the numerical model are provided in Section 2.3.

2.3 Numerical Model

A continuum based numerical model of ionic dispersion in nanochannels is developed here to provide a comparison for and extension of the analytical solution, and quantification of the Debye-Hückel approximation (linearization of the Poisson-Boltzmann equation). The numerical model differs from the analytical solution by using the nonlinear Poisson Boltzmann equation (equation 1.9), which allows larger zeta potential and therefore larger relative electric double layer thickness cases to be investigated; in addition the model will be 2-dimensional. The analytical solution using the linearized Poisson Boltzmann equation (equation 2.2) is limited to a maximum zeta potential of 50 mV and a maximum relative EDL thickness of 0.4. The 2-dimensional axisymmetric numerical model is implemented using COMSOL 3.2 with MATLAB (COMSOL MULTIPHYSICS, COMSOL Inc., Stockholm, Sweden), a well developed finite element method software package that runs well on a PC. The software contains modules specific to microflows and allows for multiphysics modeling such as combining electrostatic, liquid flow, and mass transport simulations. The steady state electrostatics and Navier Stokes equations are modeled followed by the time dependent mass transport equations. Laminar flow of an incompressible, Newtonian liquid solute introduced into an electrolyte is simulated. The solute and the electrolyte are dilute enough in aqueous solution that using the properties of water can be justified. The solute is assumed to be infinitely dilute and therefore only the bulk electrolyte contributes to the formation of the EDL. The liquid properties are constant at 25°C: the density is 997 kg m^{-3}, the relative permittivity is 78.4, the viscosity is 0.8909×10^{-3} kg m^{-1} s^{-1}, and the molecular diffusion coefficient is $1x10^{-10}$ m^2 s^{-1}. It is assumed that the channel walls are charged uniformly with a negative surface charge density specified as a boundary condition.

Details on the solution of each variable are provided in the sections to follow. In this paragraph an overview of the key aspects of the numerical model is provided. Briefly, the numerical model is solved as follows: first the two electrostatics simulations are run in parallel to solve for the applied electric field, $\bar{E}$, and the electric potential due to the EDL, ψ. Second, the results of the electrostatics simulations are input into the liquid flow simulation to solve for axial velocity, $\bar{u}$. Lastly, the results of the electrostatics and liquid flow simulations are input into the species transport simulation and it is solved for the concentration distribution, $c(r,x,t)$. The species transport results do not effect the bulk velocity profile since the solute is assumed dilute with respect to the bulk electrolyte. The channel lengths are on the order of 10 μm and diameters are on the order of 50 nm. Axisymmetric geometry enables modeling of 3-dimensional phenomena with a 2-dimensional model. The model solution made use of one way coupling between the electric fields, flow field and concentration field. Specifically, the electric field solution was applied in the flow field solution and both were applied in the solution of the concentration field. However, the concentration field did not influence either the electric or flow fields as the solute was dilute. The steady state electric and flow fields prevailed while the species conservation equation was solved in a time dependent manner. The time dependent simulation was stopped when consistent values of effective diffusion coefficient were obtained. Also, in the solution of the concentration field a moving computational domain was employed. In order to concentrate computing power on the translating solute, the computational domain was translated at a constant velocity approximately equal to the average net solute velocity, u_{avg}. Due to solute interactions with the EDL, as discussed earlier (Section 2.2), this velocity was not always known a priori. Instead, an estimate was made for initial iterations and if significant solute mass was lost (i.e. ~ 1%) via the boundaries, the domain was corrected and the model re-run. In general, 2-dimensional field data was calculated for each variable in order to facilitate easy integration into the species transport model. Fundamental dimensional dependencies, however, may be summarized as follows; applied electric field, $E(x)$, electric potential due to the EDL, $\psi(r)$, velocity, $u(r)$, and concentration field, $c(r,x,t)$. Typical solutions required 80 s on a Pentium® 4 PC with 512 MB of RAM.

2.3.1 Electrostatic Field Solution

The simulation for the electric potential due to the EDL is solved using the Electrostatics module in COMSOL software with a steady state non-linear solver, since the nonlinear Poisson Boltzmann equation is being implemented. The equation modeled is as follows,

$$\nabla^2\psi = \frac{-\rho_E}{\varepsilon} \quad (2.18)$$

where $\rho_E = -2\varepsilon F c_\infty \sinh\left(\frac{e\psi}{kT}\right)$ is the net charge density, and ψ is the electric potential due to the presence of the electric double layer and is a function of radial coordinate only, $\psi(r)$. The outer wall surface charge density is given by the boundary condition,

$$\bar{n}\cdot\bar{\nabla}\psi = \frac{-\sigma}{\varepsilon} \quad (2.19)$$

where $\sigma = -2.5\text{x}10^{-3}$ C m^{-2} is the surface charge density, and $\bar{n}$ is a unit vector normal to the wall. There is axial symmetry about the channel centerline, and the inlet and outlet are set as electrically insulating boundary conditions.

In parallel with the electric potential due to the EDL simulation, a second electrostatics simulation solves the electric potential due to the axially applied electric field for the electrokinetically driven flow case. This simulation is not required when pressure driven flow is modeled (i.e. when there is no externally applied electric field). The equation solved is as follows,

$$\nabla^2\phi = 0 \qquad (2.20)$$

where ϕ is the electric potential due to the applied electric field. The boundary condition on the wall is for electrical insulation and, again, there is axial symmetry at the channel centerline. The electric potential at the inlet is set to a constant value so that a steady axially applied electric field is generated, the outlet is grounded.

2.3.2 Bulk Fluid Velocity Solution

For the liquid flow simulation, the incompressible Navier Stokes module is used and solved with a steady state non-linear solver. This module solves the incompressible continuity and Navier Stokes equations,

$$\bar{\nabla}\cdot\bar{u} = 0 \qquad (2.21)$$

$$\rho\frac{\partial\bar{u}}{\partial t} + \rho(\bar{u}\cdot\bar{\nabla})\bar{u} = -\bar{\nabla}p + \mu\nabla^2\bar{u} + \bar{F} \qquad (2.22)$$

where $\bar{F}$ is a body force vector and $\bar{u}$ is the velocity vector. Since the simulation is solved for steady state the first term in equation 2.22 goes to zero. The body force in the channel for electrokinetically driven flow is the electrostatic Lorentz force [Santiago (2001)],

$$\bar{F} = \rho_E \bar{E} \qquad (2.23)$$

where $\bar{E} = -\bar{\nabla}\phi$. For pressure driven flow, $\bar{F} = 0$. The no slip condition $\bar{u} = 0$ is applied at the channel wall and there is axial symmetry at the centerline. For electrokinetically driven flow, the inlet and outlet pressure are set to zero and therefore internal pressure gradients are zero. For pressure driven flow, an inlet pressure is specified and outlet pressure is maintained at zero producing a linear axial pressure distribution in the channel.

2.3.3 Species Transport Solution

The results from the electric field and fluid velocity simulations are input into the time-dependant species transport simulation. The electrokinetic flow module in COMSOL software is used to solve the mass transport equation using a time dependent solver. As in the analytical solution, a uniform-concentration, discrete sample of solute species with a valence of +2, +1, 0, -1, or -2 is inserted into the bulk electrolyte at time zero. The solute is assumed to have the same properties as water and to be dilute compared to the bulk electrolyte so that the addition of the solute does not affect the electric double layer. The following mass transport equation is solved for the solute species,

$$\frac{\partial c}{\partial t} + \bar{u} \cdot \nabla c = D\nabla^2 c + v_{im} zF\nabla \cdot (c(\nabla \phi + \nabla \psi)) \qquad (2.24)$$

The values for $\bar{\nabla}\psi$ and $\bar{\nabla}\phi$ come from the previous electrostatic simulations and $\bar{u}$ is from the liquid flow simulation; it is adjusted to have a moving coordinate system as in the analytical solution. For pressure driven flow, the value $\bar{\nabla}\phi$ is zero. An insulation boundary condition is applied at the wall, or in other words, no mass crosses the walls. The inlet concentration is zero and a convective flux boundary condition is applied at the outlet. At time zero, a solute with assigned concentration $c / c_o = 1$ and length L_o is located mid-channel and starts to flow; c_o is the solute concentration and L_o = 2.5 μm is the solute sample length at time zero. The solute concentration data is calculated in the model as a dimensionless ratio c / c_o and is used to calculate the effective diffusion coefficient and dispersion coefficient, as described in the next section.

2.3.4 Calculation of D_{eff} and f from Numerical Simulation Output

The output of the numerical model is an array of two-dimensional (radial, axial) concentration field data at a set time step, i.e. a discrete representation of $c(r,x,t)$. Plots of this raw output over a typical dispersion process, at late times, are provided in Figure 2.1 for Taylor dispersion and Figure 2.3 for ionic dispersion in pressure driven flow. In order to compare numerical model results with results of the analytical solution, these relatively high resolution results must be generalized through calculation of an effective diffusion coefficient, D_{eff}, and dispersion coefficient, *f*, where $D_{eff} = 1 + fPe^2$. The Peclet Number is calculated as follows from the numerical model results,

$$Pe = \frac{\langle u \rangle a}{D} \qquad (2.25)$$

The cross sectional area average bulk velocity, $\langle u \rangle$, is calculated by equation 2.26 in MATLAB (Mathworks Inc., MA), a problem solving software package, using the Trapezoidal rule and velocity data exported from the numerical model.

$$\langle u \rangle = \frac{2}{\pi a^2} \int_0^a u(r) \pi r dr \quad (2.26)$$

The effective diffusion coefficient as described in the analytical solution can be calculated using concentration data from the model. The concentration data is exported to MATLAB where the cross-sectional area averaged concentration $\langle c \rangle / c_o$ is calculated using the Trapezoidal rule, the same method in which $\langle u \rangle$ is calculated. Concentration cross-sectional averaged results were axially Gaussian as in the classical Taylor dispersion solution. The Taylor equation relating effective diffusion coefficient to cross sectional area averaged concentration [Probstein (1994), Taylor (1953)] is as follows,

$$\frac{\langle c \rangle}{c_o} = \frac{n_o / c_o \pi a^2}{2(\pi D_{eff} t)^{1/2}} \exp\left(-\frac{(x - u_{avg} t)^2}{4 D_{eff} t} \right) \qquad (2.27)$$

The number of moles of the solute species, n_o, is the concentration of the solute species multiplied by the volume of the sample at $t = 0$,

$$n_o = (c_o)(\pi a^2)(L_o) \qquad (2.28)$$

The moving coordinate $x - u_{avg} t$ is equal to zero when the average concentration, $\langle c \rangle / c_o$, is at its maximum. Taking this into account, equation 2.27 can be re-written to solve for D_{eff} as follows,

$$D_{eff} = \frac{1}{\pi t}\left(\frac{L_o}{2\langle c\rangle_{\max}/c_o}\right)^2 \qquad (2.29)$$

where $\langle c\rangle_{\max}/c_o$ is the maximum area averaged concentration. Since the maximum average concentration is known from the mass transport model results, equation 2.29 can be used to calculate the effective diffusion coefficient for ionic dispersion. The dispersion coefficient f is then related to the effective diffusion coefficient and the Peclet number by equation 2.15. In figure 2.4, a sample plot of D_{eff}/D versus Pe^2 is shown. In all cases tested the slope was constant indicating a linear relationship between D_{eff}/D and Pe^2. The dispersion coefficient was determined from the slope of these lines.

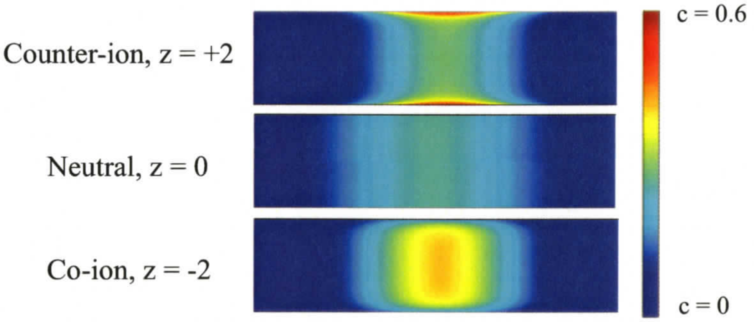

Figure 2.3 Schematic illustrating ionic dispersion of counter-ions, neutral species, and co-ions at late times in pressure driven flow when $\lambda_D / a = 0.1$. The concentration scale is shown at the right.

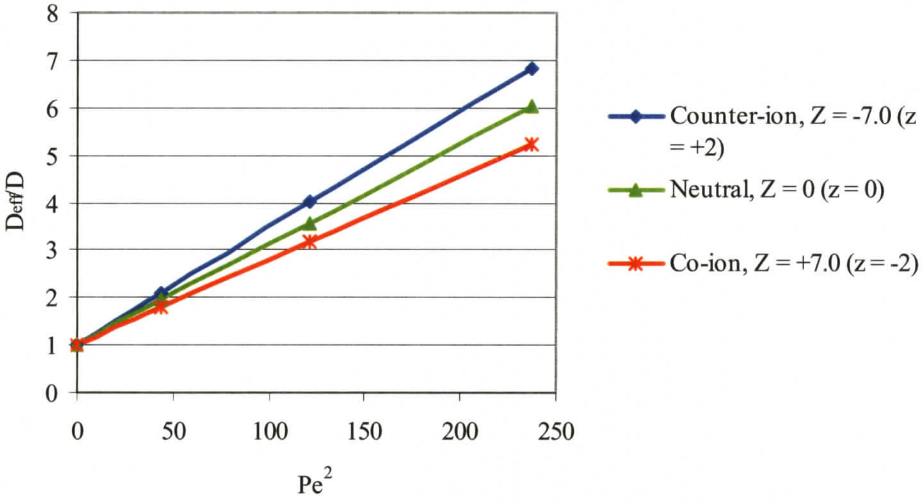

Figure 2.4 Plot of D_{eff} / D versus Pe^2 showing a linear relationship for the case of pressure driven flow with $\lambda_D/a = 0.1$. The slope of the straight line gives the value of the dispersion coefficient, *f*.

2.3.5 Mesh Analysis

Concentration is the most computationally demanding variable since it must be solved in both spatial dimensions as well as time. In addition, large (effectively infinite) concentration gradients exist at the edges of the discrete sample at $t = 0$. The concentration value also depends on the electrostatic and velocity solutions and particularly for the counter-ion case (an example is shown in Figure 2.2), the presence of the EDL results in intense cross-stream electromigration and resulting high cross-stream gradients near the wall. A finite element mesh analysis was performed to determine an appropriate number of mesh elements to use in the channel geometry taking model accuracy and solution time into account. The maximum concentration a short time later (say $1\text{x}10^{-6}$ sec) is used to measure the numerical error produced. The maximum concentration can deviate from a physical maximum ($c/c_o = 1$ in the case of a neutral solute) due to interpolation errors between sharp gradients. This numerical artifact is common in time dependent solvers and indicates insufficient discretization only. Errors of less than 1% were considered admissible here. As solution error decreases, solution time increases. Many simulation runs (hundreds) were required to obtain data for each solute charge, relative electric double layer thickness, applied electric field and pressure gradient studied. The results of the mesh analysis are shown in Table 2.1.

Number of mesh elements	Solution time (s)	Error (%)
972	5.8	4.3
3888	16.7	1.8
15552	77.8	0.0
62208	No solution	-

Table 2.1 Mesh analysis results. The solution time and error are given for successive mesh refinements in an axisymmetric geometry with a radius of 25 nm and length of 20 μm.

Table 2.1 shows that for successive mesh refinements, the error decreases but solution time increases. For the case with 62208 mesh elements, no solution was obtained because an "out of memory" error occurred; this case was too demanding for the PC employed (512 MB of RAM, 2.80 GHz). The case with 15552 mesh elements resulted in a solution with an error of less than 1% and solved within a relatively short period (77.8 s) so it was not necessary to have a further mesh refinement to 62208 elements. 15552 mesh elements produced an approximation to the solution that was sufficient.

Other modeling challenges included the discretization of long thin geometries. In this model, geometries with a radius of 25 nm compared to a length of 20 μm were used – a three order of magnitude difference in dimensions. Data in both the axial and radial directions needed to be resolved. COMSOL software has several grid adaptation parameters that can be utilized for modeling long thin geometries, one parameter involves the resolution of narrow regions and the other an r-direction scaling factor. The resolution of narrow regions controls the number of layers of elements created in narrow regions of the geometry. The r-direction scaling factor allows anisotropic meshes to be generated that are useful in long thin geometries. The r-direction scaling factor controls the aspect ratio of the mesh elements. For example, using an r-direction scaling factor of five means the radial extent of each element will be five times less than in the axial extent. For the particular model geometry presented in this thesis, mesh elements were approximately 2.5 nm in the radial direction and 13 nm in the z-direction, on average, when 15552 mesh elements were used. When the resolution of narrow regions is set to 2, then on each successive mesh refinement the number of mesh elements in the radial direction is doubled. Setting the r-direction scaling factor to 5 and the resolution of narrow regions to 2 resulted in 972 additional mesh elements on the first refinement. After several mesh refinements, 15552 mesh elements resulted and a sufficient solution approximation as indicated in Table 2.1.

A more independent validation of the numerical model simulations is provided by direct comparison of final output with the analytical solution. These comparisons are provided in the following results section.

2.4 Results

2.4.1 Results of Analytical Solution

The dispersion coefficient for the analytical solution may be calculated readily from equation 2.16 or 2.17 through direct numerical integration with common mathematical software tools. MATLAB was applied here, requiring less than one second computational time for each case when running on a typical desktop PC. The dispersion coefficient, *f*, for counter-ions, co-ions and neutral solutes is plotted versus relative EDL thickness, λ_D/a, for the cases of pressure driven flow, and electrokinetically driven flow in Figures 2.5 and 2.6, respectively. General applicability of the ionic dispersion results is facilitated through the non-dimensional valence parameter, *Z*. The range of $Z = 7.0$ to -7.0 was selected to correspond to ions of valence charge, $z =$ -2 to +2, with $\zeta_o = \sigma a / \varepsilon = -90$ mV. Such a potential parameter results, for example, from an aqueous buffer solution within a channel of radius $a = 25$ nm, exhibiting a constant surface charge density, $\sigma =$ -2.5x10^{-3} C m^{-2}, typical of silica [Karnik et al. (2005), Daiguji et al. (2004b)].

The predicted dispersion coefficients for neutral species agree well with established theory. In the pressure driven flow case shown in Figure 2.5, the neutral solute ($z = 0$) is unaffected by the EDL and exhibits a constant dispersion coefficient, $f = 1/48 \cong 0.21$, as originally predicted by Taylor (1953). In the electrokinetically driven flow case shown in Figure 2.6, the neutral solute dispersion coefficient approaches zero in the thin EDL limit ($\lambda_D/a \to 0$) corresponding to ideal electroosmotic flow with a uniform velocity profile. As the EDL thickness increases, the electrokinetically driven velocity profile becomes increasingly parabolic (apparent in Figure 2.2), and the dispersion coefficient increases toward the classical Taylor value ($f = 1/48 \cong 0.21$) [Taylor (1953)]. The predicted curve is in agreement with the results of a previous study [Datta and Kotamarthi (1990)] (also plotted) of neutral solute dispersion with significant EDL effects.

Ionic dispersion differs significantly from that of neutral species in both the pressure driven flow (Figure 2.5) and electrokinetically driven flow (Figure 2.6) cases. The deviation in both cases may be explained by two unique effects: Firstly, the velocity gradients that induce the shearing action central to Taylor dispersion are highest near the channel walls. In this area, there is an increased concentration of counter-ions and a reduced concentration of co-ions (sample concentrations and velocity profiles are shown in Figure 2.2). Thus, a counter-ion concentration is exposed to a higher average shear rate than a co-ion concentration in the same flow. This charge-shear coupling dispersive effect, termed here, tends to increase the dispersion rate of counter-ions and decrease the dispersion rate of co-ions. Secondly, radial diffusion of ions is limited by electromigration in response to the wall charge. In contrast to neutral species that diffuse radially toward a uniform concentration distribution, ions may diffuse radially only to the extent determined by the Boltzmann equilibrium distribution. This electromigration dispersion-limiting effect, termed here, tends to decrease dispersion of all ions relative to neutral solutes, however, the effect is pronounced for counter-ions due to their high degree of concentration near the wall (the counter/co-ion segregation effect is also apparent in Figure 2.2).

Specifically in the pressure driven flow case (Figure 2.5), charge-shear coupling results in a dispersion coefficient for counter-ions that increases with relative EDL thickness over the range $0 < \lambda_D/a < 0.1$. A corresponding decrease is observed for co-ions, in proportion to valence charge. Beyond $\lambda_D/a = 0.1$ however, the electromigration dispersion-limiting effect becomes significant, and eventually dominating for counter-ions in thick EDL cases where the dispersion coefficients for the counter-ions approach that of their co-ion counterparts. The difference in dispersion coefficient between the $z = +2$ and $z = -2$ cases is over 40% at $\lambda_D/a = 0.15$. At $\lambda_D/a = 0.4$, the dispersion coefficients of both $z = +2$ and $z = -2$ cases are 35% less than that of a neutral solute in the same flow.

In electrokinetically driven flow (Figure 2.6), the role of ionic dispersion relative to a neutral solute is similar in trend to the pressure driven case. The charge-shear coupling effect is observed at moderate EDL thicknesses ($0 < \lambda_D/a < 0.15$), as counter-ions experience more dispersion and co-ions experience less dispersion than a neutral solute. It is noteworthy, however, that the dependence of the electrokinetically driven velocity profile on EDL thickness mitigates, to some extent, the charge-shear coupling effect. Specifically, the difference in shear rates between the near-wall and central region is most significant at lower EDL thicknesses, whereas the cross-stream segregation of co-ions and counter-ions is most significant at higher EDL thicknesses. As EDL thickness increases beyond $\lambda_D/a = 0.15$, the electromigration dispersion-limiting effect becomes significant, and as in the pressure driven case, eventually dominating for counter-ions. The result is lower dispersion coefficients for all ions at higher EDL thicknesses, where dispersion coefficients of the $z = +2$ and $z = -2$ cases are over 30 % and 40% less than that of a neutral solute, respectively. The most significant discrepancies between dispersion coefficients of co-ions and counter-ions occur in the range $0.1 \leq \lambda_D/a \leq 0.2$ where the $z = +2$ case is more than double that of the $z = -2$ case.

Akin to neutral solute dispersion in pressure driven [Taylor (1953)], electrokinetically driven [Griffiths and Nilson (1999), Griffiths and Nilson (2000b), Zholkovskij et al. (2003)] and mixed [Datta and Kotamarthi (1990), Dutta and Beskok (2001), Zholkovskij and Masliyah (2004)] flows, the impact of ionic dispersion in nanofluidics ultimately depends on the Peclet number, Pe, as indicated in equation 2.15. At very low Peclet numbers, dispersion is dominated by axial molecular diffusion. Both dispersive effects (axial molecular diffusion and Taylor-style dispersion) are significant at Peclet numbers larger than 0.7 [Probstein (1994)]. Peclet numbers in this range characterize nanofluidic flows with applied electric fields on the order of 1 kV/cm and pressure gradients on the order of 10^7 kPa/m (or higher). Nanoscale geometries afford the application of such fields, for instance, electric fields on the order of 10 kV/cm are not uncommon in membrane science [Siwy and Fulinski (2002), Kuo et al. (2001)], and axial pressure gradients on the order of 10^8 kPa/m may be generated readily in nanoscale channels [Daiguji et al. (2004a)]. Specifically in the context of electrophoretic analytical separations, higher electric field strengths can offer increased speed and separation efficiencies. Exploitation of this inherent characteristic of nanoscale geometries is a natural progression in the miniaturization of these technologies.

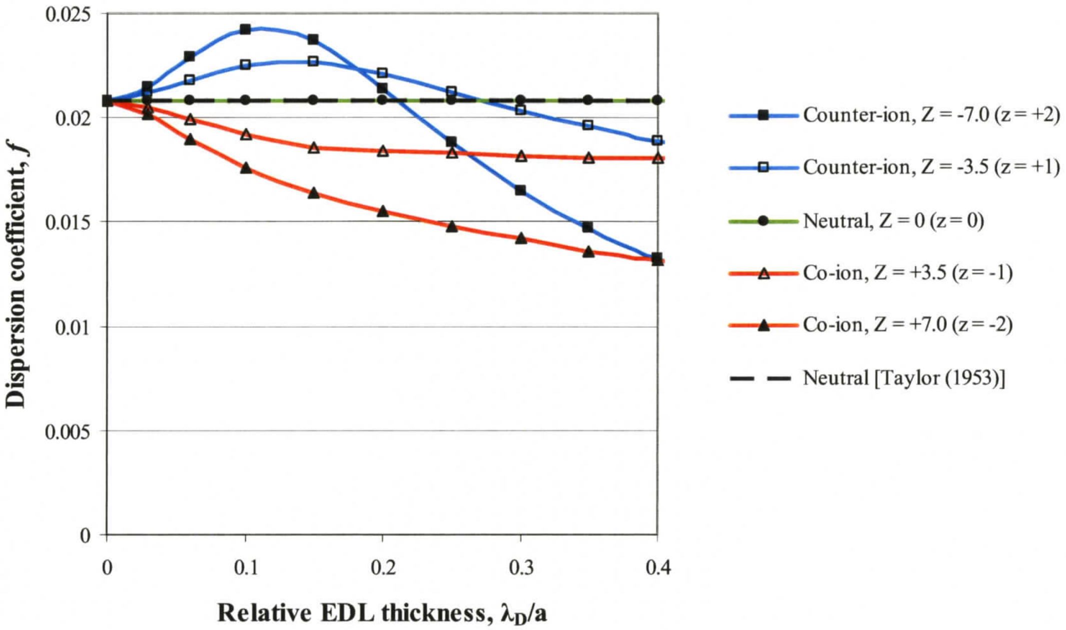

Figure 2.5 Analytical solution results for pressure driven flow at late times. Dispersion coefficient f resulting from pressure driven flow is plotted versus relative EDL thickness for counter-ions, co-ions and neutral solutes. Unaffected by the EDL, the neutral ($Z = z = 0$) case is co-linear with the Taylor limit ($f = 1/48 \cong 0.21$) [Taylor (1953)]. For ionic solutes, the effect of valence charge is generalized through the non-dimensional valence parameter, Z. The plotted cases of $Z = 7.0$ to -7.0 were selected to correspond to ions of valence charge, z = -2 to +2, with $\zeta_o = \sigma a / \varepsilon =$ -90 mV.

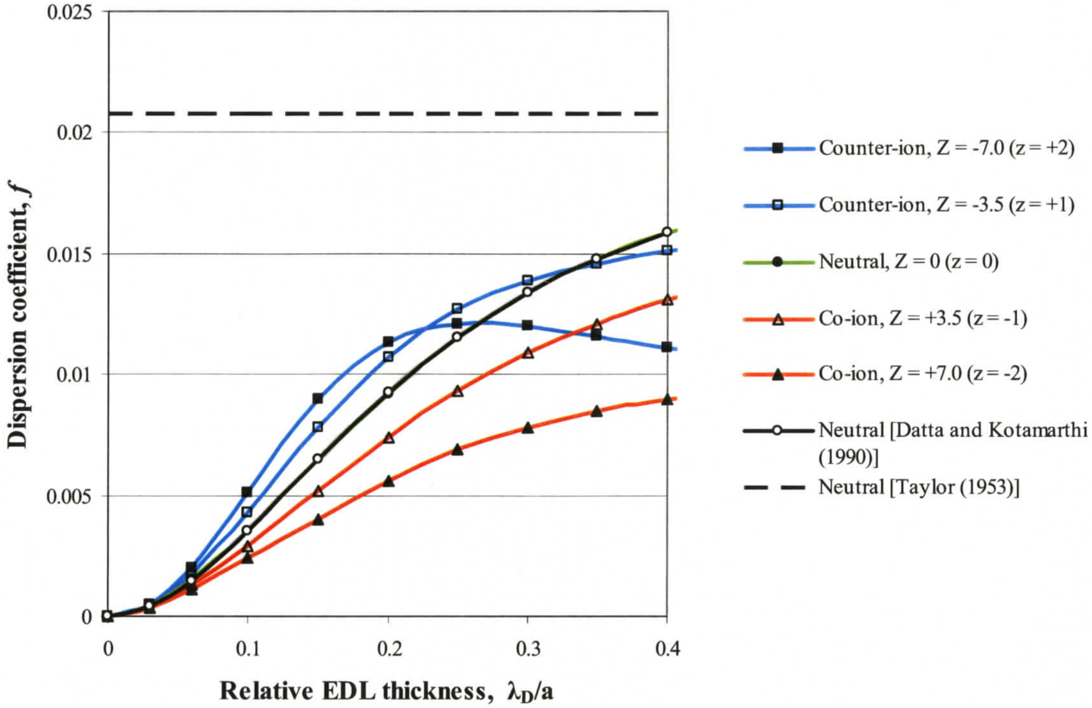

Figure 2.6 Analytical solution results for electrokinetically driven flow at late times. Dispersion coefficient *f* resulting from electrokinetically driven flow is plotted versus relative EDL thickness for counter-ions, co-ions and neutral solutes. Values of *f* for the neutral case ($z = 0$) agree with those calculated from a previous study for neutral solutes [Datta and Kotamarthi (1990)] (also plotted). The neutral species dispersion coefficient approaches the Taylor value ($f = 1/48 \cong 0.21$, plotted as a dashed line) [Taylor (1953)] as EDL thickness increases. For ionic solutes, the effect of valence charge is generalized through the non-dimensional valence parameter, *Z*, and the cases of $Z = 7.0$ to -7.0 correspond to ions of valence charge, $z = -2$ to +2, with $\zeta_o = \sigma a / \varepsilon = -90$ mV as in Figure 2.5.

2.4.2 Limitations of the Analytical Solution

With respect to limitations of the analytical solution, the relative EDL thickness range considered here, $0.05 \leq \lambda_D/a \leq 0.4$, is characteristic of nanofluidics. For example, this range corresponds to channel radii in the range, 120 nm $\geq d \geq$ 15 nm, for c_∞ = 10 mM, or to bulk ionic concentrations in the range, 60 mM $\geq c_\infty \geq$ 0.9 mM, in a channel of diameter $d = 50$ nm. In addition, both the continuum assumption and the Debye-Hückel approximation require consideration. The continuum assumption is generally considered appropriate for liquid flows in smooth walled channels greater than 5 nm in cross-sectional dimension [Eijkel and van den Berg (2005)]. In this analysis, the continuum assumption is valid to an upper limit of relative EDL thickness that is a function of the electrolyte concentration. A typical electric double layer thickness, given by equation 2.1, is 10 nm for an electrolyte but can be as large as 100 nm in distilled water; corresponding to upper limit relative EDL thicknesses of λ_D/a = 2 and λ_D/a = 20, respectively. These values are well above the range considered here.

The linearization of the Poisson-Boltzmann equation using the Debye-Hückel approximation (equation 2.2) is considered appropriate for zeta potentials less than 50 mV in magnitude [Rice and Whitehead (1965)]. Specifically, established EDL theories based on the linear, nonlinear and extended Poisson-Boltzmann formulations, as well as hypernetted chain theory differ significantly at higher surface charge densities due to finite ion size and interaction effects [Attard et al. (2000)]. However, below $|\sigma| = 5\text{x}10^{-3}$ C/m^2 ($|\zeta| \sim 50$ mV) these theories exhibit a linear dependence in close agreement with the linearized Poisson-Boltzmann equation applied here [Attard et al. (2000)]. In the context of this analysis, this approximation is valid to an upper limit on the potential parameter defined earlier, $\zeta_o = \sigma a / \varepsilon$, where the limiting potential is a function of relative EDL thickness (according to equation 2.4). In the most restrictive case considered, $\lambda_D / a = 0.4$, the assumption requires $|\zeta_o| \le 95.6\,\mathrm{mV}$. Given a surface charge density of $\sigma = -2.5\text{x}10^{-3}$ C/m^2, for example, and typical electrolyte permittivity, the restriction implies a channel size limit of $d \le 53$ nm. This represents the most restrictive case presented as the maximum potential parameter increases with decreasing relative EDL thickness. For the numerical model, the use of the nonlinear Poisson Boltzmann equation (equation 1.9) allows the analytical solution to be extended to larger zeta potential and larger values of λ_D / a. The nonlinear Poisson Boltzmann equation agrees well with the extended Poisson Boltzmann formulation and hypernetted chain theory up to a surface charge density of $20\text{x}10^{-3}$ C m^{-2} corresponding to a zeta potential of 120 mV in a 1 mM electrolyte [Attard et al. (2000)].

Both the analytical solution and numerical model assume a constant surface charge density at the channel wall that does not depend on the value of λ_D / a. Surface charge density at a surface results from an equilibrium between counter-ions on the surface and free ions in the bulk electrolyte and varies with proximity to other charge carrying surfaces and the material the surface is composed of, as well as the pH of the electrolyte [Behrens and Grier (2001), Kirby and Hasselbrink (2004)]. For a given pH value (for example pH = 6), for separations greater than $s / \lambda_D = 3$ where s is the separation distance between two charged surfaces, the surface charge density is approximately constant and does not vary with s / λ_D [Behrens and Grier (2001)]. If the separation distance, *s*, is set equal to the nanochannel diameter, *d*, the minimum separation distance can be represented as a maximum relative EDL thickness, $\lambda_D / a = 0.67$. Thus, relative EDL thickness in a nanochannel needs to be less than 0.67 so that surface charge density does not vary with λ_D / a. For values of $\lambda_D / a > 0.67$, surface charge density at the wall can still be applied as a constant boundary condition, but its value will need to be adjusted depending on λ_D / a. Here however, the numerical model is applied only to the range $0.05 \leq \lambda_D / a \leq 0.6$, where surface charge density is considered constant with respect to channel size.

2.4.3 Results of the Numerical Model and Comparison of Results with the Analytical Solution

The use of the linearized form of the Poisson-Boltzmann equation via the Debye-Hückel approximation limits the applicability of the presented analytical solution as discussed above. The numerical model of solute transport in the geometry of interest was implemented independently to cross-validate the analytical solution, quantify the effect of the Debye-Hückel approximation, and extend the results. Species transport in the axisymmetric domain was calculated directly from equation 2.24, the Navier-Stokes equations 2.21 and 2.22, and the Poisson-Boltzmann equation. Dispersion coefficients were determined from the concentration field data. As a first validation step, the linearized Poisson-Boltzmann equation was implemented in the computational model. The results of the analytical solution, and those of the computational model (with the linearized Poisson-Boltzmann equation) agreed to within 2% over the range of interest.

This result is significant as it provides cross-validation of the two independent techniques. The computational model was then implemented with the nonlinear Poisson-Boltzmann equation (equation 1.9).

Dispersion coefficients calculated from the computational model (with the nonlinear Poisson-Boltzmann equation) are compared with those of the analytical solution (with the linear Poisson-Boltzmann equation 2.2) for counter-ions, co-ions and neutral solutes in Figures 2.7 and 2.8, for the cases of pressure driven flow and electrokinetically driven flow, respectively. The analytical solution results are limited to $\lambda_D/a \leq$ 0.4 as before, whereas the results of the computational model extend to $\lambda_D/a =$ 0.6. Results agree very well overall with average standard deviations of 0.0004, and 0.0002 in the pressure driven and electrokinetically driven cases, respectively. The computational results reinforce the observations of a charge-shear coupling dispersive effect (tending to increase dispersion of counter-ions and decrease dispersion of co-ions) and at larger relative EDL thicknesses, an electromigration dispersion-limiting effect (tending to decrease dispersion of all ions, and particularly that of counter-ions). The influence of the Debye-Hückel approximation in the analytical solution is apparent as differences between the analytical (linear P-B) and computational (nonlinear P-B) increase with λ_D/a. At the upper limit defined earlier, $\lambda_D/a =$ 0.4, average error incurred was 7.0% and 5.6% for the pressure and electrokinetically driven cases, respectively. Extended computation results in the range $0.4 \leq \lambda_D/a \leq 0.6$ show a continued trend of charge-shear coupling and electromigration limited dispersion.

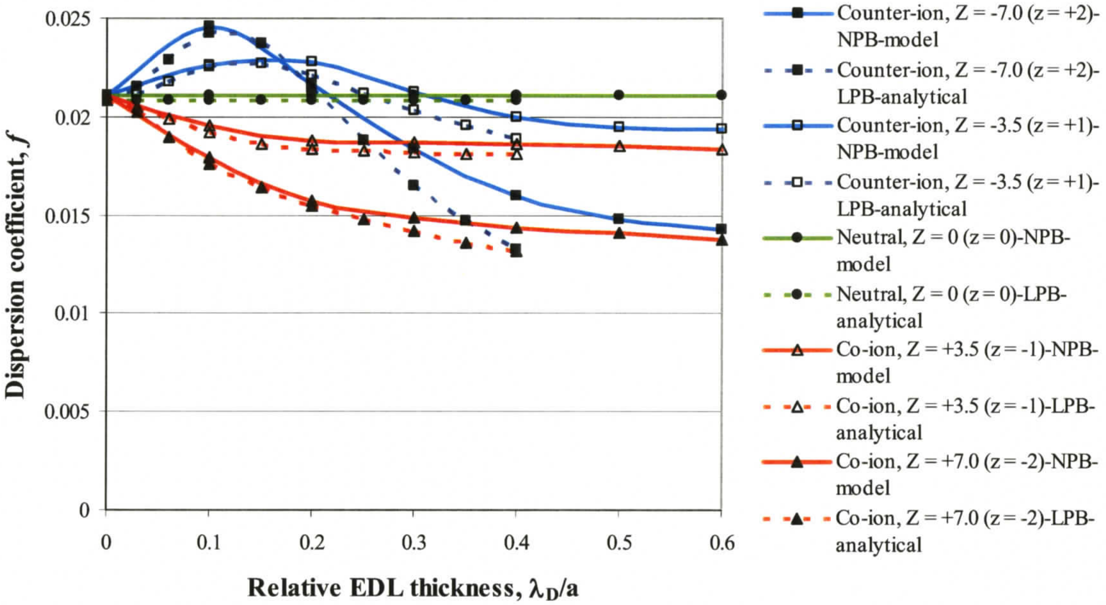

Figure 2.7 Numerical modeling and analytical solution results for pressure driven flow at late times. Dispersion coefficient *f* resulting from pressure driven flow is plotted versus relative EDL thickness for counter-ions, co-ions and neutral solutes comparing the computational model using the nonlinear Poisson Boltzmann (NPB) equation with the analytical model using the linear Poisson Boltzmann (LPB) equation. The analytical results stop at $\lambda_D/a = 0.4$ (the limit of the linear Poisson Boltzmann equation) while the computational model results are extended to $\lambda_D/a = 0.6$. The computational results reinforce the trends seen in Figure 2.5 and show that the trend continues for λ_D/a above 0.4. For ionic solutes, the effect of valence charge is generalized through the non-dimensional valence parameter, *Z*, and the cases of $Z = 7.0$ to -7.0 correspond to ions of valence charge, z = -2 to +2, with $\zeta_o = \sigma a/\varepsilon$ = -90 mV as in Figure 2.5.

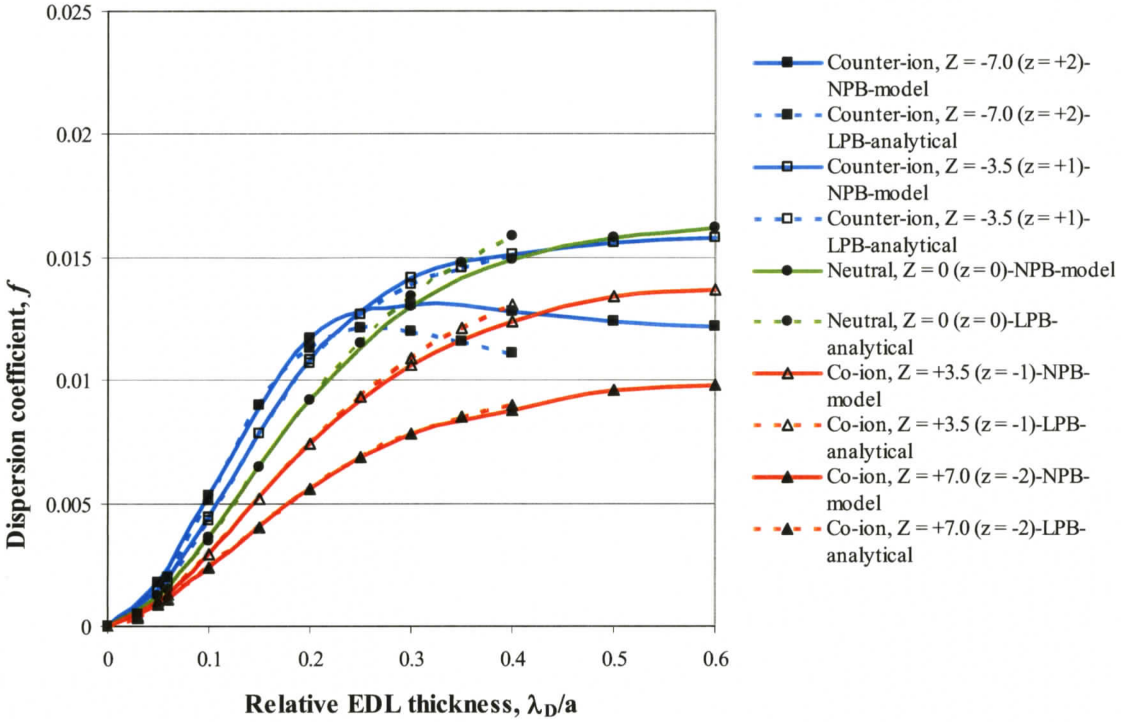

Figure 2.8 Numerical modeling and analytical solution results for electrokinetically driven flow at late times. Dispersion coefficient *f* resulting from electrokinetically driven flow is plotted versus relative EDL thickness for counter-ions, co-ions and neutral solutes comparing the computational model using the nonlinear Poisson Boltzmann (NPB) equation with the analytical model using the linear Poisson Boltzmann (LPB) equation. The analytical results stop at $\lambda_D/a =$ 0.4 (the limit of the linear Poisson Boltzmann equation) while the computational model results are extended to $\lambda_D/a =$ 0.6. The computational results reinforce the trends seen in Figure 2.6 and show that the trend continues for λ_D/a above 0.4. For ionic solutes, the effect of valence charge is generalized through the non-dimensional valence parameter, *Z*, and the cases of $Z =$ 7.0 to -7.0 correspond to ions of valence charge, $z =$ -2 to +2, with $\zeta_o = \sigma a / \varepsilon =$ -90 mV as in Figure 2.5.

2.5 Summary

This chapter presents ionic dispersion phenomena in nanofluidics. In the presence of a significant EDL, characteristic of nanoscale channels, the dispersion of ionic solutes is found to vary substantially from well-established theory on neutral solute transport. Combining relevant electrokinetic theory and the essential elements of classical Taylor dispersion work, the presented analytical solution provides a dispersion coefficient for circular cross-section channels as a function of a valance parameter, the relative EDL thickness, and the form of the velocity profile. Results indicate that in both pressure- and electrokinetically driven flows, ionic dispersion phenomena result from the combination of two unique effects. The first, charge-shear coupling dispersive effect, is a product of cross-stream ionic segregation and differential shear rates due to radially-varying velocity gradients. This effect tends to increase dispersion of counter-ions and decrease dispersion of co-ions. The second, electromigration dispersion-limiting effect, results from the restriction on radial diffusion imposed by electrostatic forces. This effect tends to decrease dispersion of all ions, and particularly of counter-ions, relative to neutral solutes. These two effects act in combination, and the result is that the dispersion of ionic species in nanoscale channels is markedly charge dependent, and substantially deviates from that of neutral solutes in the same flow. In general, co-ion dispersion is overestimated by previous theory based on neutral solutes, whereas counter-ion dispersion is underestimated at moderate, and overestimated at high relative EDL thicknesses. An independent computational model was implemented to cross-validate the analytical solution, quantify the effect of the Debye-Hückel approximation (linearization of the Poisson-Boltzmann equation), and extend the results to higher relative EDL thicknesses. Computational results using the nonlinear Poisson-Boltzmann equation supported those of the analytical solution in the suggested range of applicability, $0.05 \le \lambda_D / a \le 0.4$. Combined, these results can inform the further development of nanostructured separation technologies with the aim of minimizing dispersion. The dependencies of ionic dispersion on valence charge and EDL thickness established here may also be strategically exploited to inform separation processes, or to constitute a new separation mechanism inherent to the nanoscale.

The second half of this thesis contains an experimental study involving species transport detection in nanohole array sensors embedded into microfluidic chips with rectangular cross-section channels. Although the focus of this later half is different from the first, the unique dispersion phenomena identified here are applicable to rectangular channels. The cylindrical geometry considered here was convenient for formulating an analytical solution, and is applicable to nanoscale capillaries that are widely available.

Chapter 3

NANOSTRUCTURE BASED DETECTION ON-CHIP

In this chapter, an integrated microfluidic device with multiple embedded nanohole arrays of different periodicity is developed and demonstrated as a surface plasmon resonance sensor for on-chip chemical detection by measuring bulk changes in concentration. The device is applied experimentally to measure cross-stream concentration gradients and monitor surface protein binding events.

3.1 Background

3.1.1 Background-Surface Plasmon Resonance Based Sensors

Surface plasmons are surface bound electromagnetic waves that can be excited in sub-wavelength metallic structures such as arrays of nanoholes [Barnes et al. (2003)]. Such nanoscale structures are also common in natural systems [Vukusic and Sambles (2003)]. Incident light is scattered by the array producing evanescent waves that tunnel through the nanoholes. The evanescent waves have small but finite amplitude on the far side of the array where the waves are again scattered. The interference of the evanescent waves produces light that propagates away from the array. Surface plasmons enhance the fields associated with the evanescent waves, resulting in increased transmittance [Barnes et al. (2003)]. When the metal film is thin enough, the tunneling of the evanescent waves through nanoholes may become resonant because the surface plasmon modes overlap and interact through the holes [Barnes et al. (2003)]. Enhanced transmission of light through arrays of nanoholes in optically thick metallic films has been observed to be much higher than expected [Barnes et al. (2003), Gordon et al. (2004)]. The transmission spectra of the nanohole arrays show resonance peaks that can be adjusted with the periodicity and symmetry of the arrays [Barnes et al. (2003), Gordon et al. (2004)]. The ability to pattern nanoscale metal structures presents an opportunity to tailor surface plasmon response to specific applications. In addition, the structure-based response would be highly repeatable, an advantage with respect to mass production. The resonance is also a function of the medium particularly close to the surface and thus has applications as sensors, more specifically as surface sensors.

Some applications for surface plasmon based devices include photonic devices [Barnes et al. (2003)], and biological and chemical sensors [Brolo et al. (2004a), Brolo et al. (2004b), Liu et al. (2004)]. Surface plasmon based sensors are available commercially and used in biomedical and biochemical research for monitoring of surface binding events [Nice and Catimel (1999)], biomedical analysis [Haes et al. (2004)], nucleic acid diagnostics [Storhoff et al. (2004)], and detection of biohazardous materials and organisms [Zhang et al. (2005)]. Brolo et al. (2004a) demonstrate the use of a square periodic array of sub-wavelength holes on gold film as a SPR sensor operating in transmission mode for the adsorption of biomolecules. The mechanism exploited there is a change in local refractive index at the gold-liquid interface which results in a red-shifted transmission spectrum. Transmission geometry allows for a simpler collinear optical arrangement and provides a smaller probing area than the typical Kretschmann configuration in commercial devices [Brolo (2004a)]. The size of the nanohole arrays (a few micrometers) and the transmission geometry of the sensor allow for miniaturization and integration into microfluidic architectures [Brolo et al. (2004a)]. Liu et al. (2004)

demonstrated that nanocavity arrays can be integrated into a simple microfluidic architecture for use as an optical biosensor that takes advantage of enhanced fluorescence based on SPR in the nanostructure. Nanohole arrays have also been demonstrated for enhanced fluorescence detection for biosensing [Brolo et al. (2005)] and for enhanced Raman spectroscopy [Brolo et al. (2004b)].

Through this work, a nanohole array based SPR sensor integrated into a microfluidic chip is built and demonstrated experimentally for chemical detection. The device takes advantage of the following characteristics: the relatively small footprint (20 μm x 20 μm) of nanohole arrays; the ability to vary optical response via array periodicity; and operation in transmission mode which simplifies optical infrastructure required. The sensor is applied to detect changes in refractive index in sugar solutions of varying concentration, to measure cross-stream concentration gradients, and to monitor surface protein binding events.

This work was done in collaboration with research groups in the Electrical Engineering and Chemistry departments at the University of Victoria, formally through the British Columbia Research in Nano Optics initiative. The collaborating electrical engineering group is lead by R. Gordon, and participating group members include Kiran Kumar and Victoria de Lange. The collaborating chemistry group is lead by A. Brolo and includes Erin Arctander. The nanohole arrays were provided by the Electrical Engineering group. A spectrometer for taking measurements, a refractometer, and materials needed for protein binding were provided by the Chemistry group. Members from both collaborating groups assisted in performing the experiments. The main focus of this chapter is the integration of the nanohole array SPR sensor into a microfluidic device and subsequent experimental measurements completed in the Microfluidics Lab.

3.1.2 Background – Microfluidic Structure Fabrication

Soft lithography, particularly with poly(dimethylsiloxane) (PDMS), is a popular technique for fabrication of microfluidic devices [McDonald et al. (2000), Duffy et al. (1998)]. This method can reproduce features on the order of micrometers, it eliminates the need for a clean room, and it is inexpensive [McDonald et al. (2000), Duffy et al. (1998)]. Soft lithography is a much less time consuming alternative to etching in silicon; the concept-to-prototype turnaround time is less than 24 hours [McDonald et al. (2000), Duffy et al. (1998)]. The physical and chemical properties of PDMS, such as durability, chemical inertness, stability, and optical transparency, make it well suited to molding microstructures [de Mello (2002)]. PDMS also facilitates integration and embedding of multiple components on a microfluidic chip.

The soft-lithography fabrication procedure consists of four main steps shown in Figure 3.1. First, a photomask is created. A CAD program such as AutoCAD is used to design the desired microfluidic structure which is then printed on a transparency using a high resolution printer. The transparency serves as a photomask during UV exposure where light is only transmitted through clear areas. Photoresist, a photosensitive polymer, is spin-coated uniformly onto a durable substrate such as a glass microscope slide or a silicon wafer. The thickness of the photoresist determines the height of the microfluidic structure that will later result [McKechnie (2006)]. In this work, the thickness was 50 μm. The photomask is placed over the photoresist and it is exposed to collimated UV light which cures the photoresist. This is followed by a post-exposure bake to harden the photoresist.

The second stage of the process, following the post-exposure bake, is to immerse the photoresist in developer to dissolve any parts that were not exposed to UV light. The elevated photoresist pattern corresponding to the transparent areas of the photomask design remains on the substrate and is referred to as a master.

Thirdly, the microchannel structure is created by curing liquid PDMS over the master. A negative imprint of the master pattern is produced in the PDMS. Attainable feature sizes using this method were as small as 20 μm which is adequate for creating channel structures with a width up to 200 μm.

The fourth and final step is to create inlet/outlet holes in the channel structure and align it and seal it to a substrate. In this work, the substrate included the nanohole array structures. With PDMS, reversible sealing is possible by conformal contact between surfaces. The elastic nature of PDMS allows it to conform to imperfections in the planar surface through van der Waals forces [Ng et al. (2002)]. Reversible sealing supports low pressure flows up to 5 psi [McDonald et al. (2000)] and allows resealing without any damage to PDMS or the surface it is sealed to. This is suitable for applications where flow structures can be disassembled, easily cleaned for re-use, and base substrates or other components reused. Reversible sealing was required here because the financial and time investments in the nanohole array substrate were high.

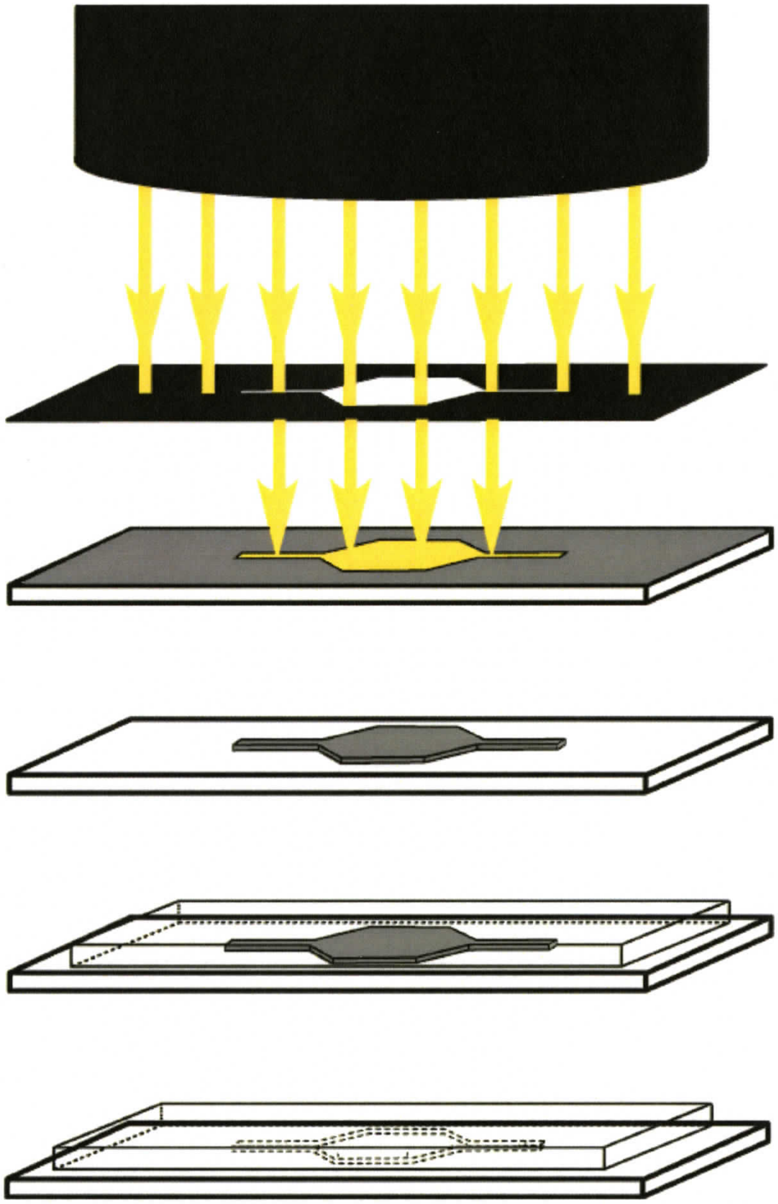

Step 1:
Selective exposure of photoresist (SU-8) using collimated UV light passed through a patterned transparency

Step 2:
Dissolving of unexposed photoresist leaves the positive template of the pattern on a substrate

Step 3:
Vacuum curing of PDMS polymer over positive template

Step 4:
Removal of master leaves negative channel structure embedded in PDMS

Figure 3.1 Schematic and description of the soft-lithography microfabrication method.

3.2 Experimental

3.2.1 Fabrication of Nanohole Arrays

Several nanohole array substrates were employed at different stages as this work developed. Images of a typical nanohole array were provided in Figure 1.5. Discussed here is the fabrication and application of the final substrate employed. The nanohole arrays were fabricated by Kiran Kumar of the collaborating electrical engineering group by focused ion beam milling on a 100 nm optically thick commercially coated gold film on a glass substrate (Evaporated Metal Films, Ithaca, NY). The arrays were fabricated and imaged using a FEI 235 dual beam gallium ion beam and field emission scanning electron microscope at Simon Fraser University. The ion beam was set to 30keV with a milling rate of 1.6 nm/μs and the beam current was 300 nA. The nanoholes were approximately 150 nm in diameter and were made to form two rows of six arrays each. A map of the nanohole arrays is shown in Figure 3.2. One row contained arrays of periodicity (center-to-center spacing between holes) 350, 450, 550, 650, 750, 850 nm and the second row contained 6 arrays of 650 nm periodicity. The six arrays of varying periodicity were used to determine which periodicity was best suited for sensing, the six arrays with 650 nm periodicity were used to measure cross-stream concentration gradients in a focusing experiment and to detect protein binding events. The arrays were approximately 20 μm x 20 μm each and thus the footprint of the set of arrays was less than 1 mm x 100 μm.

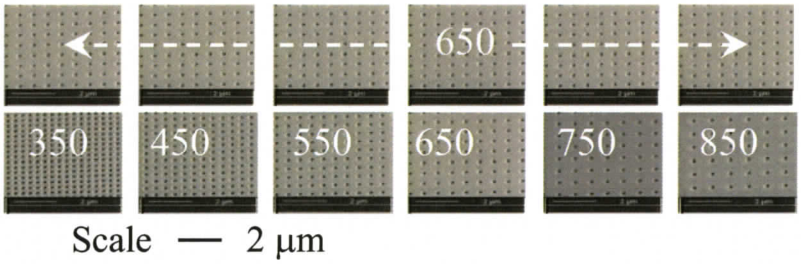

Figure 3.2 Nanohole array sensor map with periodicities indicated in nanometers. The identical upper row arrays are for cross-stream concentration gradient measurements. Only portions of each array are shown.

3.2.2 Fabrication of the Microfluidic Chip

The microfluidic channel structures were made using soft-lithography techniques [Duffy et al. (1998), McDonald et al. (2000)], outlined in Figure 3.1. Photomasks of each channel structure were created in AutoCAD 2006 and printed on transparencies using high resolution printing (Island Graphics, Victoria, BC). The photoresist SU-8 50 (MicroChem, Newton, MA) was spin-coated on a silicon wafer (Silicon Quest International, Santa Clara, CA) ramping to 500 rpm in 5 sec, then dwelling for 8 sec, then ramping to 2000 rpm in 5 sec and spinning for 25 sec, resulting in a uniform thickness of 50 μm. Silicon wafers were used because they have a clean flat surface that the photoresist readily adheres to. The coated silicon wafers were pre-baked at 65 °C for 6 min, then at 95 °C for 20 min to harden the photoresist. The photomask was positioned over the silicon wafer and it was exposed under a collimated UV light for 45 sec. This was followed by a hard bake first at 65 °C for 1 min, then at 95 °C for 5 min to promote polymerization of the photoresist. The exposed silicon wafer was then immersed in SU-8 developer (MicroChem, Newton, MA) until all the unexposed photoresist was removed. To remove excess developer isopropyl alcohol was used to rinse the wafer. The wafer had a somewhat streaky surface and was cleaned quickly in acetone and allowed to dry. The master template was thus created.

The microchannels were created by curing PDMS on the masters. Approximately 30 g of PDMS base and curing agent (Sylgard 184 Elastomer, Dow Corning Canada, Mississauga, ON) were mixed in a 10:1 by weight ratio, stirred and poured over the master in a round Petri dish. The 30 g of PDMS was used to create a slab of PDMS approximately 4 mm thick. Thick PDMS was used so that hoses could be inserted into it and held in place by friction fit and so that the PDMS was stiff enough that the channel structures would not collapse under suction. The PDMS was then degassed for 45 min in a -27 in-Hg vacuum and cured at 95 °C for 2 hours on a hotplate. The PDMS with channels was cut from the master and assembled over the gold-on-glass substrate with nanohole arrays to form the microfluidic device.

3.2.3 Microfluidic Chip Configurations

Two configurations of microchannel structure were designed to flow liquids over the nanohole array SPR sensors. A schematic of channel structure positioning over nanohole arrays is shown in Figure 3.3. The configuration shown in Figure 3.3a has two inlets and one outlet for cross-stream concentration measurements during colaminar flow. This test involves a gradient in sample solution, analyzed at spatially separated sensors with identical periodicity. The configuration shown in Figure 3.3b is a single-inlet single-outlet channel to be used for measuring the transmission spectra in the row of arrays with varying periodicity. This test involves a single sample, analyzed with multiple sensors, differentiated by rectangular array periodicity. Both channel structures fit within a 1" x 1" boundary corresponding to the size of the commercial gold-on-glass substrate. The arrays were offset from the center of the substrate to facilitate tubing (world-to-chip interface) without interfering with the microscope objective. The inverted microscope, now available in the lab, avoids this competition between optical and fluidic infrastructure. Each PDMS structure was aligned over top of the gold surface with nanohole arrays and was capped with a clear plexiglass cover plate where a clamping force was applied. Openings in the cover plate allowed inlet/outlet hoses to be introduced into the PDMS layer. A circular viewing area was cut in the plexiglass and positioned over the nanohole arrays so the plexiglass would not interfere with light transmission measurements through the nanohole arrays.

Configuration a: This configuration is shown in Figure 3.3a. It has two inlets, one outlet, and a 1 mm x 1 mm viewing window for the arrays. It is used for gradient-based experiments over the row of arrays with a 650 nm periodicity, and for monitoring protein binding events.

Configuration b: This configuration is shown in Figure 3.3b. It is a channel with one inlet, one outlet, and a 6 mm x 1 mm viewing window for the nanohole arrays. It is used to measure the transmission spectra in the row of arrays with periodicity from 350 nm to 850 nm using sugar solutions of varying refractive index.

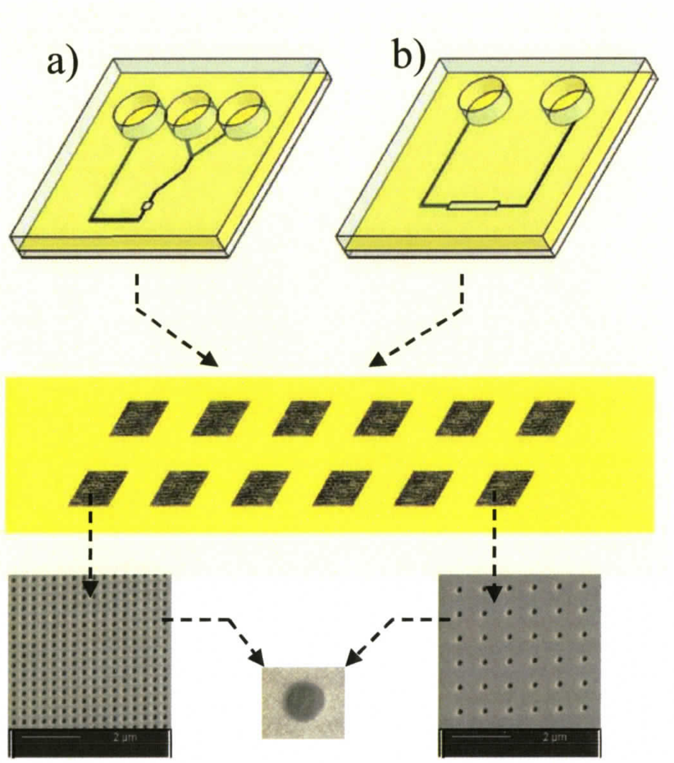

Figure 3.3 Schematic of the microfluidic chip with embedded nanohole arrays. Two microfluidic configurations are shown with the sensing element pattern illustrated below with sample SEM images of the nanoholes. Each array is 20 µm x 20 µm. a) The microchannel configuration shown on the left enables measurements (with fixed periodicity) across a concentration gradient (referred to as configuration a in the text). b) The chip configuration shown on the right enables single solution (multisensor) tests (referred to as configuration b in the text).

3.2.4 Device Assembly

The microfluidic device with embedded nanohole arrays involved several layers which needed to be assembled into the final chip shown in Figure 3.4. The components of the device included a 3" by 1" standard glass microscope slide, a 1" by 1" commercially coated gold-on-glass substrate with nanohole arrays, the PDMS microchannel structure, a 1/16" thick plexiglass cover plate with openings for hoses and for viewing nanohole arrays, double sided tape, and two clamps. The gold-on-glass substrate was fixed to the microscope slide with small ¼" X ¼" pieces of double sided tape to facilitate alignment of the chip components and integration of the device with the microscope stage.

Separately, the viewing area and tube openings in the plexiglass coverplate and PDMS structure were aligned and the PDMS reversibly bonded to the plexiglass. The PDMS channel structure was then plasma treated for 20 s which caused the surface to become hydrophilic [Duffy et al. (1998)], and facilitated filling of the device. Once the PDMS with coverplate was removed from the plasma treater, distilled water was put on the PDMS to retain hydrophilicity, otherwise, in air, the PDMS will revert to its native hydrophobic state [Duffy et al. (1998)]. The hydrophilic channel structure was then aligned with the nanohole arrays over the gold-on-glass substrate and a clamping force was applied. Hoses were inserted into the PDMS with a friction fit and the desired liquids flowed through the channel structure using a syringe pump. The total assembly was approximately 7.5 mm thick. It is noteworthy that the plasma treatment that renders the PDMS surface hydrophobic also enables irreversible bonding to glass and other materials, however not to gold. Thus with a gold-coated substrate it was possible to have a hydrophilic channel structure as well as a reversible channel structure-substrate bond. The assembly described above allows the chip to be taken apart easily for cleaning, and to be reassembled with different PDMS channel structures as desired. In this work, the same multi-array gold-on-glass substrate was employed with over 10 microfluidic structures. The assembled prototype chip is shown in Figure 3.4.

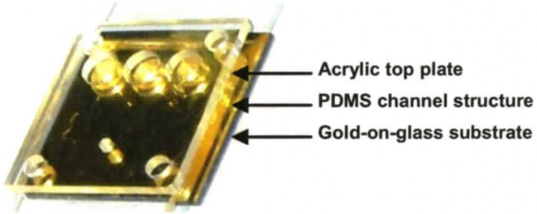

Figure 3.4 Prototype chip. To ensure sealing, the reversible bond at the acrylic-PDMS and PDMS-gold interfaces was reinforced with clamping pressure. Tube connections were made by friction fit into the pre-punched PDMS layer.

3.2.5 Chemicals

As a proof of concept experiment, the transmission through the nanohole arrays was measured when solutions of varying refractive index flowed over the arrays. Sugar solutions with varying concentrations of sucrose produced sufficient change in refractive index for the red shift in the transmission spectra to be noticeable, i.e. 3 nm. The change in refractive index is proportional to the SPR wavelength shift in the transmission spectra for each array. Solutions of refractive index varying from 1.332 (pure water) to 1.358 (concentrated sugar solution) were used. For example, a 1M sugar solution has a refractive index of 1.352 measured on a refractometer. Sucrose has the chemical formula $C_6H_{12}O_6$ and molecular weight 180 g mol^{-1}. To make a 1M sugar solution, for example, 0.9 g or 0.005 moles was mixed into 5 mL of pure water.

Other materials such as sodium chloride solution also have a change in refractive index with varying concentration in water but the corresponding shift in SPR is too small to be seen when measured with a halogen light source. Sucrose, a large molecule, produces a more noticeable change in refractive index with change in concentration. Solutions such as acetone (refractive index = 1.342) and ethanol (refractive index = 1.361) would also produce a noticeable shift in SPR but were not used because they have undesirable effects on PDMS, such as swelling [Lee et al. (2003)].

A sugar solution with a refractive index of 1.359 was used to measure cross-stream concentration gradients over the nanohole arrays. For comparison with the concentration gradient measurements obtained with the arrays, images of gradient generation with colored dye were obtained. The colored dye used here was Napthol blue black, mixed at 1% by weight in water. For example, a 1% by weight solution of blue dye is made by mixing 0.1 g of dye in powder form into 10 mL of distilled water.

[Note: Details of the chemicals employed in the on-chip assembly of the cysteamine-biotin-streptavidin system are provided with the results, Section 3.3.4.]

3.2.6 Fluid Delivery and Optical Setup

A syringe pump was used to pull liquids through the microstructure over the nanohole arrays by applying a constant flow rate and resultant suction pressure at the outlet reservoir. Operation in vacuum mode promotes sealing of the channel structure which is an advantage when a reversible seal is employed. Tygon tubing with an internal diameter of 3/32" was friction fit into the PDMS outlet hole and attached to a 10 mL syringe. Suction flow rate was controlled by the syringe pump. Inlet reservoirs were filled manually with a pipette.

Transmission spectra through the nanohole arrays were measured with a fiber optic cable connected to a spectrometer (S2000 Ocean Optics Inc., Dunedin, FL) and OOIBase32 software (Version 2.0.6.2, Ocean Optics Inc., Dunedin, FL), as shown schematically in Figure 3.5. The software provided the light transmission intensity in counts for wavelengths between 370 nm and 1050 nm. A halogen light source was used to shine light through the nanohole arrays on a microscope using a 50x objective with a long working distance and a light intensity of 6 V. The 50x objective was used so that only one array was in the field of view when a measurement was taken, preventing interference from neighboring arrays. An objective with a long working distance, here 8.1mm, was used so that the assembled chip (7.5 mm thick) would fit under the objective.

Inlets and outlets for tubing were designed to be on the same side of the chip (see Figure 3.3) so the tubing would not interfere with the microscope objective.

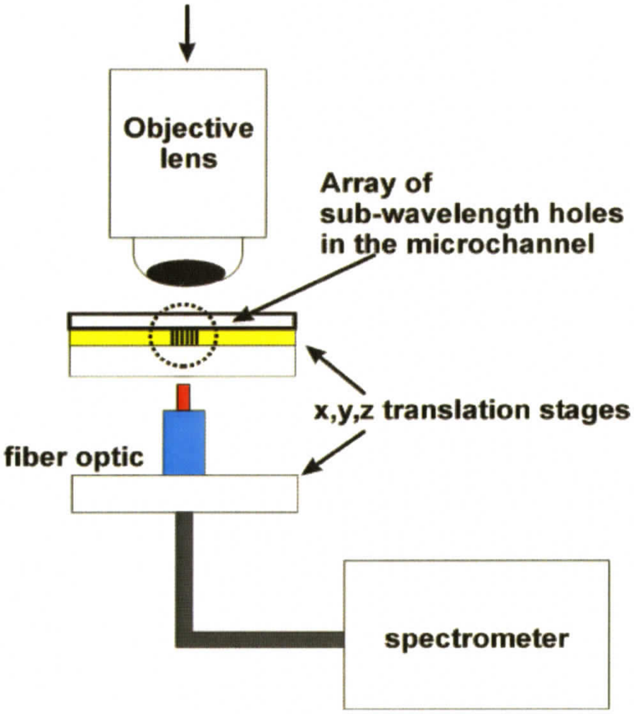

Figure 3.5 Experimental setup for transmission spectrum measurements through nanohole arrays. A broadband halogen light source was employed.

3.3 Results

3.3.1 Fluid Flow over Nanohole Arrays

As discussed in Chapters 1 and 2, there are two general mechanisms with which to drive and control fluid flow in microstructures. These are pressure driven and electrokinetically driven (or electroosmotic) flow. The high degree of control and relative simplicity of electroosmotic flow made it the preferred choice. However, as shown through numerical simulations (employing the same numerical model and computational platform as in Chapter 2), the requirement of a noble metal (gold in this case) at the interface of the structure and solution complicates electroosmotic flow. Specifically, the conductive gold layer effectively prevents the formation of an axial electric field over the nanohole arrays. One strategy to avoid this is to have the gold conductive layer only where needed and utilize electroosmotic pumping elsewhere as shown in Figure 3.6. This was effectively an electroosmotic pumping scheme as described elsewhere [Herr et al. (2000)]. Pressure driven flow was induced above the nanohole arrays by electrokinetic driving forces in the rest of the network. Although this was an effective strategy, it was not the most practical due to electrolysis and fabrication issues. For the experiments described here pressure driven flow was used throughout.

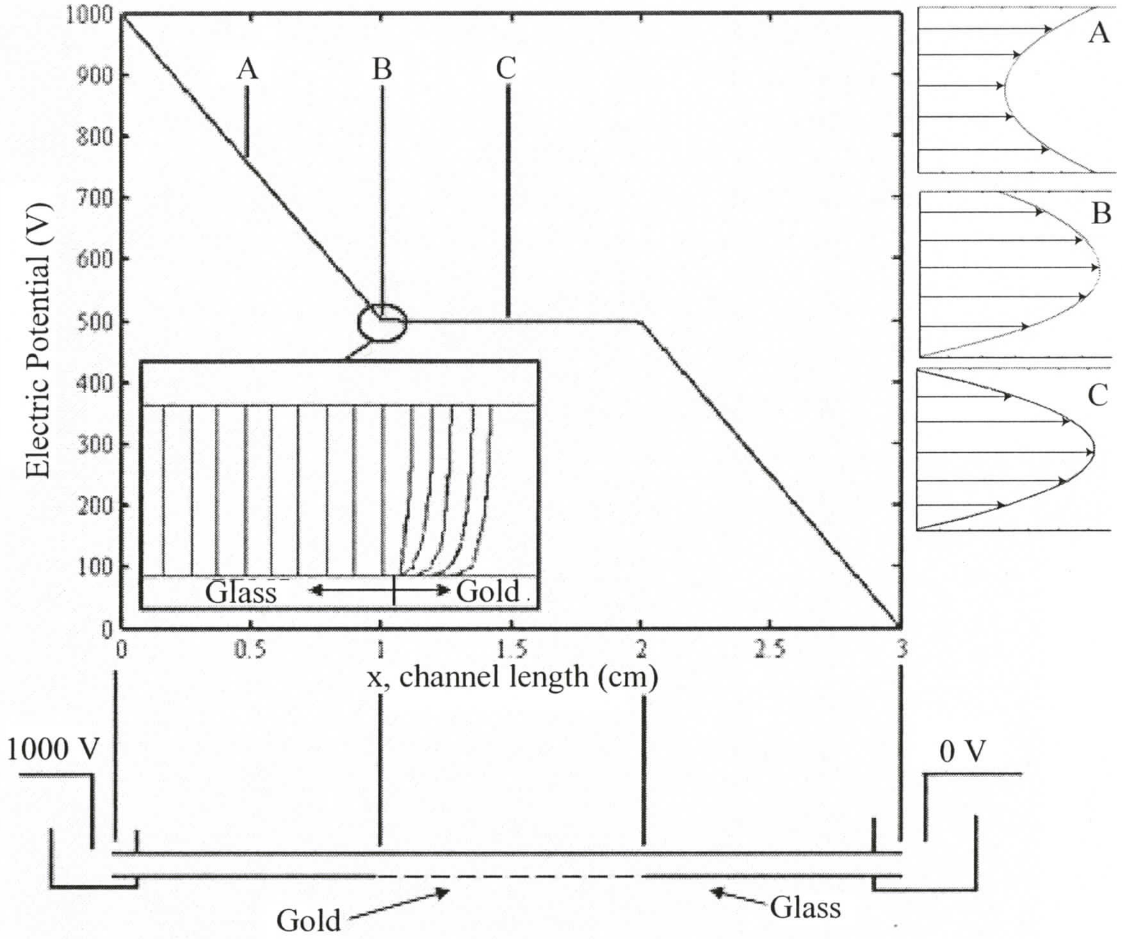

Figure 3.6 Electrical potential variation along a microchannel with electroosmotic flow where 1000 V is applied at the inlet and the outlet is grounded, and the corresponding gold patterning. The inset plot shows an expanded 2-D view of iso-potential lines near point B. The points labeled A, B and C correspond to velocity profiles on the right. Location A is the electroosmotic velocity profile 0.5 cm along the channel. Location B is the transition velocity profile 1.005 cm along the channel. Location C is the pressure-driven velocity profile 1.5 cm along the channel over gold.

3.3.2 Transport within Nanohole Arrays

The experiments discussed in this chapter involve flowing liquids through a microfluidic channel structure over the nanohole array sensors. It is therefore appropriate to understand and characterize relevant transport mechanisms between the nanoholes and the microfluidic stream. This transport is also of general interest in the context of nanohole array sensors as it presents a fundamental limit with respect to the temporal sampling rate achievable with this technology.

Numerical simulations with a detailed 2-D sub-domain were used to investigate the time dependant transport phenomena in the nanohole arrays; it was implemented in COMSOL software (COMSOL MULTIPHYSICS, COMSOL Inc., Stockholm Sweden). The following nanohole dimensions were considered in the model: a diameter of 200 nm and a depth of 500 nm. The computational domain included ten nanoholes with a spacing of 600 nm between them. The situation modeled is that of a solution replacement over the nanohole arrays. The interface between the solutions is sharp entering the computational domain (i.e. no prior diffusion). Although this boundary condition facilitates the nanohole-to-free stream transport analysis and the determination of the time lag associated with the sensor, it would be difficult to apply in practice. In application, the minimum response time is both a function of the upstream fluidic switching and nanohole-to-free stream transport. The diffusion equation (equation 1.16) was solved, using a molecular diffusion coefficient with a constant value of $5\text{x}10^{-10}$ m^2 s^{-1} [Bird et al. (1960)]. Velocity values were obtained from a liquid flow simulation using the incompressible Navier Stokes equations 1.1 and 1.2 with a liquid having the same properties of water at 25 °C, density was 997 kg m^{-3} and viscosity was $0.8909*10^{-3}$ Pa s

[White (1999)].The average velocity in the channel was 1.5 mm/s obtained from the Navier-Stokes equations.

Figure 3.7 shows the computational domain and during the solution replacement including both convective and diffusive transport. The inset velocity vector plot shows that there is a small circulation developed in the nanoholes, with a characteristic velocity on the order of 100 nm/s. Although this circulation facilitates some mixing of the fluid in the nanohole with that of the free stream, diffusion is the dominant transport mechanism. The relative strengths of these transport mechanisms are evident by comparing the characteristic recirculation velocity, v = 100 nm/s, to the diffusion velocity defined as $v_D = D/l = \frac{10^{-10} m^2/s}{500*10^{-9} m} = 200 \mu m/s$. Figure 3.8 shows a plot of concentration at the base of a nanohole versus time during a solution replacement. It takes 0.2 seconds for the concentration in a nanohole to reach 99.9% of that of the free stream. Considering the time typically associated with switching solutions in a microfluidic channel, the time for the solution to permeate the nanoholes is thus insignificant. In the case of larger molecules, such as biomolecules, increased permeation time can be expected to scale with the increased diffusion coefficient. The axial concentration gradients would not be as sharp as those simulated here due to axial diffusion of the concentration front prior to reaching the array. The time scale for diffusion is $\tau = l^2 / D$ [Probstein (1994)] where l is the characteristic length; here it can be taken as the nanohole depth, 500 nm. For a fluid with the same properties as water (D = 5x10^{-10} m^2 s^{-1}), the time scale for diffusion in a nanohole is τ = 0.5 ms. Both the numerical simulation and the diffusion characteristic time parameter indicate that diffusion happens rapidly in the nanohole arrays and flushing one liquid with another will not result in contamination or present a significant bottleneck with respect to the temporal resolution of the measurements.

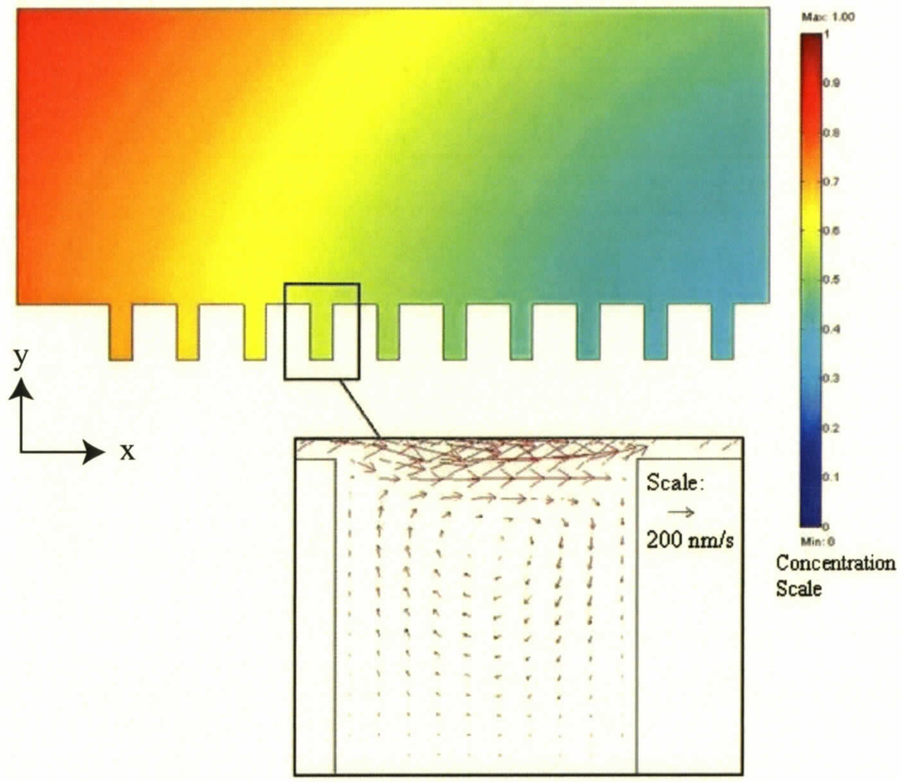

Figure 3.7 Concentration and circulation in nanoholes. The concentration in and around the nanoholes is shown during the exchange of solutions. The inset shows circulation in the nanoholes, the scale indicates an arrow length of 200 nm/s. The color scale on the right indicates the non-dimensional concentration.

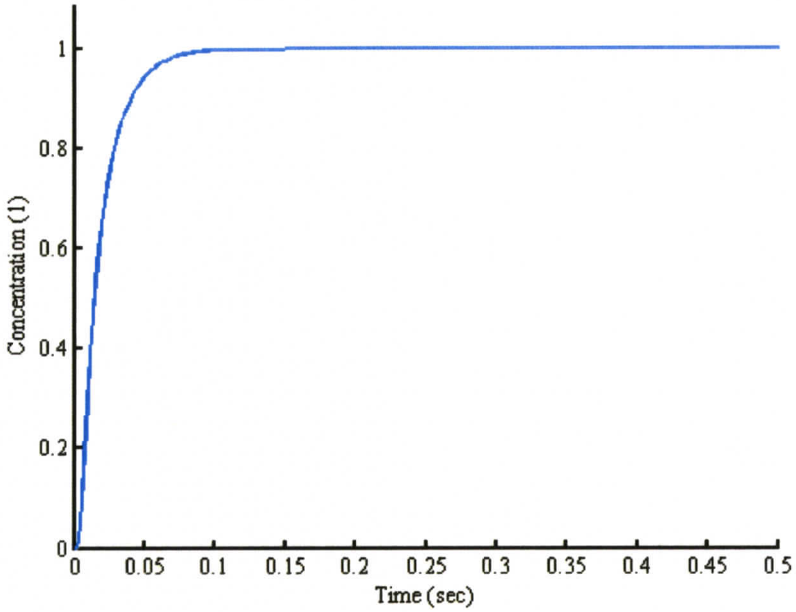

Figure 3.8 Variation in concentration over time at the base of a nanohole during a solution replacement. It takes 0.2 seconds to reach a non-dimensional concentration of 1 (to within 99.9%).

3.3.3 Sucrose and Water Based Measurements

The effect of the microfluidic chip material, PDMS, on transmission measurements through the arrays was established here. Although PDMS is reported to be optically transparent in the wavelength range of interest [de Mello (2002)], it was important to validate that the channel structure would not bias the results. Transmission measurements in water through the arrays of varying periodicity were done with and without the PDMS layer in place. Figures 3.9 and 3.10 show the transmission spectra with and without the PDMS layer, respectively. Table 3.1 compares the surface plasmon resonance peak wavelengths for each array obtained from the transmission spectrum measurements. No systematic error was detectable, only seemingly random variations on the order of 1 nm were observed. The conclusion is that a PDMS channel structure can safely be placed over the nanohole array sensors without incurring artifacts on the transmission measurements.

Array Periodicity (nm)	**Resonance Wavelength (nm)**		**Error (nm)**
	Water, no PDMS layer	**Water in PDMS channel**	
350	606.4	605.4	1.0
450	644.1	644.0	0.1
550	608.9	609.6	-0.7
650	680.2	676.4	3.8
750	no peak	no peak	-
850	no peak	no peak	-

Table 3.1 Comparison of resonance wavelength in water with and without the PDMS channel structure.

In the context of sensor applications, several aspects of the spectral responses plotted in Figure 3.9 are noteworthy. To be useful as a sensor, it would be beneficial for the arrays to exhibit sharp SPR peaks in the transmission spectrum. The first spectral peak appears at about 500 nm and is common to all the arrays, this is a strong spectral component of the halogen light source (it is broadband). The 350 nm periodicity array produces resonance with the largest intensity, however the peak is very broad with the maximum intensity occurring at around 605 nm. The 450 nm periodicity array has several peaks, the sharpest of which occurs at a wavelength of 644 nm. The multiple peaks result from small resonances that occur at the gold/glass interface, and the PDMS/liquid interface in addition to the gold/liquid interface. The 450 nm periodicity array appears to have the sharpest resonance peak at 644 nm, which makes it the most desirable for detecting shifts in the resonance wavelength. The 550 nm and 650 nm periodicity arrays show smaller resonances at wavelengths 609 nm and 676 nm respectively. The 750 nm and 850 nm periodicity arrays do not appear to have resonances in the visible range of light detected. The resonances associated with these larger periodicity arrays occur in the infrared range which is not picked up by the spectrometer.

The transmission spectrum of white light, obtained with a halogen source, was used to demonstrate the response of the device to refractive index variation at the surface where the nanohole arrays are located. In Figure 3.11 transmission spectra obtained with the device through arrays of periodicity 350 nm to 850 nm are shown for both pure water (refractive index = 1.332) and a sugar solution (refractive index = 1.352). Although each spectral pattern is a function of many variables (including array periodicity, input light spectrum etc.) a clear red-shift is observed for the 350nm to 650nm cases corresponding to an increase in index of refraction of approximately 10%. The 750nm and 850nm periodicity arrays again do not show any resonance peaks or corresponding red shift, making them unsuitable for use as chemical sensors with the experimental setup used here.

To quantify sensitivity, five sugar solutions with index of refractions varying from 1.332 (pure water) to 1.358 were prepared. Transmission spectra for each solution from the array with 450 nm periodicity exhibited clear peaks at wavelengths 606 nm, 644 nm, and 674 nm as seen in Figure 3.12. The red-shift in peak wavelength was proportional to the index of refraction of the solution. Relative peak shifts measured for each peak in the 450 nm periodicity array spectrum obtained from Figure 3.12 are plotted versus index of refraction in Figure 3.13. Error bars representative for all measurements are indicated on the 606 nm wavelength peak case. The pure water case was tested first, and used as the reference case (collapsed data at n = 1.332). Increasing the index of refraction over the total range, 0 to 2%, resulted in a significant, linear increase in relative peak wavelength from 0 to 10 nm. Lastly, the chip was flushed again with pure water corresponding to the second set of data shown at n = 1.332. Increasing the index of refraction over the total range, 0 to 2%, resulted in a significant, linear increase in relative peak wavelength from 0 to 10 nm. The demonstrated sensitivity is 333 nm/RIU (refractive index unit) in very good agreement with [Brolo et al. (2004a)]. The solution employed exhibits 7.6 M/RIU, thus the sensitivity in concentration is 43.8 nm/M. With the exception of the 750 nm and 850 nm periodicity arrays, all arrays showed similar redshift in resonance peak with change in refractive index.

Two rows of nanohole arrays were fabricated on the gold-on-glass substrate at the same time before any experiments were conducted. The array periodicity selected for cross-stream concentration gradient measurements was 650 nm. This value was the middle of the range, 350 nm to 850 nm, in the row of arrays used to determine the optimum periodicity. After experimentation it was found, however, that the 450 nm periodicity array appeared to have the best sensing characteristics. If the gradient generation experiment was to be done again, a row of 450 nm periodicity arrays would be used. It was, however, still possible to obtain results from the 650 nm periodicity arrays, which are discussed next.

The set of six arrays of the same periodicity facilitate spatial sampling across a microfluidic flow. Microfluidic gradient generation is facilitated by colaminar microfluidic streaming. Two liquids enter the microfluidic channel structure and they flow side by side with minimal mixing. As described in Chapters 1 and 2, typical flows in microchannels are laminar with low Reynolds number and the only mixing that occurs is due to diffusion. The width of the mixing region (or equivalently, the rate of mixing) of the two adjacent liquid streams can be controlled by varying the flow rate. The mixing width in the focusing chip is determined as follows [Ismagilov et al. (2000)]:

$$\Delta x_w = \left(\frac{D h_C y}{U} \right)^{1/3} \quad \text{or} \quad \Delta x_c = \left(\frac{D h_C y}{U} \right)^{1/2} \qquad (3.1)$$

where Δx is the mixing width of the two fluid streams at locations indicated by subscripts w, wall, and c, channel center, D is the diffusion coefficient, U is the average flow speed in the channel, h_C is the channel height, and y is the distance traveled along the channel. The mixing width refers to the interface between the two fluids in the focusing channel where a concentration gradient exists. The limits of the mixing region are between 95% mixed and 5% mixed. For channel configuration a (Figure 3.3a) with a width of 200 μm, channel height of 50 μm, diffusion coefficient of $5\text{x}10^{-10}$ m^2/s, and distance traveled of 7 mm, the near-wall mixing width at various flow rates were estimated. The results for flow rates of 0.001 mL/min and 0.050 mL/min are shown in Table 3.2.

Flow rate (mL/min)	**Velocity, U (m/s)**	**Mixing width, Δx_w (µm)**
0.001	0.0017	47
0.050	0.0833	13

Table 3.2 Near-wall mixing width estimates for typical flow rates.

A flow rate of 0.050 mL/min results in a mixing width corresponding to 7% of the channel width. A flow rate of 0.001 mL/min, however, corresponds to a mixing width that spans 24% of the channel. The flow rate of 0.05 mL/min is used to demonstrate detection over a sharp concentration gradient as compared to the 0.001 mL/min case.

Using channel configuration a and the set of 650 nm periodicity arrays, the device was applied to measure cross-stream concentration gradients. Colored dye solution was employed to demonstrate gradient generation in the microfluidic channel. The dye was introduced at one inlet while the other inlet provided pure water. A microscope image of the resulting flow is provided in Figure 3.14a. The six 650 nm periodicity arrays are labeled in the image. The sharp gradient apparent in the inlet flow is spaced across the expansion chamber and reformed in the outlet. The total flow rate for this case was 0.001 mL/min. The dye solution was replaced with sugar solution and resonance peak wavelengths were recorded at each cross-stream 650 nm periodicity array at different flow rates. Figure 3.14b compares the resonance wavelength at each cross-stream array when the channel contained pure water, pure sugar solution, a gradual gradient (0.001 mL/min), and a sharper gradient (0.05 mL/min). The resulting resonance wavelength profiles reflect expected cross-stream concentration behavior in each case.

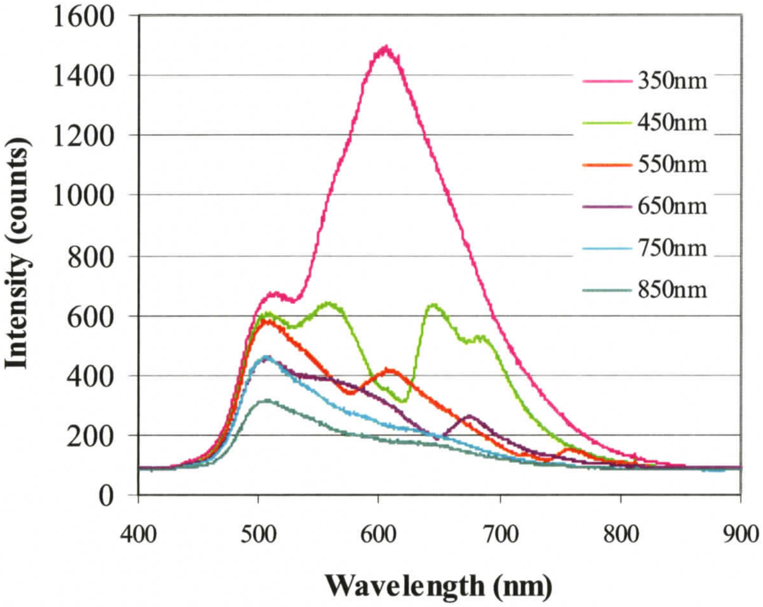

Figure 3.9 Transmission spectra for arrays of varying periodicity with water in the PDMS channel structure over the arrays. The array periodicities are indicated in nanometers in the legend.

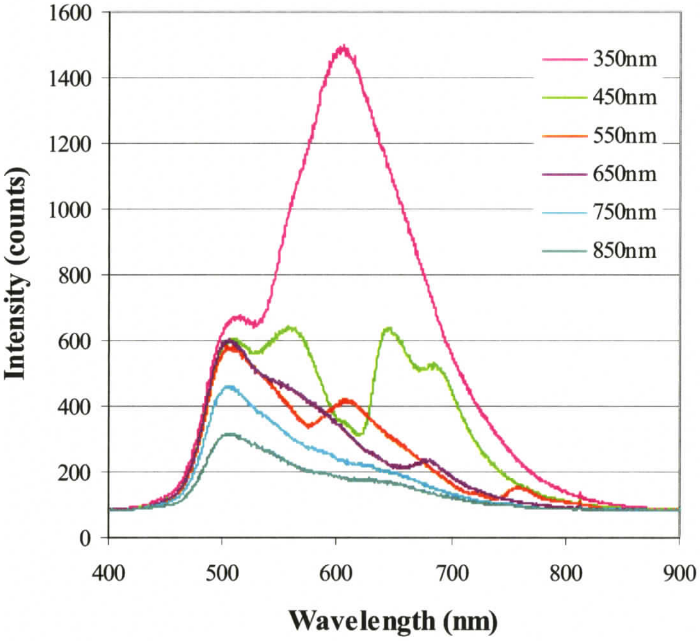

Figure 3.10 Transmission spectra for arrays of varying periodicity in water with no PDMS channel structure over the arrays. A droplet of water was placed on the bare gold surface over the arrays. The array periodicities are indicated in nanometers in the legend.

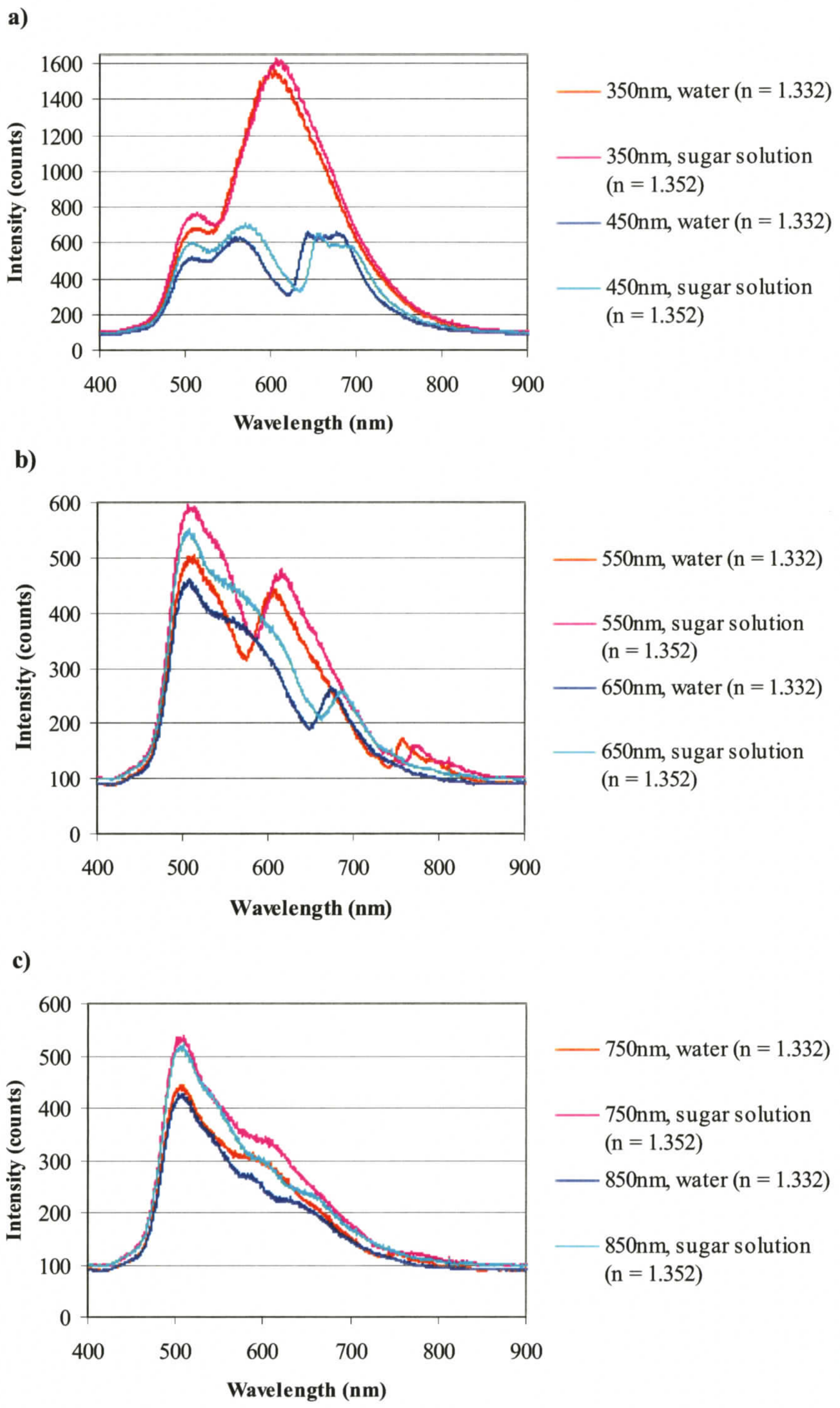

Figure 3.11 Comparison of transmission spectra for pure water (refractive index, n = 1.332) and sugar solution (refractive index, n = 1.352) in channel over the arrays. a) Transmission spectra for arrays of periodicity 350nm and 450 nm. b) Transmission spectra for arrays of periodicity 550nm and 650 nm. c) Transmission spectra for arrays of periodicity 750nm and 850 nm.

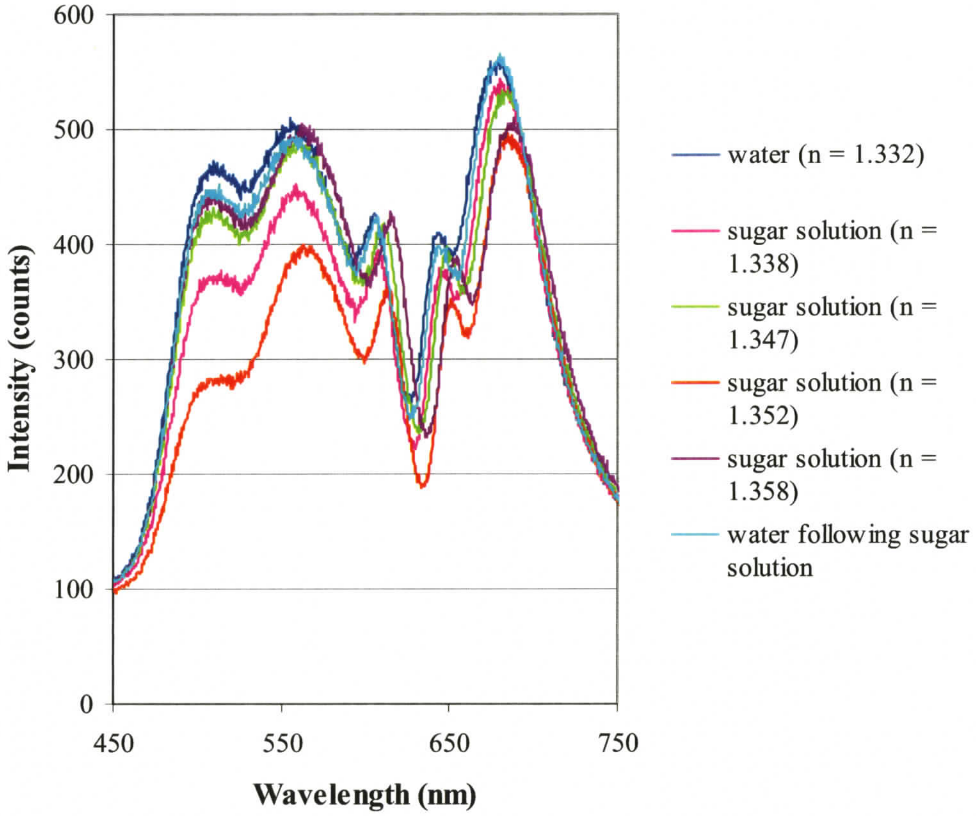

Figure 3.12 Transmission spectra in the array with periodicity 450nm for pure water (refractive index, n = 1.332), sugar solutions with refractive index varying from 1.338 to 1.358, and again for water after the sugar solution has been flushed out. The red shift in resonance peak wavelengths can be seen. The refractive index is indicated in brackets in the legend.

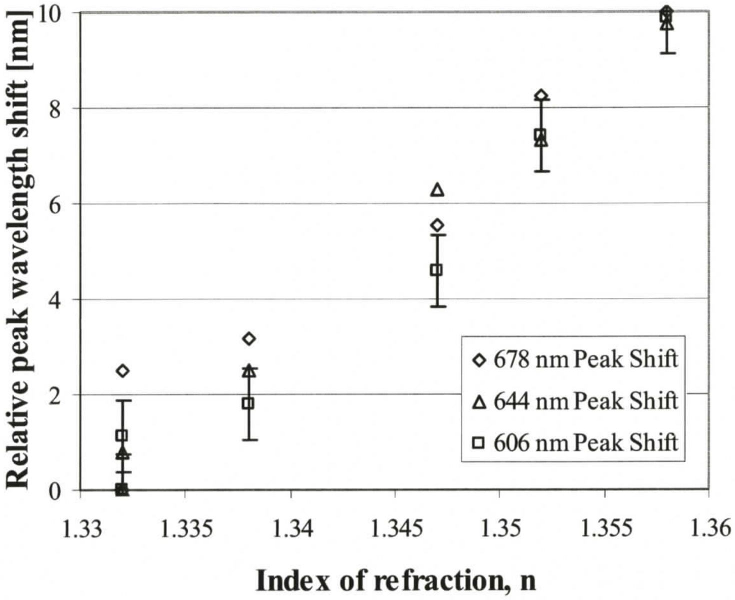

Figure 3.13 The relative red-shift in peak wavelength for three spectrum peaks (at wavelengths 606 nm, 644 nm, and 674 nm) exhibited by the array with a 450 nm periodicity as a function of refractive index of the surrounding medium. The two sets of data for the pure water case (n = 1.332) correspond to the first and last measurements. Estimated error for all measurements is indicated for the 606 nm wavelength case.

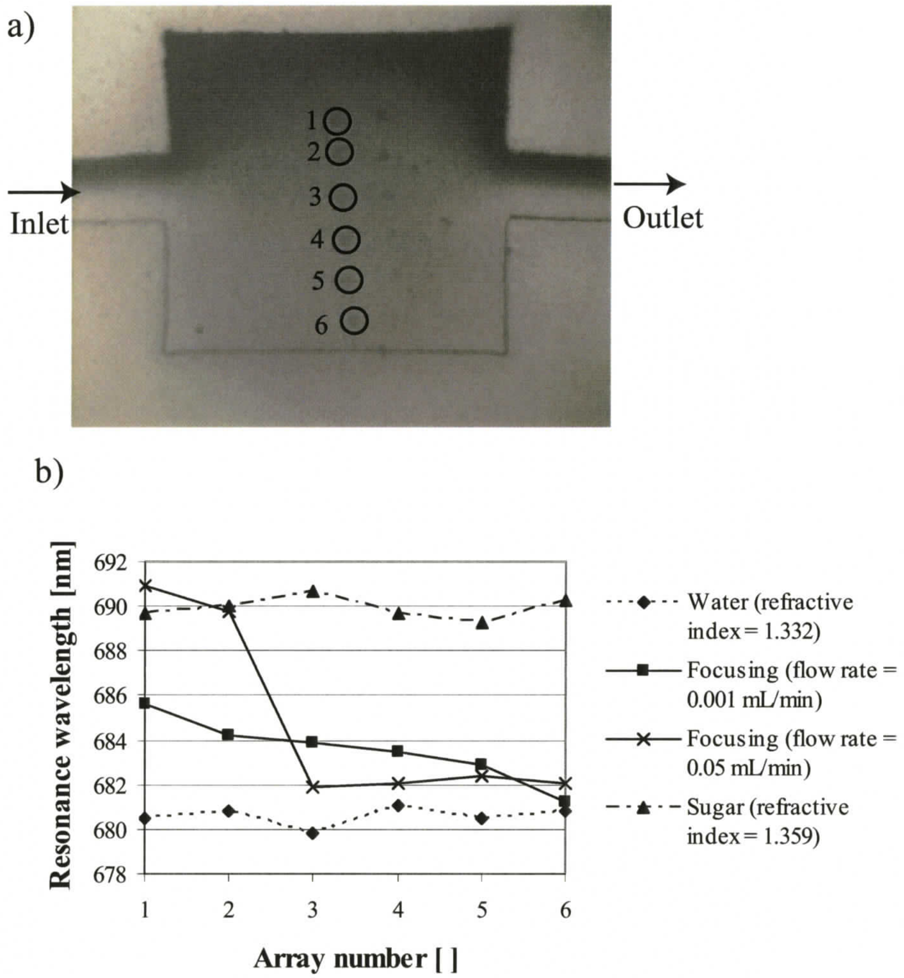

Figure 3.14 Focusing over nanohole arrays. (a) A 5x magnification image using colored dye instead of sugar solution to demonstrate focusing visually at a flow rate of 0.001 mL/min. The array periodicity is 650nm. (b) A plot of resonance wavelength for each of the six arrays shows focusing with a concentration gradient for two different flow rates: 0.001 mL/min and 0.05 mL/min. Array numbers correspond to those in (a).

3.3.4 Surface Binding Measurements

The surface-specific nature of nanohole array based sensing was exploited to monitor specific surface binding events in the cysteamine-biotin-streptavidin system on the nanohole array substrate. The cysteamine-biotin-streptavidin model system was chosen because it is readily available, the biotin-streptavidin bond is generally quite strong, and the biochemistry is well established [Neuert et al. (2005)]. The protein bonding to the gold surface involves a three step procedure. A schematic of the final protein binding is shown in Figure 3.15. First a solution of cysteamine (Sigma-Aldrich, St Louis, MO, Cat # M9768) with a molecular mass of 65 g/mole was prepared by mixing 0.002g of cysteamine in 5mL of water. To clean the gold-on-glass chip, it was rinsed in acetone and then in methanol. It was then placed in an ultrasonic bath in methanol for 3 minutes, plasma cleaned for 15 minutes, and then soaked in the cysteamine solution for 72 hours. During this soak, a cysteamine monolayer assembled on the gold surface. On removal from the cysteamine, the gold was cleaned in ethanol, then in distilled water. The microfluidic device was then assembled, the PDMS channel structure and cover plate were clamped over top the gold and a PBS buffer (pH 7) was flowed through the channel over the nanohole arrays. For consistency, the spectrum measurements were always taken when there was PBS buffer in the channel. The transmission spectrum in the 6 arrays of the 650 nm periodicity row was measured with the spectrometer in the experimental setup shown in Figure 3.5.

Secondly, a solution of biotin linker (EZ-Link® NHS-LC-LC-Biotin, Pierce, Rockford, IL; Cat # 21343) was prepared by dissolving 12 mg of biotin into 2 mL of Dimethyl Sulfoxide (DMSO). This solution was introduced in the channel structure over the nanohole arrays and the biotin molecules bonded to the cysteamine monolayer. The biotin flowed in the channel for 45 min at a rate of 0.02 mL/min during which time it attached to the cysteamine monolayer. Again, the transmission spectrum of each 650 nm periodicity array was measured with PBS buffer replacing the biotin solution.

The third and final step in protein binding was to mix a solution containing the streptavidin protein (Sigma-Aldrich, St Louis, MO, Cat # S4762). Since the amount of protein required was so small (less than 0.1 mg) an amount exceeding the required concentration was used. A quantity of streptavidin was measured out until it produced a noticeable change on the balance reading. The mass of streptavidin used was estimated to be between 0.5 mg and 1 mg. The streptavidin was dissolved in 4 mL of PBS buffer, and then flowed through the channel structure over the arrays where the streptavidin protein bonded to the biotin linker. The streptavidin solution flowed for 15 min at a rate of 0.02 mL/min. The transmission spectrum was then measured with the streptavidin-PBS solution in the channel. Then the channel was flushed with just PBS buffer and measurements taken again. These two final measurements were expected to give the same result.

All of the substances used to mix the solutions for protein bonding absorbed water very quickly from the air. This made measuring the exact mass difficult since the mass reading on the balance tended to increase the longer the substance was left. To resolve this problem, weighing the substances was done as quickly as possible to minimize exposure to air.

The total surface group assembly process corresponded to resonance peak shifts of approximately 2 to 7 nm in arrays 3 through 6. The intermediate measurements with biotin alone, however, were difficult to interpret. The average shift in resonance peak using bare gold as a reference was 0.5 nm for the cysteamine monolayer with a standard deviation of 0.9 nm, 1.5 nm for the biotin linker with a standard deviation of 1.3 nm, 2.2 nm for streptavidin in PBS buffer with a standard deviation of 1.9 nm, and 2.5 nm for measurements in PBS buffer alone after flushing out the streptavidin solution with a standard deviation of 1.9 nm. Little change in these resonance peak locations following the final rinse indicated both the formation of surface groups and the surface-specific nature of the SPR based sensors. The magnitude of the shifts reported here are in general agreement with earlier experimental work [Brolo et al. (2004a)], but not as high as reported by theory [Jung et al. (1998)]. Although larger shifts would increase sensitivity and accuracy of the device, the results presented here effectively demonstrate the application of SPR based sensors on-chip. The individual runs and some aspects that led to relatively high standard deviations are discussed next.

Three sets of data were obtained with spectra at each array (1 through 6) at each stage of the protein binding process with results plotted in figure 3.16a, b, and c corresponding to each of the three data sets. The gold sample was cleaned of protein between each run. In figure 3.16a, the first data run, the cysteamine monolayer shift in resonance wavelength was within +/- 1 nm of the bare gold case, the biotin shift was within 2 to 3 nm, and the streptavidin protein shift ranged from 1 to 2 nm. The shift in streptavidin protein measurements seemed to decrease below the biotin value, however, the shift was greater than the cysteamine monolayer measurements and up to 2 nm greater than the bare gold reference.

In figure 3.16b, the second data run, the cysteamine values shifted consistently below the bare gold values by about 1 nm and the biotin data was very scattered. The protein shifts were consistently above both biotin and cysteamine monolayer shifts, with shifts around 2 nm in arrays 3 through 6. Arrays 1 and 2 had consistently low shifts in both the first and second data runs. This could be due to damaged arrays, arrays out of alignment or contamination. In the second data run, the streptavidin solution was flushed out of the channel with a PBS buffer; there was very little difference in the streptavidin shifts and the PBS flushing shifts as expected, indicating the formation of surface groups.

In figure 3.16c, the third data run, the cysteamine monolayer shift was within +/- 1 nm of the bare gold value as in figure 3.16a and there was less scatter in the biotin compared to figure 3.16b. The protein shift was consistently above the biotin and cysteamine readings up to 5 to 7 nm, double the shift seen in figure 3.16b. It appeared that the streptavidin layers were building on each other, perhaps due to incomplete cleaning. In figure 3.16c, array 1 had an unusually high resonance wavelength shift for the streptavidin protein and the PBS buffer flushing measurements and was not plotted, this could be due to an air bubble in the microfluidic channel or contamination. Arrays 5 and 6 were outside of the channel and did not provide measurements.

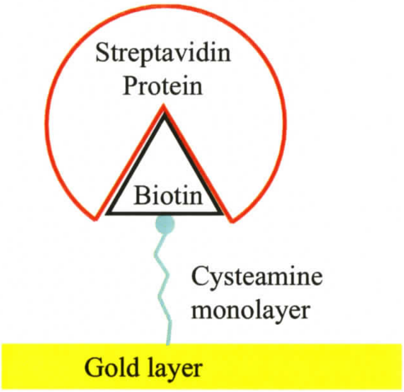

Figure 3.15 Streptavidin protein binding process. First a cysteamine monolayer is formed on the gold surface, then a biotin linker is attached to the monolayer and finally, streptavidin protein binds to the biotin linker.

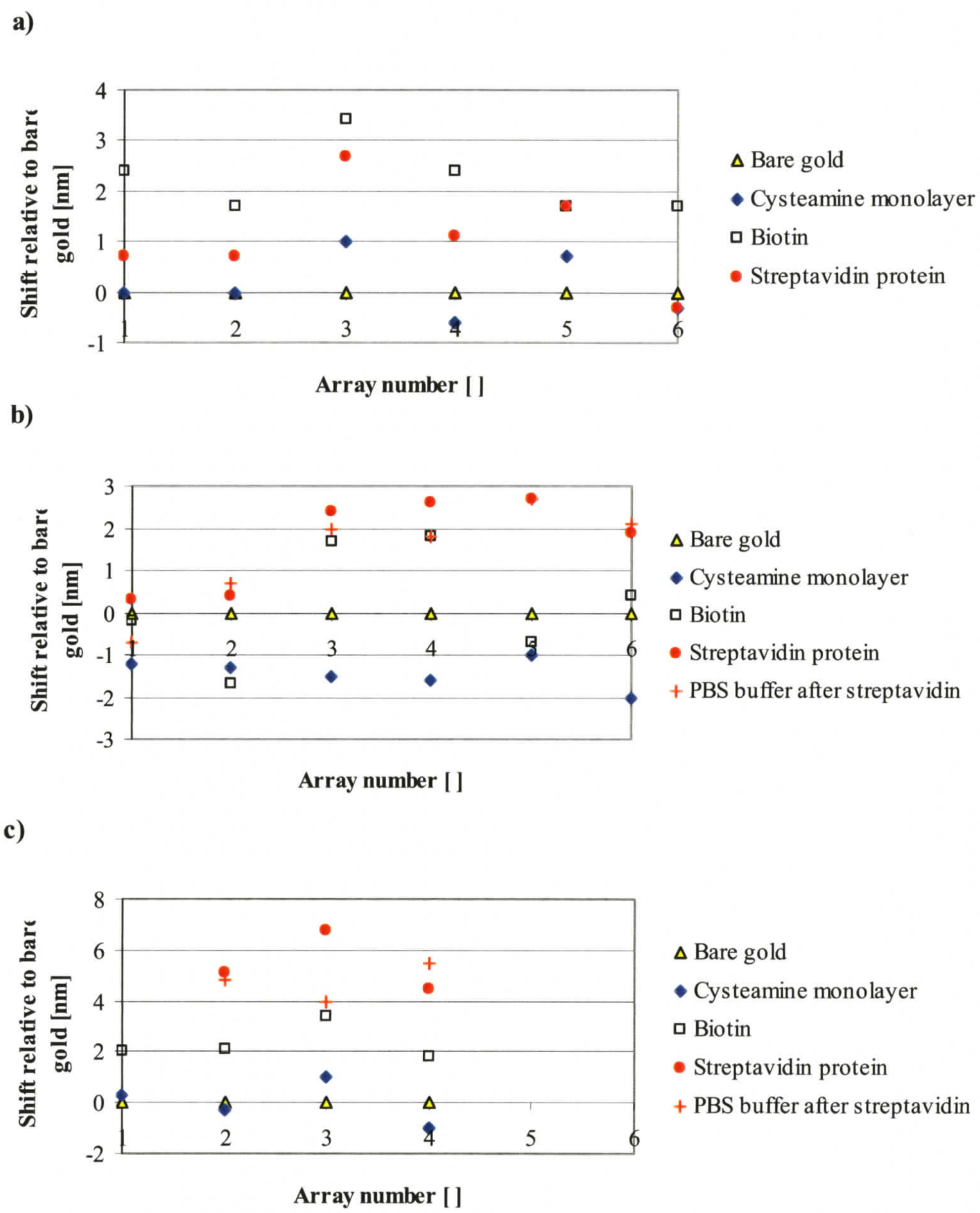

Figure 3.16 Shift in resonance wavelengths relative to bare gold at each stage of protein binding for three different sets of data a) run 1 b) run 2 c) run 3. Measurements are taken at four different stages in the protein binding: after the cysteamine monolayer has formed on the gold surface while a PBS buffer is in the channel (cysteamine monolayer data points), after the biotin linker has flowed and is replaced with PBS buffer (biotin data points), after streptavidin solution has been flowing in the channel for 15 minutes (streptavidin protein), and lastly after the streptavidin solution has been replaced with PBS buffer (PBS buffer after streptavidin). The resonance wavelength is obtained for arrays 1 through 6. In c) two outlying data points on array 1 are not plotted as they greatly exceeded the plotted range; no data is available for arrays 5 and 6 outside the channel.

3.4 Summary

A microfluidic device with embedded nanohole array sensors was built and demonstrated. Measurements indicate that arrays of nanoholes can be integrated and used as effective SPR detectors in an on-chip format to detect changes in refractive index, measure cross-stream concentration gradients, and detect specific surface binding events.

Chapter 4

CONCLUSIONS AND FUTURE WORK

4.1 Conclusions and Contributions of this Thesis

This thesis was devoted to an investigation of species transport in nanostructures and on-chip species detection using nanohole arrays. A combination of analytical, numerical and experimental techniques were employed. The contributions of this work included the development of an analytical solution and a numerical model to quantify ionic dispersion in nanochannels with finite EDLs and identify fundamental dispersion mechanisms unique to nanoscale flows. Experimental work included the fabrication and demonstration of a microfluidic device with embedded nanohole array SPR sensors. As proof of concept, the device was applied to detect bulk changes in liquid concentration, measure cross-stream concentration gradients, and monitor surface protein binding events. These contributions are summarized below.

4.1.1 Ionic Dispersion in Nanochannels

A continuum based analytical solution and numerical model were developed to investigate dispersion of charged and neutral species in nanofluidic channels with finite EDLs. The presented analytical solution provides a dispersion coefficient for circular cross-section channels as a function of a valance parameter, the relative EDL thickness, and the form of the velocity profile. Results indicate that in both pressure- and electrokinetically driven flows, ionic dispersion phenomena result from the combination of two unique effects. The first, charge-shear coupling dispersive effect, is a product of cross-stream ionic segregation and differential shear rates due to radially-varying velocity gradients. This effect tends to increase dispersion of counter-ions and decrease dispersion of co-ions. The second, electromigration dispersion-limiting effect, results from the restriction on radial diffusion imposed by electrostatic forces. This effect tends to decrease dispersion of all ions, and particularly of counter-ions, relative to neutral solutes. In general, co-ion dispersion is overestimated by previous theory based on neutral solutes, whereas counter-ion dispersion is underestimated at moderate, and overestimated at high relative EDL thicknesses. An independent numerical model using the nonlinear Poisson-Boltzmann equation was implemented to cross-validate the analytical solution, quantify the effect of the linearization of the Poisson-Boltzmann equation, and extend the results to higher relative EDL thicknesses. Computational results supported those of the analytical solution in the suggested range of applicability, $0.05 \leq \lambda_D / a \leq 0.4$. Combined, these results can inform the further development of nanostructured separation technologies with the aim of minimizing dispersion. The dependencies of ionic dispersion on valence charge and EDL thickness established here may also be strategically exploited to inform separation processes, for example nanoscale electrophoretic separations, or to constitute a new separation mechanism inherent to the nanoscale.

4.1.2 Microfluidic Device with Nanohole Arrays

A microfluidic device with embedded nanohole array SPR sensors was built and demonstrated experimentally. Measurements indicate that arrays of nanoholes can be integrated and used as effective SPR detectors in an on-chip format. Sensor functionality requires detectable resonance peaks in the transmitted spectral output that shift significantly in response to local changes in refractive index (proportional to concentration changes) at the array surface. With the detector employed here, the 350 nm to 650 nm periodicity arrays showed resonance peaks that shifted with varying refractive index making them suitable as sensors. The 450 nm periodicity array exhibited the sharpest resonance peaks. The 750 nm and 850 nm periodicity arrays are unsuitable as sensors in the visible light range and did not show resonance peaks. The microfluidic device was successfully applied to detect changes in refractive index with a sensitivity of 333 nm/RIU, comparable to previously reported values [Brolo et al. (2004a)]. Employing a cross-stream array of nanohole arrays, the device is applied to detect microfluidic concentration gradients as well as to detect surface binding in the assembly process of a cysteamine monolayer-biotin-streptavidin system. In gradient-based measurements, cross-stream concentrations determined at a range of flow rates agreed well with dye-based visualization experiments and analytical descriptions of the mixing process. In the protein binding event monitoring experiments, shifts in resonance wavelength of 2 to 7 nm were observed which is in general agreement with earlier experimental work [Brolo et al. (2004a)]. Although larger shifts would increase sensitivity and accuracy of the device, the results presented here effectively demonstrate the application of SPR based nanohole array sensors on-chip.

4.2 Proposed Future Work

Some aspects of this work that could be extended to future projects are suggested below.

4.2.1 Extension of the Numerical Model for Ionic Dispersion

During the numerical investigation of ionic dispersion in nanochannels, the nonlinear Poisson Boltzmann equation was used to model the electric potential due to the EDL. For the range of surface charge densities and zeta potentials used in this thesis, electric potential distributions calculated with the Poisson Boltzmann equation closely agree with the more complete Hypernetted Chain Theory model which takes finite ion size effects into account. As a further extension and validation of both the analytical solution and the numerical model, the Hypernetted Chain Theory could be employed to calculate the electric potential in the EDL and this new model could be used to extend the range of applicability.

Both the analytical solution and numerical model use a constant surface charge density as a boundary condition. In this thesis, it is assumed that the surface charge density does not change with relative EDL thickness; however this limits the numerical model to relative EDL thickness values below approximately $\lambda_D / a = 0.67$. The variation of surface charge density with relative EDL thickness could be taken into consideration to extend the numerical model to larger relative EDL thickness values and account for the surface charge variation with proximity to other charged surfaces.

4.2.2 Further Experiments in Nanohole Arrays

Measurements of cross-stream concentration gradients using the nanohole array SPR sensors was successfully demonstrated using sugar solutions and water. A further application of this technique would be to pattern a selected number of arrays with a specific chemical while the remaining arrays are left bare during chemical sensing. This could be particularly useful for patterning the arrays with cysteamine, biotin and streptavidin. For example, one array could be left bare as a reference case, another array could be patterned with a cysteamine monolayer only, a second array could have a cysteamine with biotin linker, and a third array could have the streptavidin protein bonded to it. Measurements from all four stages in the assembly process could then be compared side-by-side. Colaminar microfluidic focusing would enable independent addressing of the cross-stream arrays both for surface group deposition and later detection.

Although shifts in resonance wavelength were observed during the protein binding step, the shifts were small (2 to 7 nm) and the broad halogen light source produced transmission spectra that were somewhat noisy. An improvement in resolution could be obtained using a laser instead of the halogen light source. This experiment could be repeated using a laser with a wavelength output in a high slope region of the spectral response (close to the resonance wavelength of the arrays). As resonance shifts occur, a significant difference in the laser light intensity would be observed. The differences in transmitted intensity will be proportional to the change in refractive index that occurs at the array surface during the various stages of protein binding and may provide a more effective detection method. Intensity measurements are also more straightforward than broadband spectral shifts to analyze and thus more applicable to device-level integration. As a control to test protein binding, leaving out the biotin and running the experiment with cysteamine and streptavidin only could be done. Without biotin, the streptavidin will not bind to the cysteamine and therefore shifts in resonant wavelengths are not expected to occur. The data obtained can then be used to compare bonded streptavidin to streptavidin that is not bonded.

The array periodicity may also effect detection of protein binding events; the 650 nm periodicity arrays used to monitor protein binding show smaller resonance peaks compared to the 350 nm to 550 nm periodicity arrays. More conclusive results may be obtained with a row of 350 nm, 450 nm and 550 nm periodicity arrays since they show sharper resonance peaks with a greater light intensity. It would also be of interest to repeat the concentration gradient generation experiments using these rows of arrays. Use of higher periodicity arrays with infrared based detectors would also be of interest.

REFERENCES

Aris, R. (1956) "On the Dispersion of a Solute in a Fluid Flowing Through a Tube." Proceedings of the Royal Society of London, 235A, 67-77.

Atencia, J., Beebe, D. J. (2005) "Controlled microfluidic interfaces." Nature, 437, 648-655.

Attard, P., Antelmi, D., Larson, I. (2000) "Comparison of the Zeta Potential with the Diffuse Layer Potential from Charge Titration." Langmuir, 16, 1542-1552

Barnes, W. L., Dereux, A., Ebbesen, T. W. (2003) "Surface Plasmon Subwavelength Optics." Nature, 424, 824-830.

Bazylak, A., Sinton, D., Djilali, N. (2005) "Improved Fuel Utilization in Microfluidic Fuel Cells: A Computational Study." Journal of Power Sources, 143, 57-66.

Behrens, S. H., Grier, D. G. (2001) "The Charge of Glass and Silica Surfaces." Journal of Chemical Physics, 115 (14), 6716-6721.

Bird, R., Stewart, W. E., Lightfoot, E. N. (1960) "Transport Phenomena." John Wiley & Sons, New York, NY.

Bousse, L., Cohen, C., Nikiforov, T., Chow, A., Kopf-Sill, A. R., Dubrow, R., Parce, W. (2000) "Electrokinetically controlled microfluidic analysis systems." Ann Rev Biophys Biomol Struct, 29, 155–181.

Brody, J. P., Yager, P., Goldstein, R. E., Austin, R. H. (1996) "Biotechnology at low Reynolds numbers." Biophysics, J 71, 3430–3441.

Brolo, A. G., Gordon, R., Leatham, B., Kavanagh, K. L. (2004a) "Surface plasmon sensor based on the enhanced light transmission through arrays of nano-holes in gold films." Langmuir, 20, 4813-4815.

Brolo, A. G., Arctander, E., Gordon, G., Leathem, B., Kavanagh, K. L. (2004b) "Nanohole-Enhanced Raman Scattering." Nano Letters, 4 (10), 2015-2018.

Brolo, A. G., Kwok, S. C., Moffitt, M. G., Gordon, R., Riordan, J., Kavanagh, K. L. (2005) "Enhanced Fluorescence from Arrays of Nanoholes in a Gold Film." Journal of the American Chemical Society, 127, 14936-14941.

Burgreen, D., Nakache, F. R. (1964) "Electrokinetic Flow in Ultrafine Capillary Slits." Journal of Physical Chemistry, 68, 1084-1091.

Crabtree, H. J., Cheong, E. C. S., Tilroe, D. A., Backhouse, C. J. (2001) "Microchip Injection and Separation Anomalies Due to Pressure Effects." Analytical Chemistry, 73, 4079-4086.

Daiguji, H., Yang, P., Szeri, A. J., Majumdar, A. (2004a) "Electrochemomechanical Energy Conversion in Nanofluidic Channels." Nano Letters, 4 (12), 2315-2321.

Daiguji, H., Yang, P., Majumdar, A. (2004b) "Ion Transport in Nanofluidic Channels." Nano Letters, 4 (1), p137-142.

Datta, R., Kotamarthi, V. R. (1990) "Electrokinetic Dispersion in Capillary Electrophoresis." AIChe Journal, 36 (6), 916-926.

De Leebeeck, A., Sinton, D., Brolo, A. G., Arctander, E., Gordon, R. Kavanagh, K. (2004) "Electrokinetic Flow Over a Nano-hole Array Sensor." ASME-IMECE, Anaheim CA.

De Leebeeck, A., Sinton, D. (2005) "Taylor-like Dispersion in Electrokinetically-Driven Nanoflows." ASME-IMECE, Orlando FL.

De Leebeeck, A., Kumar, L. K. S., Brolo, A. G., Gordon, R., Sinton, D. (2006a) "On-chip Detection with Nanohole Arrays." IEEE/LEOS Summer Topicals, Quebec City, QC.

De Leebeeck, A., Sinton, D. (2006), "Ionic Dispersion in Nanofluidics." Submitted to Electrophoresis.

De Leebeeck, A., Sinton, D., Brolo, A. G., Gordon, R., et al. (2006) "Multiple nanohole array sensing on-chip." to be submitted July/August 2006.

de Mello, A. (2002) "Plastic fantastic?" Lab on a chip, 2, 31N-36N.

Duffy, D. C., McDonald, J. C., Schueller, O. J. A., Whitesides, G. M. (1998) "Rapid Prototyping of Microfluidic Systems in Poly(dimethylsiloxane)." Analytical Chemistry, 70, 4974-4984.

Dutta, P., Beskok, A. (2001) "Analytical Solution of Combined Electroosmotic/Pressure Driven Flows in Two-Dimensional Straight Channels: Finite Debye Layer Effects." Analytical Chemistry, 73, 1979-1986.

Dutta, D., Leighton, D. T. (2002) "A Low Dispersion Geometry for Microchip Separation Devices." Analytical Chemistry, 74, 1007-1016.

Dyer, C. K., (2002) "Fuel cells for portable applications." Journal of Power Sources, 106, 31-34.

Ebbesen, T. W., Lezec, H. J., Ghaemi, H. F., Thio, T., Wolff, P. A. (1998) "Extraordinary Optical Transmission Through Sub-Wavelength Hole Arrays." Nature, 391, 667-669.

Eijkel, J. C. T., van den Berg, A. (2005) "Nanofluidics: What is it and What can we Expect from it?" Microfluidics and Nanofluidics, 3, 249-267.

Eijkel, J. C. T., van den Berg, A. (2006) "The Promise of Nanotechnology for Separation Devices – from a Top-Down Approach to Nature-Inspired Separation Devices." Electrophoresis, 27, 677-685.

Gad-el-Hak, M. (2005) "Liquids: The Holy Grail of Microfluidic Modeling." Physics of Fluids, 17, 100612.

Garcia, A. L., Ista L. K., Petsev, D. N., O'Brien, M. J., Bisong, P., Mammoli, A. A., Brueck, S. R. J., Lopez, G. P. (2005) "Electrokinetic Molecular Separation in Nanoscale Fluidic Channels." Lab on a Chip, 5, 1271-1276.

Ghosal, S. (2004) "Fluid mechanics of electroosmotic flow and its effect on band broadening in capillary electrophoresis." Electrophoresis, 25, 214-228.

Gordon, R., Brolo, A. G., McKinnon, A., Rajora, A., Leatham, B., Kavanagh, K. L. (2004) "Strong polarization in the optical transmission through elliptical nano-hole arrays." Physical Review Letters, 92 (3), article number 037401.

Griffiths, S. K., Nilson, R. H. (1999) "Hydrodynamic Dispersion of a Neutral Nonreacting Solute in Electroosmotic Flow." Analytical Chemistry, 71, 5522-5529.

Griffiths, S. K., Nilson, R. H. (2000a) "Band Spreading in Two-Dimensional Microchannel Turns for Electrokinetic Species Transport." Analytical Chemistry, 72, 4767-4777

Griffiths, S. K., Nilson, R. H. (2000b) "Electroosmotic Fluid Motion and Late Time Solute Transport for Large Zeta Potentials." Analytical Chemistry, 72, 5473-5482.

Gzil, P., Vervoort, N., Baron, G. V., Desmet, G. (2003) "Advantages of Perfectly Ordered 2-D Porous Pillar Arrays over Packed Bed Columns for LC Separations: A Theoretical Analysis." Analytical Chemistry, 75, 6244-6250.

Haes, A. J., Hall, W. P., Chang, L., Klein, W. L., Van Duyne, R. P. (2004) "A Localized Surface Plasmon Resonance Biosensor: First Steps toward an Assay for Alzheimer's Disease." Nano Letters, 4, 1029-1034.

Han, J., Craighead, H. G. (2000) "Separation of Long DNA Molecules in a Microfabricated Entropic Trap Array." Science, 288, 1026-1029.

Herr, A. E., Molho, J. I., Santiago, J. G., Mungal, M. G., Kenny, T. W., Garguilo, M. G. (2000) "Electroosmotic capillary flow with nonuniform zeta potential." Analytical Chemistry, 72 (5), 1053-1057.

Ho, C. M., Tai, Y. C. (1998) "Micro-electro-mechanical-systems (MEMS) and fluid flows." Ann Rev Fluid Mech, 30, 579–612

Huang, L. R., Cox, E. C., Austin, R. H. (2004) "Continuous Particle Separation Through Deterministic Lateral Displacement." Science, 304, 987-990.

Hunter, R. J. (1981) "Zeta Potential in Colloid Science: Principles and Applications", Academic Press, New York, NY.

Ismagilov, R. F., Stroock, A. D., Kenis, P. J. A., Whitesides, G. (2000) "Experimental and theoretical scaling laws for transverse diffusive broadening in two-phase laminar flows in microchannels." Applied Physics Letters, 76 (17), 2376–2378.

Jung, L. S., Campbell, C. T., Chinowsky, T. M., Mar, M. N., Yee, S. S. (1998) "Quantitative Interpretation of the Response of Surface Plasmon Resonance Sensors to Adsorbed Films." Langmuir, 14, 5636-5648.

Kamholz, A. E. (2004) "Proliferation of Microfluidics in Literature and Intellectual Property" Lab on a Chip, 4, 16N–20N.

Karnik, R., Fan, R., Yue, M.; Li, D., Yang, P., Majumdar, A. (2005) "Electrostatic Control of Ions and Molecules in Nanofluidic Transistors." Nano Letters, 5 (5), p943-948.

Kirby, B. J., Hasselbrink Jr., E. F. (2004) "Zeta Potential of Microfluidic Substrates: 1. Theory, Experimental Techniques, and Effects on Separations." Electrophoresis, 25, 187-202.

Kuo, T. C., Sloan, L. A., Sweedler, J. V., Bohn, P. W. (2001) "Manipulating Molecular Transport through Nanoporous Membranes by Control of Electrokinetic Flow: Effect of Surface Charge Density and Debye Length." Langmuir 2001, 17, 6298-6303.

Lee, J. N., Park, C., Whitesides, G. M. (2003) "Solvent Compatibility of Poly(dimethylsiloxane)-Based Microfluidic Devices." Analytical Chemistry, 75, 6544-6554.

Li, D. (2004) "Electrokinetics in microfluidics." Academic Press, New York.

Liu, Y., Bishop, J., Williams, L., Blair, S., Herron, J. (2004) "Biosensing Based Upon Molecular Confinement in Metallic Nanocavity Arrays." Nanotechnology, 15, p1368-1374.

McDonald, J. C., Duffy, D. C., Anderson, J. R., Chiu, D. T., Wu, H., Schueller, O. J. A., Whitesides, G. M. (2000) "Fabrication of Microfluidic Systems in Poly(dimethylsiloxane)" Electrophoresis, 21, 27-40.

McKechnie (2006) "Fabrication of Microfluidic Devices with Application to Membraneless Fuel Cells." Master's thesis, University of Victoria, Victoria, BC, Canada.

Molho, J. I., Herr, A. E., Mosier, B. P., Santiago, J. G., et al. (2001) "Optimization of Turn Geometries for Microchip Electrophoresis." Analytical Chemistry, 73, 1350-1360.

Neuert, G., Kufer, S., Benoit, M., Gaub, H. E. (2005) "Modular multichannel surface plasmon spectrometer." Review of Scientific Instruments, 76 (5), Art. No. 054303.

Ng, J. M. K., Gitlin, I., Stroock, A. D., Whitesides, G. M. (2002) "Components for integrated poly(dimethylsiloxane) microfluidic systems." Electrophoresis, 23, 3461-3473.

Nguyen, N. T., Wereley, S. T. (2002) "Fundamentals and applications of microfluidics." Artech House, Norwood, MA

Nice, E. C., Catimel, B. (1999) "Instrumental biosensors: new perspectives for the analysis of biomolecular interactions." BioEssays, 21, 339-352.

Pennathur, S., Santiago, J. G. (2005a) "Electrokinetic Transport in Nanochannels. 1. Theory." Analytical Chemistry, 77, 6772-6781.

Pennathur, S., Santiago, J. G. (2005b) "Electrokinetic Transport in Nanochannels. 2. Experiments." Analytical Chemistry, 77, 6782-6789.

Plecis, A., Schoch, R. B., Renaud, P. (2005) "Ionic Transport Phenomena in Nanofluidics: Experimental and Theoretical Study of the Exclusion-Enrichment Effect on a Chip." Nano Letters, 5 (6), 1147-1155.

Probstein, R. F. (1994) "Physicochemical Hydrodynamics" 2nd Ed., John Wiley & Sons.

Pu, Q., Yun, J., Temkin, H., Liu, S. (2004) "Ion-Enrichment and Ion-Depletion Effect of Nanochannel Structures." Nano Letters, 4 (6), 1099-1103.

Qiao, R., Aluru, N. R. (2003) "Ion Concentrations and Velocity Profiles in Nanochannel Electroosmotic Flows." Journal of Chemical Physics, 118 (10), 4692-4701.

Reyes, D. R., Iossifidis, D., Auroux, P. A., Manz, A. (2002) "Micro total analysis systems. 1. Introduction, theory, and technology." Analytical Chemistry, 74, 2623–2636.

Rice, C. L., Whitehead, R. (1965) "Electrokinetic Flow in a Narrow Cylindrical Capillary." Journal of Physical Chemistry, 69, 4017-4024.

Santiago, J. G. (2001) "Electroosmotic Flows in Microchannels with Finite Inertial and Pressure Forces", Analytical Chemistry, 73, 2353-2365.

Schlichting, H. (1968) "Boundary-Layer Theory" 6th Ed, McGraw-Hill Book Company, New York, NY.

Sharp, K. V., Adrian, R. J., Santiago, J. G., and Molho, J. I. (2002) "Liquid Flows in Microchannels" In: Gad-el-Hak M (ed), CRC Handbook of MEMS. CRC Press, New York, pp. 6-1–6-38.

Sinton, D. (2003) "Microscale flow visualization." PhD thesis, University of Toronto, Toronto, Ontario, Canada

Siwy, Z., Fulinski, A. (2002) "Fabrication of a Synthetic Nanopore Ion Pump." Physical Revue Letters, 89, 198103

Squires, T. M., Quake, S. R. (2005) "Microfluidics: Fluid physics at the nanoliter scale." Reviews of Modern Physics, 77, 977-1026.

Stone, H. A., Stroock, A. D., and Ajdari, A. (2004) "Engineering Flows in Small Devices: Microfluidics Toward a Lab-on-a-Chip" Annual Revue of Fluid Mechanics 36:381–411.

Storhoff, J. J., Lucas, A. D., Garimella, V., Bao, Y. P., Muller, U. R. (2004) "Homogeneous detection of unamplified genomic DNA sequences based on colorimetric scatter of gold nanoparticle probes." Nature Biotechnology, 22, 883-887.

Struchtrup, H. (2005), "Macroscopic Transport Equations for Rarefied Gas Flows Approximation Methods in Kinetic Theory." Springer, Heidelberg.

Taylor, G. T. (1953) "Dispersion of Soluble Matter in Solvent Flowing Slowly Through a Tube", Procedings of the Royal Society of London, Series A, 219A, 186-203.

Tegenfeldt, J. O., Prinz, C., Cao, H., Huang, R. L., Austin, R. H., Chou, S. Y., Cox, E. C., Sturm, J. C. (2004) "Micro- and nanofluidics for DNA analysis." Analytical and Bioanalytical Chemistry, 378, 1678-1692.

Van Theemsche, A., Deconinck, J., Van den Bossche, B., Bortels, L. (2002) "Numerical Solution of a Multi-Ion One-Potential Model for Electroosmotic Flow in Two-Dimensional Rectangular Microchannels." Analytical Chemistry, 74, 4919-4926.

Verpoorte, E., De Rooij, N. F. (2003) "Microfluidics meets MEMS." Proc IEEE, 91, 930–953

Vukusic and Sambles (2003) "Photonic structures in biology." Nature, 424, 852-855.

Weigl, B. H., Yager, P. (1999) "Microfluidics Diffusion-Based Separation and Detection." Science, 283 (5400), 346-347.

White, F. M. (1999) "Fluid Mechanics." 4th Ed., WCB/McGraw-Hill, Boston.

Whitesides, G. M., Stroock, A. D. (2001) “Flexible methods for microfluidics.” Physics Today, 54(6), 42–48.

Zhang, X., Young, M. A., Lyandres, O., Van Duyne, R. P. (2005) “Rapid Detection of an Anthrax Biomarker by Surface-Enhanced Raman Spectroscopy.” Journal of the American Chemical Society, 127, 4484-4489.

Zholkovskij, E. K., Masliyah, J. H., Czarnecki, J. (2003) “Electroosmotic Dispersion in Microchannels with a Thin Double Layer.” Analytical Chemistry, 75, 901-909.

Zholkovskij, E. K., Masliyah, J. H. (2004) “Hydrodynamic Dispersion due to Combined Pressure-Driven and Electroosmotic Flow Through Microchannels with a Thin Double Layer.” Analytical Chemistry, 76, 2708-2718.